O.V. Lounasmaa Laboratory

Nanostructured Materials under Ion and Microwave Radiation

Khattiya Chalapat

A!

DOCTORAL DISSERTATIONS

Aalto University publication series
DOCTORAL DISSERTATIONS 91/2013

Nanostructured Materials under Ion and Microwave Radiation

Khattiya Chalapat

A doctoral dissertation completed for the degree of Doctor of Science (Technology) to be defended, with the permission of the Aalto University School of Science, at a public examination held at the auditorium J of the main building, on 24th May 2013 at 12 noon.

Aalto University
School of Science
O.V. Lounasmaa Laboratory

Supervising professor
Prof. Jukka Pekola

Thesis advisor
Docent Gheorghe-Sorin Paraoanu

Preliminary examiners
Prof. Mark Blamire, University of Cambridge, UK
Assoc. Prof. Ugur Cem Hasar, Ataturk University, Turkey

Opponent
Assoc. Prof. Eyal Buks, Technion-Israel Institute of Technology

Aalto University publication series
DOCTORAL DISSERTATIONS 91/2013

ISBN 978-952-60-5188-8 (printed)
ISBN 978-952-60-5189-5 (pdf)
ISSN-L 1799-4934
ISSN 1799-4934 (printed)
ISSN 1799-4942 (pdf)
http://urn.fi/URN:ISBN:978-952-60-5189-5

Unigrafia Oy
Helsinki 2013

Finland

441 697
Printed matter

Aalto University

Abstract

Aalto University, P.O. Box 11000, FI-00076 Aalto www.aalto.fi

Author
Khattiya Chalapat

Name of the doctoral dissertation
Nanostructured Materials under Ion and Microwave Radiation

Publisher School of Science

Unit O.V. Lounasmaa Laboratory

Series Aalto University publication series DOCTORAL DISSERTATIONS 91/2013

Field of research Engineering Physics, Nanoscience

Manuscript submitted 12 February 2013 **Date of the defence** 24 May 2013

Permission to publish granted (date) 2 May 2013 **Language** English

☐ **Monograph** ☒ **Article dissertation (summary + original articles)**

Abstract

This thesis discusses how ion radiation and microwaves interact with nanoscale-structured materials.

In the case of ion radiation, the experiments show that ion processing, either with low-energy ions in reactive ion etching or with higher energy ions in focused ion beams, produces inelastic strain in polycrystalline thin metallic films. This results in the bending of thin strips of metallic films, which cannot be explained by elastic models. The concept of ion-induced plastic strain implies the insertion of adatoms into grain boundaries within the metal matrix. In ion etching processes, thin strips of metallic films with different widths were released from the substrate at different times. Therefore, the rate of atomic flow into grain boundaries is different for different strips. The larger curvatures in narrower strips are the result of a faster rate of adatom insertion into the grain boundaries. With a high-energy focused ion beam, plastic strain can be created locally, allowing the fabrication of non-trivial three-dimensional structures at nanometer scales.

In the case of microwave radiation, the materials studied include cobalt nanoparticles and carbon nanotubes. The magnetic resonance and absorption in cobalt nanoparticles are observed in various magnetizing fields at frequencies between 0.5 and 18 GHz, by using a wideband method. The obtained experimental results show that the energy absorption is associated with the ferromagnetic resonance of cobalt nanoparticles. The results include measurements of blocking temperature and saturation magnetization with SQUID magnetometry. The absorption spectra are analyzed theoretically by combining Kittel's theory for uniaxial spherical particles, the Landau-Lifshitz-Gilbert equation and effective medium models. At zero magnetizing field, the observed resonance occurs at higher frequencies compared to the non-interacting particle model. The shift of resonance is suggested to be caused by the clustering of particles. Transmission electron microscopic images demonstrate that indeed particles aggregate in the forms of clusters, superlattices, and chains. The absorption properties of yarns of carbon nanotubes are also presented in the thesis.

Keywords Nanoscale materials, Magnetic nanoparticles, Carbon nan- otubes, Thin metal films, Ferromagnetic resonance, Microwave, Reactive- ion etching, Focused ion beam, Self-organization, 3D-nanofabrication

ISBN (printed) 978-952-60-5188-8 **ISBN (pdf)** 978-952-60-5189-5

ISSN-L 1799-4934 **ISSN (printed)** 1799-4934 **ISSN (pdf)** 1799-4942

Location of publisher Espoo **Location of printing** Helsinki **Year** 2013

Pages 285 **urn** http://urn.fi/URN:ISBN:978-952-60-5189-5

Preface

This dissertation and the published research articles were carried out mainly at the O.V. Lounasmaa Laboratory of Aalto University between July 2008 and July 2012. Relevant basic studies and a part of research were completed at Nanoscience Center, university of Jyväskylä in the years 2006-2008.

First, I would like to express my gratitude to Docent Sorin Paraoanu, for his strategic guidance and invaluable advice throughout my research and studies. It has been a privilege working in Kvantti group under his supervision, and at the same time getting the freedom and the encouragement to pursue my own ideas. Secondly, I am grateful to Sami Ylinen, my colleague at the Nanoscience Center, University of Jyväskylä, for teaching various laboratory practice of nanofabrication and also for his enduring friendship. M.Sc. Kari Sarvala and M.Sc. Ville Haaksluoto are acknowledged for their contribution in microwave instrumentations at University of Jyväskylä. My appreciation goes also to Dr. Jian Li for his long cordial collaboration during his PhD study in the Kvantti group. Next, I am really grateful to Dr. Alexander Savin for giving me numerous helpful advice and supports, particularly when I first joined the O.V. Lounasmaa Laboratory in 2008. My deep gratitude goes to my supervising professors, Prof. Jukka Pekola and Prof. Matti Kaivola, whose guidance has helped me to develop and present my dissertation more cogently.

For the study of magnetic nanoparticles, I very much appreciate my main collaborators, Dr. Jaakko Timonen, Maija Huuppola, and Lari Koponen, for their endless time and efforts in making good samples; my gratitude goes also to Dr. Eira Seppälä, Dr. Markku Oksanen, Prof. Olli Ikkala, Dr. Robin H. A. Ras, Dr. Christoffer Johans, Dr. Jani Seitsonen, Prof. Sebastiaan van Dijken, Witold Skowronski, and Matti Sarjala. For the research on carbon-nanotube materials, I am really thankful to

Dr. Vladimir Ermolov for sharing carbon-nanotube yarns and also for many stimulating discussions, many thanks go also to Dr. Ilya Anoshkin and Antti Kaskela for the preparation of carbon nanotube composites and films. Relating to microwave theory and techniques, I very much appreciate intellectual discussions with Dr. Tapani Matala-aho, Prof. Sergei Tretyakov, Dr. Igor Nefedov, and Prof. Constantin Simovski. For the work on the effect of ion irradiation, I especially thank Dr. Hua Jiang and Dr. Nikolai Chekurov for their cheerful and genuine collaboration; discussions with Prof. Babak Parviz, Prof. Gennadiy Nikishkov, Prof. Chun-Wei Pao, Prof. Ken Elder, and Prof. Tapio Ala-Nissilä are also appreciated.

In the year 2006-2007, my study owed very much to the excellent learning atmosphere at University of Jyväskylä, and for this I would like to thank the present members and alumni of the Nanoscience center and Faculty of Mathematics and Science. In particular, my special thanks go to Dr. Minna Nevala, Dr. Jenni Karvonen, Dr. Terhi Hongisto, Kai Poras, Antti Nuottajarvi, Dr. Paavo Niutanen, Dr. Hannu Salo, Dr. Hannu Pakkanen, Dr. Jami Kinnunen, Dr. Piotr Prus, Riitta-Liisa Kuittinen, Prof. Markus Ahlskog, Docent Konstantin Yu. Arutyunov, Prof. Ilari Maasilta, Prof. Jouko Korppi-Tommola, Prof. Päivi Törmä, and Prof. Matti Manninen.

The excellent laboratory infrastructure and the pleasant working environment at the O.V. Lounasmaa Laboratory, which provides a playground for the most part of my research, owe very much to the dedication of the former Director, Prof. Mikko Paalanen, the Leaders, Prof. Pertti Hakonen, Prof. Grigori Volovik, Prof. Matti Krusius, Prof. Nikolai Kopnin, Prof. Mikka Sillanpää, Docent Tero Heikkila, Docent Juha Tuoriniemi, and the good-spirited members and alumni of the laboratory: Arvi Isomäki, Markku Korhonen, Hannu Kaukelin, Jayanta Sarkar, Antti Puska, Pasi Lähteenmäki, Matti Tomi, Pasi Häkkinen, Jaakko Sulkko, Dr. Xuefeng Song, Dr. Sung Un Cho, Dr. Juha Voutilainen, Dr. Matti Laakso, Karthikeyan Kumar, Antti Vepsäläinen, Robab Jabdaraghi, Dr. Dmitry Lyashenko, Dr. Aurelien Fay, Dr. Fan Wu, Laura Korhonen Äkäslompolo, Dr. Joonas Peltonen, Dr. Matthias Meschke, Ville Maisi, Matti Manninen, Juho Rysti, Dr. Anssi Salmela, and Dr. Alexander Sebedash. My gratitude goes also to the administrators and the secretaries, especially Liisi Pasanen, Tuire Koivisto, Pirjo Muukkonen, Teija Halme, Mari Kaarni, Olga Jakkola, and Minna Günes. Scientific resources and supports from the Department of Applied Physics and the Micronova Centre

for Micro and Nanotechnology are also appreciated; special thanks go to Dr. Janne Raula, Dr. Antti Soininen, Pasi Kostamo, Paula Heikkila, Dr. Victor Ovchinnikov, Dr. Sergey Novikov, Dr. Kestutis Grigoras, Dr. Lauri Sainiemi and Dr. Antti J. Niskanen.

Since the start of my PhD, I have been very fortunate to receive scholarships and research funding from numerous sources. First, it was a great honor to receive the strategic scholarship for frontier research network from Thailand's Commission on Higher Education during the year 2006-2011, under the administration of Chancellor Gesorn Ploysangvan and Chancellor Jutharat O'Gorman of the Royal Thai Embassy, Helsinki. Then, in the year 2009-2011, with an opportunity to be a scientist in projects related to the microwave characterization of nanomaterials, I received additional funding from Nokia research center (under a Tekes project). In 2012, my research continued as part of the Center of Excellence "Low Temperature Quantum Phenomena and Devices" and was generously supported by the Kvantti group (under an Academy of Finland project), O.V. Lounasmaa Laboratory, Aalto University.

Above all, I owe my deepest gratitude to my family for supporting me unconditionally with their love and compassion. My special thanks go to Uncle Jaturong Plienchao for lightening my early interest in science, and M.Ed. Pavinee Sothayapetch for cheering me up and encouraging me while I was preparing this manuscript. Finally, my gratitude goes to my friends and fellows who kept me grounded and made little things in my life valuable.

Helsinki, May 5, 2013,

Khattiya Chalapat

List of Publications

This thesis consists of an overview and of the following publications which are referred to in the text by their Roman numerals.

I K. Chalapat, K. Sarvala, J. Li, and G. S. Paraoanu. Wideband reference-plane invariant method for measuring electromagnetic parameters of materials. *IEEE Transactions on Microwave Theory and Techniques*, **57**, 2257-2267 (2009).

II K. Chalapat, G. S. Paraoanu, Z. Du, J. Tervo, I. Nefedov, and S. Tretyakov. Unity absorbance layers - optimal design criteria. In *Metamaterials 2010, Fourth International Congress on Advanced Electromagnetic Materials in Microwaves and Optics*, 279-281 (2010).

III K. Chalapat, N. Chekurov, J. Li, and G. S. Paraoanu. Ion beam assisted self-assembly of metallic nanostructures. *Nucl. Instrum. Meth. B*, **272**, 202-205 2012.

IV K. Chalapat, N. Chekurov, H. Jiang, J. Li, B. Parviz, and G. S. Paraoanu. Self-organized origami structures via ion-induced plastic strain. *Advanced Materials*, **25**, 91–95 (2013).

V A. Vepsäläinen, K. Chalapat, and G. S. Paraoanu. Measuring the microwave magnetic permeability of small samples using the short-circuit transmission line method. *IEEE Transactions on Instrumentation and Measurement*, In Press (2013).

VI K. Chalapat, J. Timonen, M. Huuppola, L. Koponen, C. Johans, R. H. A. Ras, O. Ikkala, M. Oksanen, E. Seppälä, and G. S. Paraoanu. Ferromagnetic resonance of ϵ-cobalt nanoparticle clusters. , Submitted (2013).

VII J. V. I. Timonen, R. H. A. Ras, O. Ikkala, M. Oksanen, E. Seppälä, K. Chalapat, J. Li, and G. S. Paraoanu. Magnetic nanocomposites at microwave frequencies. *Trends in nanophysics: theory, experiment, technology, edited by V. Barsan and A. Aldea*, Engineering Materials Series, Springer-Verlag, Berlin, ISBN: 978-3-642-12069-5 pp. 257-285.

Author's Contribution

Publication I: "Wideband reference-plane invariant method for measuring electromagnetic parameters of materials"

The author invented the algorithm, did the microwave measurements, analyzed the data, and was responsible for writing the manuscript.

Publication II: "Unity absorbance layers - optimal design criteria"

The author contributed to the analytical calculations and the writing of the manuscript.

Publication III: "Ion beam assisted self-assembly of metallic nanostructures"

The author conceived the experiments, fabricated the samples, and had the main contribution in writing the manuscript.

Publication IV: "Self-organized origami structures via ion-induced plastic strain"

The author conceived the experiments, fabricated the samples, developed the theoretical concepts, and wrote major parts of the manuscript.

Publication V: "Measuring the microwave magnetic permeability of small samples using the short-circuit transmission line method"

The author gave advice on the experimental methods and contributed to the revision of the manuscript.

Publication VI: "Ferromagnetic resonance of ϵ-cobalt nanoparticle clusters"

The author did the SQUID magnetometry and the microwave measurements, analyzed the data, and had the main responsibility of writing the manuscript.

Publication VII: "Magnetic nanocomposites at microwave frequencies"

The author did the microwave measurements, analyzed the data, and contributed in the writing about the microwave characterization of the materials.

Other Contributions of the Author

Publications

Publications by the author that are not included in this thesis:

1. J. Li, K. Chapalat, and G. S. Paraoanu, "Enhancement of sudden death of entanglement for driven qubits", *J. Low Temp. Phys.*, **153**, 294-303 (2008).

2. J. Li, K. Chalapat, and G. S. Paraoanu, "Entanglement of superconducting qubits via microwave fields: Classical and quantum regimes", *Phys. Rev. B*, **78**, 064503 (2008).

3. J. Li, K. Chalapat, and G. S. Paraoanu, "Measurement-induced entanglement of two superconducting qubits", *J. Phys.: Conference Series*, **150**, 022051 (2009).

4. W. Skowronski, J. Wrona, M. Frankowski, M. Czapkiewicz, T. Stobiecki, G. Reiss, K. Chalapat, G. S. Paraoanu, and S. van Dijken, "Influence of MgO tunnel barrier thickness on spin-transfer ferromagnetic resonance and torque in magnetic tunnel junctions", *Phy. Rev. B*, **87**, 094419 (2013).

Patents

Two patent applications, based on the work on microwaves presented in this thesis, have been submitted during the doctoral studies of the author.

Contents

1. Introduction

1.1 Fields and matter at nanoscale

When subatomic ingredients, such as electrons, protons and neutrons, join together to form condensed matter systems, collective phenomena emerge. These phenomena occur in all forms of matter ranging from chemistry in living organisms to the emergence of magnetic states and superconductivity. The interaction between the subatomic ingredients with the external world defines the existence and the manifestation of the world as we perceive it.

At the scale of one billionth of a meter (nanometer; symbol nm), most materials interact with the world differently from their macroscale counterparts, fundamentally because of the increasing interface (relative to the volume) between the material and the external world. When one of the dimensions of the material becomes comparable with a specific physical length, such as an electron's mean free path or the coherence length of a collective state, the corresponding phenomenon will change abruptly. At room temperature, electrons in metals loose their phase coherence on a length of several tens of nanometers. In magnetic materials, the interaction between electron spins causes the emergence of symmetry breaking and the aligning of all spins within a small region called magnetic domain.

Figure 1.1 shows a few examples of objects that exist at different scales in nature. Nowadays, nanofabrication technology allows the realization of complex structures at very small scales. Some structures are smaller than human red blood cells. Current applications of nanoscale structures are in electronic, energy, and medical sectors. Products include batteries, photovoltaic cells, catalysts, coatings, and sensors. There exist also more futuristic concepts such as nanorobots and quantum computers.

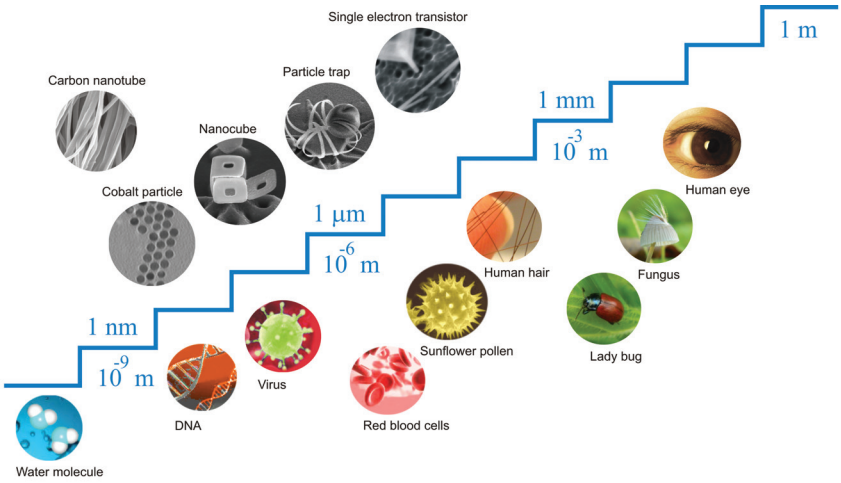

Figure 1.1. Natural and artificial objects in nature at different length scales. In the biological world, tree-pollens and microorganisms have their sizes range from hundred nanometers to several micrometers. At these scales, various materials including metals manifest themselves differently from their bulk counterpart. Technology, at the present time, allows the creation of artificial materials and complex devices at these tiny scales. Some (gray-scale) pictures in the upper part of the scale represent materials and devices fabricated and studied in this thesis.

1.2 Motivation and objectives of the research

The objectives of this work are two-fold: to increase the knowledge about nanoscale matter and to develop novel nanotechnologies.

1.2.1 Ion-based technology for 3D nanofabrication

Precise nanoengineering is a key towards a paradigm shift in science and technology. At nanoscales, there are two approaches for device fabrication: the 'top-down' approach and the 'bottom-up' approach. The bottom-up approach involves the formation of objects from atoms or molecules. Recently, a group of international researchers has successfully created a DNA nanobox that can be opened in the presence of DNA keys using a bottom-up approach [1]. Other new nanomaterials (nanoparticles and carbon nanotubes) have also been synthesized based on various bottom-up techniques.

For the top-down approach, an object is made from a large piece of material (bulk or thin films); the fabrication processing involves methods such as lithography and etching. Conventional lithography (photolithography, electron beam lithography, and others) is limited by the depth of focus. So,

it has been a challenge for scientists to find new ways for the fabrication of three-dimensional (3D) structures and devices. In recent years, many novel top-down approaches have been introduced as alternatives [2, 3]. Some methods are based on stamping technology [4], some are based on direct laser writing [5].

Another alternative way to create 3D objects at nanoscales relies on the folding of lithographic thin films. The technique was first introduced by V. Ya Prinz in 2000 [6]. The idea is to generate the folding of a planar structure by using thin-film stress. Simple structures such as tubes, spirals, and bent cantilever have been successfully demonstrated by this technique [7]. The miniaturization of nanofabrication is continually changing the way materials are used and applied.

In our research, we have studied the effects of ion irradiation on fixed and free-standing metallic thin films. The primary aims were: 1) to develop three-dimensional nanofabrication techniques, and 2) to study the folding of metallic thin films after being released from the substrate by selective (ion plasma) etching. Some experimental findings led to further studies of the effects of focused ion beam irradiation on the metallic films.

1.2.2 Microwave applications of nanomaterials

Computers and electronic devices are made of various types of materials: metals for signal lines, semiconductors for diodes/transistors, and magnetic materials for memory devices. The precise knowledge about the electronic and magnetic properties of materials is important in design and engineering processes. For example, in order to make a microwave antenna at a smaller scale, the material used must have a larger index of refraction, n. Since $n = \sqrt{\epsilon\mu}$ where ϵ is the electric permittivity and μ is the magnetic permeability, miniature antenna can be made of either high-μ magnetic or high-ϵ dielectric materials. Conventional ferromagnetic materials usually exhibit high magnetic permeability at low frequencies. But due to the presence of ferromagnetic resonances at high frequencies, the permeabilities of most materials are relatively low, $i.e.$ $\mu \approx 1$.

Conventionally, many FMR experiments have been conducted in a resonant cavity. The microwave was fixed at the resonant frequency of the cavity, and the FMR resonance is detected by sweeping the external magnetizing field until the lowest cavity Q-factor (absorption peak) is observed. Based on the cavity experiment, C. Kittel developed the FMR theory predicting the resonance condition in terms of the magnetizing

field. So far, most experimental studies on magnetic nanoparticles have been conducted by non-resonant transmission-line methods under zero external field [8, 9, 10, 11, 12, 13]. Only some experimental studies have included the effect of an external magnetizing field. Among those are the systematical studies of magnetic fluids done in the 1990's [14]-[15]. These investigations did not include micro-and nanoscopic studies of the constituent particles. In general, particles in a magnetic fluid may have various sizes and shapes; some may exhibit a single magnetic domain and some may not. Using new chemical synthesis methods [16, 17, 18], new magnetic nanoparticles can be made with narrow size distributions. In this research, fcc-cobalt and ϵ-cobalt nanoparticles are chosen for the experimental investigations at microwave frequencies. The experiments are done by measuring magnetic permeabilities over a broad range of frequencies in different magnetizing field.

For non-magnetic nanomaterials, carbon nanotubes provide an interesting object of study. They are known for their unique mechanical and electrical properties. A single-walled carbon nanotube (SWCNT) can be metallic or semiconducting depending on its chirality, while a multi-walled carbon nanotube (MWCNT) is usually a metal. With the aim to make electronic devices at smaller dimensions, engineers are motivated to find ways to shrink the interconnecting metallic lines in microchips. However, a reduction of the cross section of a wire results in an increase of Joule heat generation. High current densities in wires may also induce electromigration which leads to the generation of stress and failure of the electronic components [19, 20]. Unlike electric conductivity in metallic wires, the conductivity of carbon nanotubes does not follow Joule's law: the heating is generated at a significantly lower rate [21]. The unique electrical properties of carbon nanotubes allow realization of energy-efficient devices at smaller scales.

Besides the replacement of conventional metallic lines with carbon nanotubes, the new nanomaterials may also be used as shielding materials at microwave frequencies. Recently, an experimental study showed that a transparent SWCNT film with 90% optical transmittance has a shielding effectiveness (43 dB at 10 MHz and 28 dB at 10 GHz) higher than the requirement in the mobile phone communication industries [22]. In this work, we aim at investigating the microwave properties of both single-walled and multi-walled carbon nanotube materials. The objectives are 1) to measure the complex permittivities of single-walled carbon nanotube

composites at microwave frequencies, and 2) to study the anisotropy of aligned MCNT yarn membranes. The microwave measurements are done by using a transmission/reflection method or a resonant cavity.

1.3 Structure of the thesis

Chapter 2 of this thesis discusses how preliminary findings about the effect of ion processing on nanoscale metals have eventually led to the invention of new nanofabrication techniques that can be used to make complex three-dimensional metallic structures on the nanoscale. The new technologies are a hybrid between the state-of-the-art top-down approach and the energy-efficient self-organization in bottom-up processes. The main results of the research presented in Chapter 2 are included in Publications III and IV.

Next in Chapter 3, the effect of microwave radiation on nanoscale materials is discussed. This study is motivated by the fact that, in terms of technology, there are many applications for nanoscale materials at microwave frequencies. Chapter 3 focuses on scientific knowledge rather than on technological aspects. The research is divided into two parts: 1) development of microwave spectroscopy techniques and 2) characterization of nanoscale materials. Some of the main results presented in Chapter 3 are also discussed in Publications I, II, V, VI, and VII.

Chapter 4 presents a summary of the research work. Appendices give additional information on the microwave measurement techniques and some nanotechnological intrumentations used in this study.

2. Metallic Nanostructures under Ion Bombardment

This Chapter summarizes the research work that has been reported in Publications III-IV and presents a short review of scientific literature in the relevant research area.

2.1 Metals at reduced dimensions

2.1.1 The role of grain boundaries

Metals are usually found in the polycrystalline phase. A piece of bulk metal may be divided into three different regions: crystals, grain boundaries and surfaces. Usually, the number of atoms in the grain boundaries and surfaces is much smaller than the number of atoms in the crystals. Inelastic deformation involves the movement of dislocations or defects inside the crystals. The deformation dynamics at the grain boundary is assumed to be much smaller. However, for thin films (10s of nm), the number of surface atoms and atoms in the grain boundary will be comparable to the number of atoms in the crystals. Consequently, diffusion at the grain boundaries becomes a more prominent phenomenon for the inelastic relaxation [23].

A study made on 1 μm-thick Cu films shows that grain-boundary diffusion governs the stress relaxation at temperatures above 300 ^{o}C [24]. Other studies have demonstrated that, in contrast to coarse-grained materials, most of the plastic deformation in nanocrystalline metals is associated with atomic mobility at the grain boundaries [25, 26, 27]. For copper, the shift from dislocation-mediated plasticity in the coarse-grained material to grain boundary sliding occurs at a grain size of about 10 to 15 nanometers [28]. Besides deformation at the grain boundaries, dislocation nucleation at the free surface can also occur in atomic clusters. This

phenomenon helps sustain the plastic flow at the edge of clusters and materials at nanoscale [29].

Theoretically, electronic states of atoms in a crystal are completely different from those at a surface or grain boundary. Atoms in crystals are energetically more stable. Perturbing the states of a crystalline atom therefore requires a larger amount of energy than perturbing an atom on a surface. As a result, atomic diffusion from a metal surface into a grain boundary can occur at a much higher rate than atomic diffusion into a crystalline grain. Generally, there are a variety of ways (for example, mechanical stress, electrical stress, or radiation induced stress) to perturb an atomic state and generate atomic hopping/mobility. Although a metal can be isolated from many other external perturbations, atomic mobility can still occur through thermally induced diffusive process.

2.1.2 Technological applications

Technologically, low-dimensional or small-grain metals can be applied in many diverse areas. In the manufacturing sectors, such as in automobile industry, small grain metals are promising candidates for the processing of the so-called superplastic metals. Superplasticity is a phenomenon that is observed when a metal is heated to a phase-transition temperature. In 1999, S. X. McFadden, A. K. Mukherjee and their co-workers found that superplasticity can occur at a relatively low temperature in nanostructured nickel and metal alloys [30]. Their research results show that the mechanisms of superplasticity in nanocrystalline materials are fundamentally different from those in microcrystalline materials. Usually, nanocrystalline metals contain a larger volume fraction of grain boundaries. Atoms in a grain boundary are in non-crystalline phase. They can diffuse relatively faster to fill in gaps opened during the stretching, and so preventing the metal to break [31]. The ability to stretch metals at lower temperature can help reduce the energy cost of the manufacturer.

In the electronic industries, low-dimensional metals such as thin films are commonly used to make electrical components. A small deformation in thin films under the presence of an intrinsic stress can result in a fatal error or breakdown of the final device. It is therefore necessary to understand the inelastic deformation of thin metal films.

2.2 Conventional nanofabrication of metal nanostructures

Simple metallic nanostructures can be created by both top-down and bottom-up approaches. Publications III and IV present new techniques, which combine the advantages of the state-of-the-art top-down technology and the energy-efficient self-organization approach. The techniques can be applied to assemble complex three-dimensional nanostructures from lithographically defined thin films.

2.2.1 Bottom-up approach and self-organization

The bottom-up approach is a nanofabrication process involving the making of a macroscopic structure from small ingredients such as atoms or molecules. An ideal machine for the bottom-up approach would be a machine that can assemble matter (things) atom by atom. In nature, matter is formed in this way. The external environment and internal interactions act like a virtual machine, which transforms the matter upon the demand of nature. A study of pattern formation in ice [32] shows that the shape of a snow crystal is controlled by the humidity and temperature of the growth. Snow crystals growth at -15 ^{o}C and at high supersaturations result in the growth of plates and stellar dendrites, while a temperature of -5 ^{o}C and a moderately-high supersaturation (about 5 percent) lead to hollow column growth.

A self-organizing system is defined as a system in which a global pattern (order) emerges from the local interactions of the components (atoms, molecules, grains, etc.), starting from an initially disordered system. Self-organization in nature includes not only the formation of small things (e.g., snow flakes, metallic crystals), but also the emergence of phenomena such as the formation of evenly-spaced valleys in a mountain area [33].

In Chapter 3, magnetic nanoparticles and carbon nanotubes produced by bottom-up techniques are studied under microwave radiation. Magnetic nanoparticles are made by wet-chemical synthesis [16], and carbon nanotubes are grown by various other methods.

2.2.2 Top-down approach

In the top-down manufacturing process, smaller components are usually crafted from bigger pieces of materials. At human scales, top-down manu-

facturing usually involves cutting, stamping, welding, and bending. Welding uses heat to join pieces of metal together. At nanoscopic scales, welding is done, for example, by using electron-beam [34] or light [35]. Cutting is replaced by etching and lithography (with electron, photon or ion beam), while stamping is replaced by nanoimprinting technique [36]. For bending, mechanical methods can still be used, but it would require a nanoscale indenter (pressing) system. Alternative methods include the use of ion-beam to generate stress and induce the folding of free-standing films [37, 38, 39].

When designing complex structures at macroscopic scales, the final products are usually made by combining various techniques together, for examples, cutting and welding. At nanoscopic scales, the development of etching and lithography is far ahead of other techniques. Thus microtechnological devices have been designed and fabricated primarily based on these techniques.

Electron beam lithography (EBL) comprises three main processes: 1) coating a substrate by a resist, 2) exposing the resist with an electron beam and 3) developing the resist with a suitable chemical. In EBL, the exposure process or the patterning process is done by one pixel at a time using a modified scanning electron microscope (SEM). The resolution of EBL depends on the beam spot size and other factors related to the electron-resist interaction. Commercial EBL tools achieve a resolution well below 100 nm [40, 41].

The electron beam spot size used for an EBL process depends on the SEM operation. Usually, a commercial SEM consists of a source of electrons, a set of focusing electromagnetic lenses, a blanker to turn the beam on and off, a deflection system for moving the beam, a stigmator and apertures, see Appendix B. The electrons are generated from a source either by heating (thermionic source) or by applying an electric field (field emission source). The standard thermionic source is a loop of tungsten wire, but, today, lanthanum hexaboride (LaB_6) has become more widely used because of its higher brightness. LaB_6 has a lower work function, which means it can be operated at lower temperature (1800 K). Electrons are focused by normal and stigmator lenses. A stigmator is used to compensate for errors in e-beam focusing. A stigmator may be either electrostatic or magnetic. Typically, the de Broglie wavelength of electrons in an SEM is smaller than 0.01 nm. So, at the nanometer scale, diffraction is not the limiting factor. However, differences in electron velocity can lead to

chromatic aberration.

Although the electron beam spot size can be improved, the EBL resolution is still limited by the electron beam-resist interaction. When an energetic electron impinges on a resist, it loses its energy via a series of scaterring events. Some scattering may cause the electron to bounce back, creating a back scattered electron. Some scattering generates the emissions of secondary electrons and electromagnetic radiation. The scattering processes within the resist are the cause of the expansion of the exposure spot size. If the resist layer is thinner than the penetration range of the electrons, scattering at the resist-substrate interface should also be considered.

The electron-beam resists are high molecular-weight polymers dissolved in a liquid solvent. To deposit the resist over the substrate, we place a drop of the liquid onto the substrate and spin the substrate at 1000 to 6000 rpm. This process helps us getting a homogeneous layer of the resist over the substrate surface. After the spinning, the resist is dried by baking it on a hot plate. Note that it has been shown that sensitivity and contrast of the resists can be altered by prebaking either above or below the glass transition temperature [42].

During the exposure (patterning) process, the interaction with the beam of electrons modifies the resist in a way that makes it more soluble (positive) or less soluble (negative) in a developer. The pattern created after the development can be transferred to the substrate either by an etching process or a lifting-off process. In the lift off process, material is deposited on the substrate by various techniques such as evaporation and sputtering, and then the remaining resist is washed away by using a solvent such as acetone.

Besides planar nanostructures, EBL techniques also allows the fabrication of simple three-dimensional structures [43, 44]. The application of EBL is mainly in the mask-making and prototype nanofabrication. Typically, the produced masks are used in the replication of the patterns onto wafers.

Figure 2.1 shows how a free-standing metal film is created at a nanoscale by electron beam lithography. In Publications III and IV, the fabrication starts with the process of transferring a designed pattern from a CAD file onto a resist layer by exposing parts of the resist to electron beam. Either PMMA (polymethyl methacrylate) or copolymer or both resists are used depending on the dimensions of the pattern. Next, the exposed re-

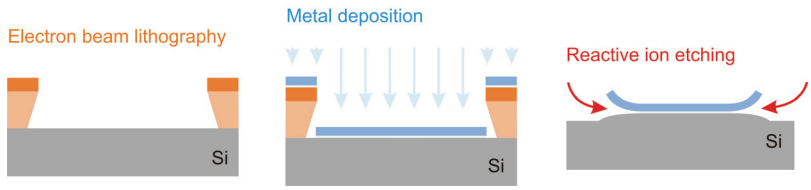

Figure 2.1. Fabrication of free-standing thin metal films by electron beam lithography and selective ion etching.

sist is removed from the substrate by dipping the whole substrate in a developer, made of a diluted solution of Methyl Isobutyl Ketone (MIBK) in Isopropanol (IPA). After the development, the unexposed part of the resist is left on the substrate. (In Publications III and IV, silicon is used as the substrate.) The resist layer is used as a mask in the metal deposition process. An electron-gun evaporator, with a pressure of about 10^{-6} mbar, is used to deposit metallic thin films of either low mobility (Al and Cu) or high mobility metals (Ti and Cr). After the metal deposition, unwanted parts are removed by immersing the whole substrate in acetone until the unwanted films are lifted-off.

2.3 Hybrid nanofabrication

The top-down (lithography based) technology described above allows the creation of complex structures, but the method is not considered practical for three-dimensional (3D) fabrication. Therefore, the self-organized bottom-up approach is more commonly applied to synthesize 3D nanostructures [1, 45, 46, 47, 48].

Alternative top-down approaches that have been used to fabricate complex 3D objects are, for example, direct laser writing [3], stamping [4], and additive 3D-printing technology.[1] However, due to the practical difficulties, these top-down approaches are not yet suitable for the creation of metallic structures at nanoscales.

Another way to fabricate metallic and semiconducting 3D nanostructures is to mimic the art of paper folding 'origami' [6, 49, 50, 51, 52, 53]. The idea is to apply lithography processes to fabricate an origami thin

[1]Additive manufacturing by 3D-printing technology is a process of making 3D solid objects from constitutive granular materials using a selective additive agent. During a 3D-printing process, a designed object is created layer by layer. Each layer is made by 2D-printing additive agent onto a thin layer of granular material.

film, and to release the film from the substrate so that the origami sheet can fold up according to either internal stress or external stimuli.

In nature, some living organisms like plants have evolved their organs as movable origami to increase their reproduction rate. A recent study on ice plant seeds reveals that the opening of the seed capsule does not involve any communication between cells, but is actually caused by a water-actuated strain [54]. The mechanism is governed by two main cell components: cellulose and lignin. Cellulose acts as water absorber, while lignin houses the cellulose in its elastic honey-comb network. After the rain, the cells are full of water, causing the expansion along the lid axis, and eventually the opening of the seed capsule.

As an energy minimization process, it is the path of relaxation that determines how a metallic origami film folds. The path is selected according to the mechanical constraints and the initial conditions of the system. For example, the final structure of a metal film formed by physical vapor deposition (PVD) is determined by energy relaxation processes during the cooling of metallic atoms on the substrate surface. The substrate acts as a mechanical constraint during the film growth. After the growth, if this constraint is removed, for instance by breaking the bonds along the film-substrate interface, the energy relaxation may cause the film to deform or even fold-up in the form of a curved sheet [55, 56]. Figure 2.2 shows examples of three-dimensional microstructures made by combining the top-down lithography with the self-organization of thin metal films.

In recent years, various 3D structures, such as pipelines, helices and tubes, have been successfully demonstrated by the hybrid top-down self-organization process [57, 58, 59]. The applications of these structures include biological research and optics [60, 61, 62].

2.4 Preliminary studies of stress-driven self-folding in thin films

In our experiments, we find that the deformation of a metal film and the curvature radius depend strongly on the boundary (structural geometry) of the film. Surprisingly, as shown in Fig. 2.3, the radius of curvature increases with the width of the strip.

Based on the elastic theory, the curvature radius of a thin Cr/Al/Cr film can be estimated, for example, by neglecting the effect of the adhesion

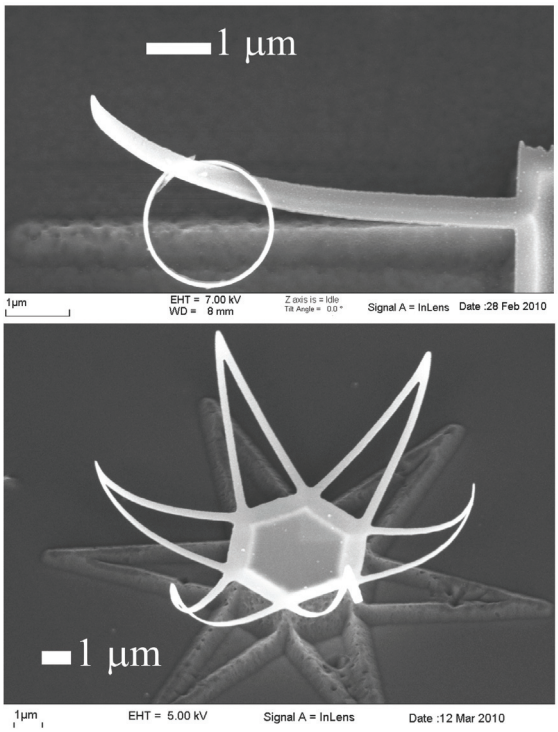

Figure 2.2. When releasing a Ti/Al bilayer film from the substrate by a reactive ion etching, the film curls up in the form of a curved sheet. Defining the boundaries of the film by a lithographic process allows the fabrication of three-dimensional structures at micro- and nanoscopic scales.

layer (the first 5 nm Cr) and applying the formula [63],

$$K = \frac{6E_f E_s (t_f + t_s) t_f t_s \epsilon}{E_f^2 t_f^4 + 4E_f E_s t_f^3 t_s + 6E_f E_s t_f^2 t_s^2 + 4E_f E_s t_f t_s^3 + E_s^2 t_s^4}, \qquad (2.1)$$

where t_f is the film thickness, E_f is the film elastic modulus, t_s is the substrate thickness, E_s is the substrate elastic modulus, $\epsilon = \Delta T(\alpha_s - \alpha_f)$ is the misfit strain due to different thermal expansions of the film and the substrate during film growth, α_f and α_s are the thermal expansion coefficients of the film and substrate, respectively, α_s is the substrate thermal expansion coefficient, and ΔT is the temperature change during the film growth. If we define a 20 nm Cr layer as the film, and a 25 nm Al layer as the substrate, this simplified model predicts a curvature radius of about 18.6 μm.[2]

The initial-strained bilayer model yields a correct order of magnitude for the curvature radius, but it cannot explain the strong width-dependent curvature. Note that the strain within the deposited thin film is assumed

[2]The calculation is done using the bulk properties of the metals, and assuming that ΔT is 90 K.

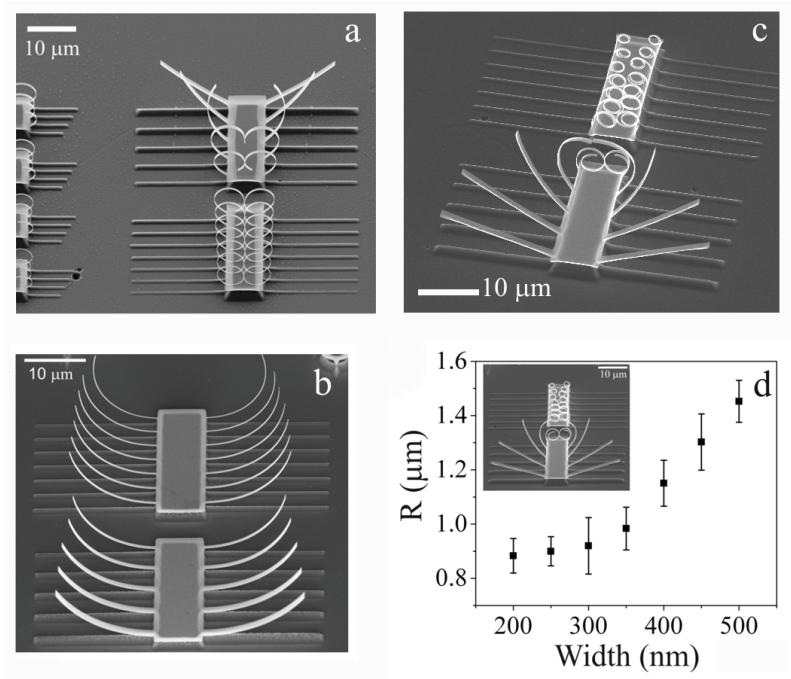

Figure 2.3. SEM images of metallic thin films with strong width dependence curvatures. The strip widths are varied from 200, 250, ... 500 nm, and 600, 800, ... 1400 μm. The films were released from the silicon substrate by reactive ion etching process. a) Scanning electron microscope (SEM) image of self-rolling strips made of a Ti5nm/Al30nm/Cr20nm film. b) SEM images of self-organized bending of 5nm/25nm/20nm Cr/Al/Cr strips. c) SEM images of self-folding 25nm/25nm Ti/Al film. d) Radius of curvature as a function of the width of the Ti/Al strip shown in Figure c. (Some figures are from Publication V.)

to be caused by the difference in thermal expansion between the two layers. The calculation indicates that the radius of curvature is inversely proportional to ΔT, so when ΔT is increased from 50 K to 200 K the radius of curvature decreases from 23.9 μm to 8.36 μm.

The elastic model cannot describe the width-dependent curvature as observed in Fig. 2.3. Biaxial deformation may be the cause of the width dependence. To test whether this hypothesis is correct, a simulation based on the finite element method was done [64]. It was found that the simulation with biaxial strain (ΔT was assumed to be 120 K) gives only a 5-percent reduction of the curvature radius when the strip width is reduced from 1400 nm to 200 nm (13.8 μm for the 200 nm strip, and 14.5 μm for the 1400 nm strip). Note that the closed-form solution in [64] gives a radius of 13.8 μm, regardless of the width. All the analyses demonstrate that the deformation cannot be described by elastic theory. So the stress of the film may relax via both elastic and inelastic processes.

2.5 The role of inelastic relaxation

If the folding of thin metal films involves both elastic and inelastic relaxation, the folding must be governed by different relaxation times: one for the elastic process and another for the inelastic relaxation. In principle, the inelastic time is longer. To test whether the relaxation times play a significant role in the folding of metal films, two identical samples (25nm/25nm Ti/Al planar structures on silicon substrates) were made. The first sample was released from the substrate at a slower rate using a reactive ion etching (RIE) process. The second was released from the substrate at a faster rate using an inductively coupled plasma reactive ion etching (ICP-RIE). Figure 2.4 shows the results of the experiment.

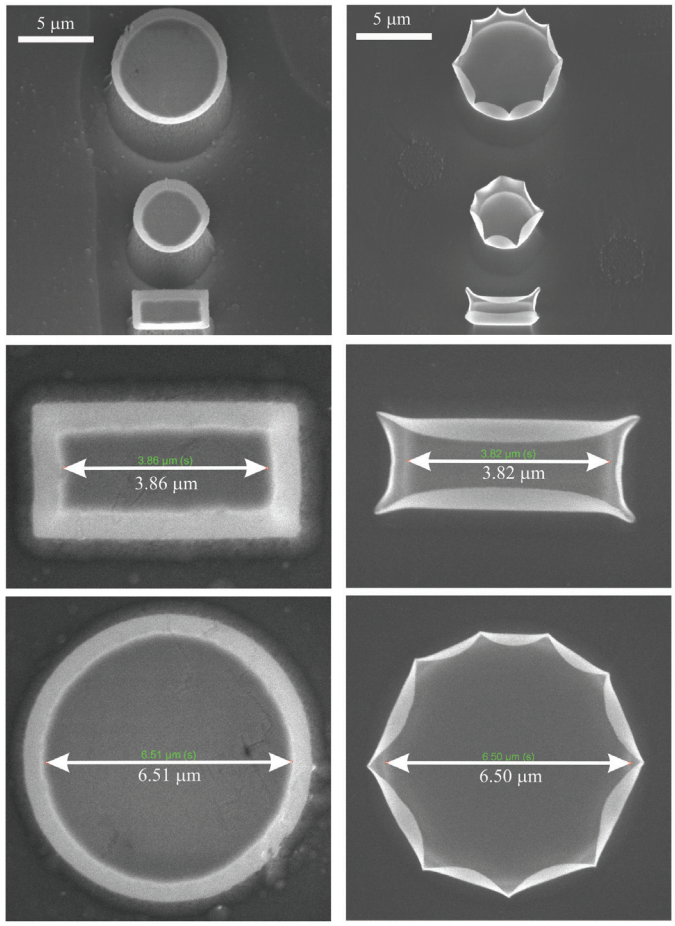

Figure 2.4. SEM images showing deformation of metal films after being processed by RIE (left column) for 3 min 20 s (SF_6 30 sccm, O_2 5 sccm, pressure 100 mTorr, RF power 80 W), and ICP-RIE (right column) for 22 seconds (SF_6 40 sccm, pressure 10 mTorr, RF power 3 W, ICP power 1000 W).

Experiments with strip line structures agree well with the results shown in Fig. 2.4. In summary, a metal strip will fold at a smaller radius of curvature if it is released (free) at a faster rate, see Figs. 2.5 and 2.6. This experimental finding suggests that inelastic relaxation must play a significant role in the deformation process.

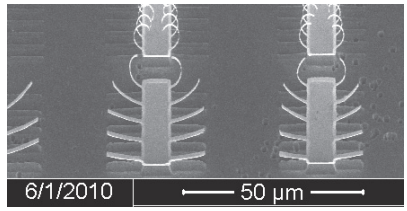

Figure 2.5. SEM images showing the curvature of 26nm/26nm Ti/Al metal strips after being processed by RIE (left column) for 3 min 40 s (SF_6 30 sccm, O_2 5 sccm, pressure 100 mTorr, RF power 80 W).

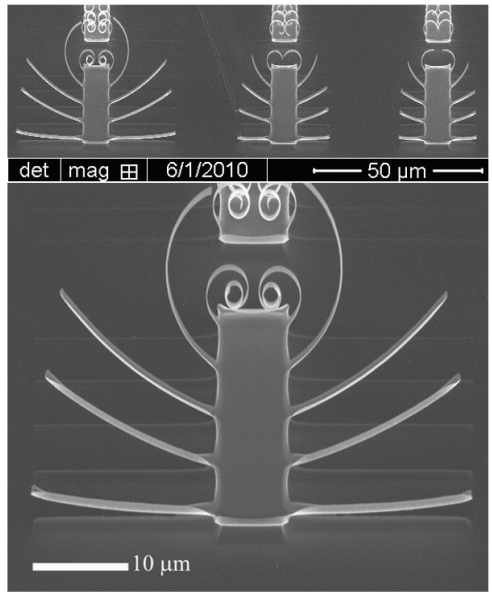

Figure 2.6. SEM images showing the curvature of 26nm/26nm Ti/Al metal strips after being processed by ICP-RIE (right column) for 22 seconds (SF_6 40 sccm, pressure 10 mTorr, RF power 3 W, ICP power 1000 W).

Note that the elastic and inelastic relaxation rates are of different orders of magnitude, see Supplementary Information in Publication IV. Regarding experimental time scales, the total RIE etching time is approximately two hundred seconds, so the widest strip is released approximately 100 seconds after the narrowest one. In principle, complex structures with different curvature radii can be fabricated with a single etching process if the effect of inelastic relaxation is taken into consideration.

2.6 Evidence of ion-induced plastic strain

The effect of structural geometry (boundary condition) is not so strong in the case of Cr/Al/Cr metal films (Fig. 2.3b), but when Ti is used as the bottom layer of the film, the effect is enhanced considerably (Fig. 2.3a). The experiment therefore shows that the inelastic deformation is increased if the bottom layers of the films are composed of Ti. Analysing the Al/Ti bilayer strips shown in Fig. 2.3c using energy-dispersive X-ray spectroscopy (EDX) shows that the strips are composed mainly of Al. Figure 2.7 shows the EDX spectrum of a narrow strip taken from the Ti/Al sample. Besides Al, we also observe Cu (from TEM grid), F (from SF^6) and O peaks. The amounts of F and O are very small, but still higher than the amount of Ti. Wider strips from the same Ti/Al sample also show almost no sign of Ti.

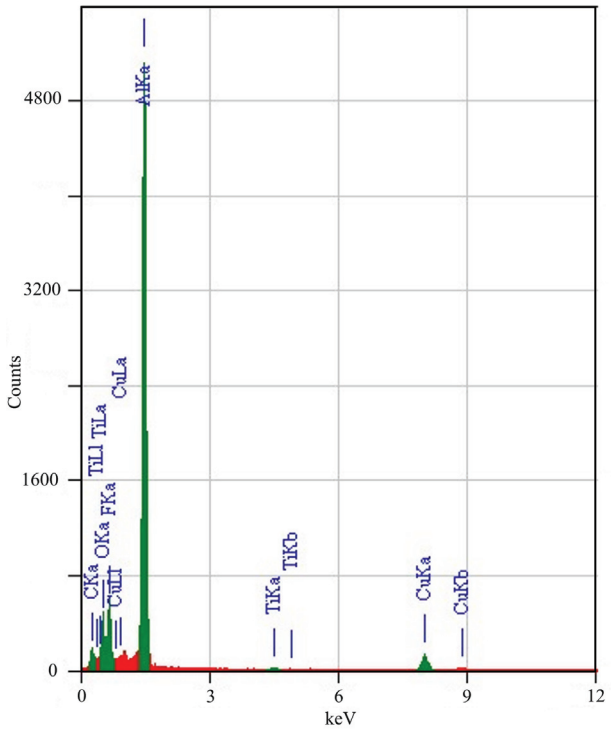

Figure 2.7. An EDX spectrum of a folded strip shown in Fig. 2.3c. The remaining film is composed mainly of Al; the Ti peak is absent from the spectra. The EDX peaks of chosen elements (Al, Ti, Cu, F, O) are highlighted with green color.

Figures 2.8 and 2.9 respectively show the TEM images of the remaining Al film in the narrow strip and a wider strip. The Al film has nanocrystalline structure; some crystals of the size below ten nanometers are observed. Near the edge of the strip, an amorphous phase is also found.

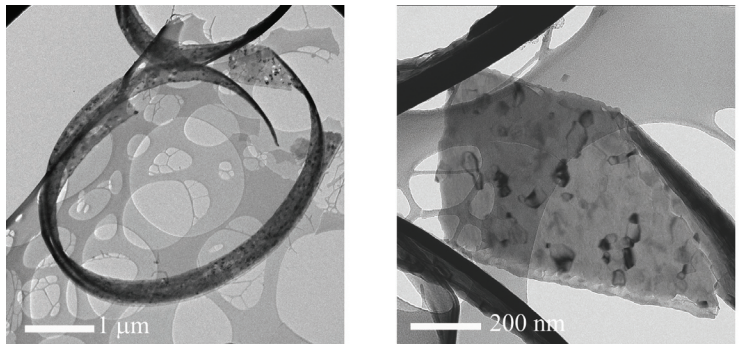

Figure 2.8. Transmission electron microscopic (TEM) images of a narrow Ti/Al strip taken from the sample presented in Fig. 2.3c.

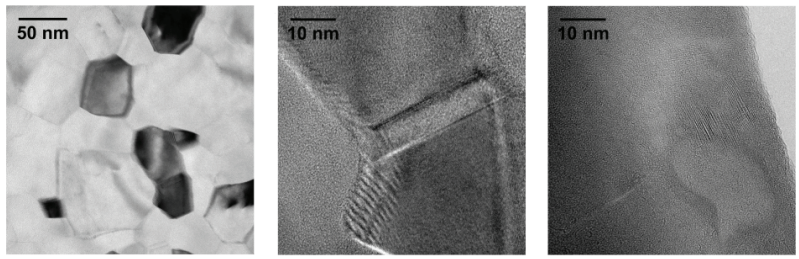

Figure 2.9. Transmission electron microscopic (TEM) images of a wide Ti/Al strip taken from the sample presented in 2.3c. The EDX spectrum shows that the film is composed mainly of Al. (Figures are from Publication IV.)

Generally, compressive stress in polycrystalline films is caused by adatom insertion into the grain boundary [65]. Our experiment shows that the reaction of Ti with ions during the etching process may increase the chemical potential of atoms at the Ti/Al interface, and therefore results in atomic flow into the surrounding grain boundaries, as discussed in Publication IV. If the film is still fixed on the substrate while the etching occurs, adatom insertion into the grain boundary will be limited by the accumulated compressive stress.

The effect of boundary condition on inelastic deformation can also be found in nature. For example, if we cut a dandelion stem into small strips and put them in water, the strips will fold, see Fig. 2.11. This is due to the difference in the water absorption between the inner and outer parts of the stem. In case of our metallic strips, the grain boundaries 'absorb' atoms from the bottom surface during a reactive ion etching process. This absorption causes the strip to fold upward. The strong width-dependent curvatures occur because of the effect of geometrical boundary. Fixed local

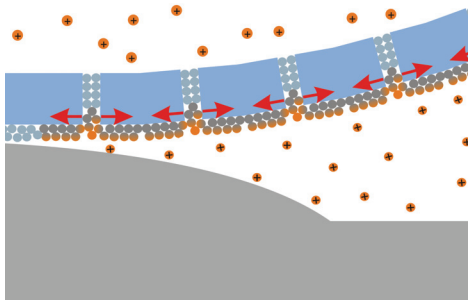

Figure 2.10. Cartoon picture describing the generation of compressive strain during a reactive ion etching process.

boundaries can limit the absorption rate and consequently slow down the bending in bigger structures.

Figure 2.11. Folding of dandelion stem in water.

2.7 3D-assembly with reactive ion etching

The ion-induced inelastic relaxation, described in the previous section, provides a new concept for three-dimensional (3D) assembly at micro and nano scales. The folding of a thin metal strip by this new technique does not require a large initial strain or intrinsic stress. The metal strip can be folded solely by the inelastic relaxation of accumulated compressive stress. In practice, the assembly may involve both elastic and inelastic processes.

An RIE-assisted self-assembly is done for example by fabricating two sacricial layers. In our experiments, silicon (Si) substrate is the primary sacrificial layer, and titanium (Ti) is the secondary layer. The role of the first sacrificial layer is to release the film from the substrate, and also to create the free boundary region. The second sacrificial layer is used to generate compressive stress in the adjacent metallic layer.

Figure 2.12 shows particle traps fabricated by incorporating ion-induced inelastic strain. The etching of the Ti layer increases the chemical potential of atoms at the interface between the Ti and Al layers. So, some atoms are driven into the grain boundaries within the upper Al layer, generating a compressive stress and bending of the film. A mathematical model of the process is discussed in Publication IV.

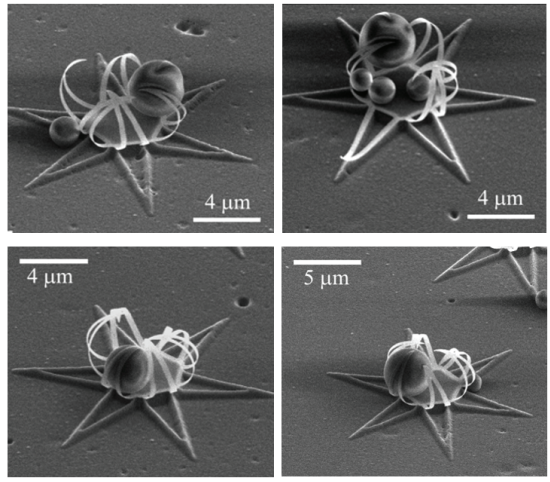

Figure 2.12. SEM images of particle traps and captured lactosed microparticles. The metallic traps are assembled from lithographic thin Ti/Al/Cr films. (Some of the figures are from Publication IV)

2.8 3D-assembly with focused ion beam

Publications III and IV report experimental evidence that free-standing metal films can be bent locally with focused ion beam. Basically, the impact of high energy ions on thin metal films is similar to how a gun-pellet impacts a metal sheet. Firing high-energy ions into metal thin films causes the film to deform. Figure 2.13 shows how the ion beam can be used to assemble a complex three-dimensional (3D) microstructure from a lithographic thin film.

From the preliminary studies of the effect of focused ion beam, reported in Publication III, we initially speculate that by applying the ion-beam prior to the etching process, the self-folding could also be activated at later time. But, in later experiments, we find that the inelastic bending caused by an FIB process is much smaller if the ion beam is applied on a fixed metallic membrane.

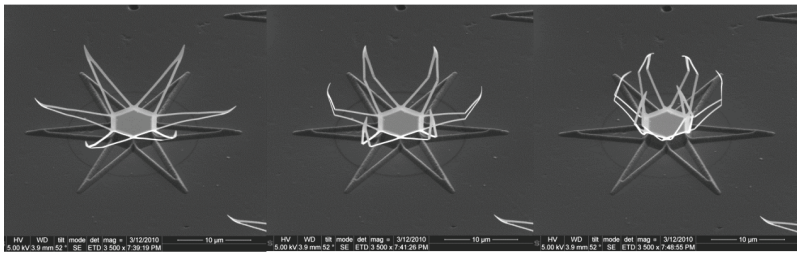

Figure 2.13. SEM images show the folding of a microcage using focused ion beam.

The ion-beam operation was done in an SEM/FIB dual beam microscope (Helios Nanolab 600, the equipment combines a scanning electron microscope and a focused ion (Ga^+) beam microscope). In order to bend a thin metal film into a designed 3D structure, we need to shoot the ions continuously along an intended fold line. With the advancement of ion-beam technology, it has become possible to focus ions at nanoscale resolution. So the curvature radius of the folded part can be in the order of 10 nm, which allows the assembly of complex 3D structures at nanoscale. Figure 2.14 shows the FIB-assisted assembly of a nanobox.

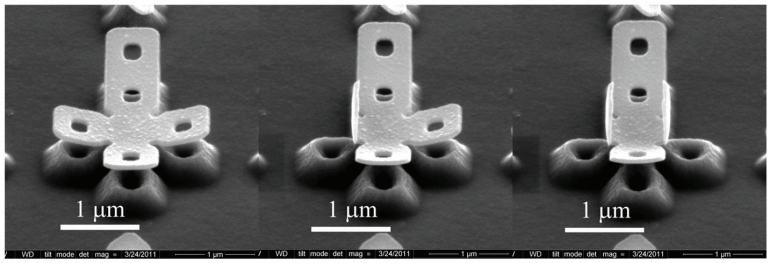

Figure 2.14. SEM images show the folding of a nanobox using focused ion beam.

Rotating the sample holder may be necessary if the area that we intend to fold is blocked by the other parts of the sample. For a nanobox like in Fig. 2.14, the folding of the face connecting the bottom and the cover of the box (see Fig. 2.15) was done after a rotation of the sample holder.

In Publication IV, we present an experimental investigation of the bending induced by an FIB process. The studies were done by using transmission electron microscope (TEM) and energy dispersive X-Ray (EDX) analysis. The TEM samples were made of a 50-nm Al thin film. Figure 2.16 shows how the TEM samples were prepared.

The EDX/TEM analysis shows that some impinged Ga^+ ions are embedded inside the Al matrix near the back surface of the film, see Figure 2.17. The simulated results based on the SRIM calculation [66], presented in

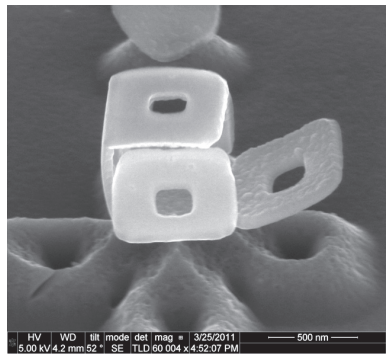

Figure 2.15. An SEM image of a nanobox made from lithographic Al film.

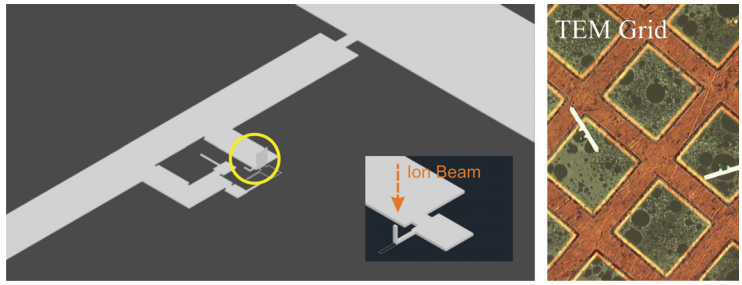

Figure 2.16. Preparation of the TEM sample. After FIB processing, the sample is picked up and placed on top of a TEM grid by using a hydrolic micromanipulator.

Publication IV and Appendix B, show that the ion range is comparable to the thickness of the film. The plastic flow of both ions and atoms from the front to the back surfaces of the film is hypothesized as the main cause of the compressive stress, and the local bending of the film. Our experiments on Al thin films with different thicknesses, from 10 to 50 nm, show that the Ga^+ processing at 30 keV always causes the films to bend up towards the beam.

Figure 2.18 shows the schematic illustration of a heuristic model describing the FIB-assisted self-assembly process. The mathematical model of the bending mechanism is presented in Publication IV.

2.9 Conclusions

The experimental studies of free-standing thin metal films presented in this chapter and in Publication III - IV support the following scenarios for ion-induced plastic deformation: a) If the surface of a metal film is reactive to the ions during a reactive ion etching process, the ion processing can cause near surface compressive stress and a significant plastic defor-

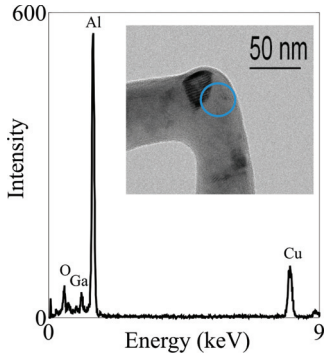

Figure 2.17. An EDX spectroscopy measurement at the area marked by a circle in the TEM image shows a trace of embedded Ga^+ ions near the back surface of the folded region. (The figure is from Publication IV)

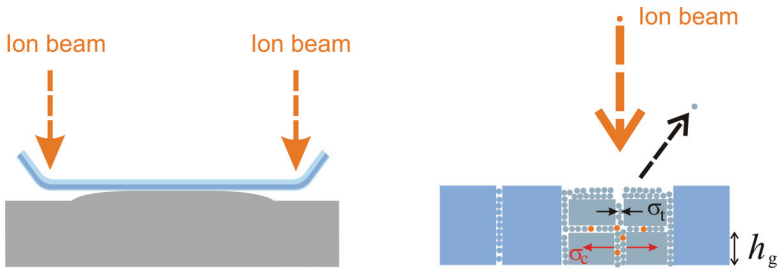

Figure 2.18. A schematic illustration of a heuristic model describing the FIB-assisted self-organization and bending of a thin metal film. (The figures are from Publication IV)

mation. b) If the range of ions of a focused ion beam is comparable to the thickness of an irradiated metal film, the bombarding ions can cause the flow of atoms and ions towards the back surface of the film; this phenomenon then induces plastic deformation and an upward bending of the film.

Our experimental results demonstrate that ion-induced plastic strain can be used to control the folding of free-standing metallic films with unprecedentedly high precision. The reactive ion etching process provides an efficient method for the generation of near-surface plastic strain in free-boundary metal films. We have shown that the folding of metal strips with different radii of curvatures can be done in a single etching process. With focused ion beam technology, a radius of curvature as small as 10 nm has been achieved.

3. Nanostructured Materials under Microwave Radiation

This Chapter summarizes the research work that has been reported in Publications I, II, V, VI, VII and presents a short review of scientific literature in the relevant research area. The investigation of the microwave properties of nanoscale materials is presented and discussed. The materials being tested include composite materials made from magnetic nanoparticles, multi-walled carbon nanotube yarns, and carbon nanotube composites.

3.1 Microwave radiation

Besides the cosmic microwave background radiation (CMB), we are also surrounded by other sources of the microwave radiation leaking from household electronic equipments, ranging from computers (2 to 4 GHz), mobile devices (3 GHz) to microwave ovens (2.4 GHz). A material interacts with microwave through exchange of energy determined by the electronic (quantum) states of the electrons inside the material. These states are fundamentally described by quantum mechanical principles, but in this chapter, the radiation is modelled as classical fields.

In this classical framework, the electric and magnetic responses of a material are described in terms of intrinsic parameters, such as relative permittivity and relative permeability. Generally, the scattering of microwave at different parts of a material can lead to the occurrence of interference phenomena. However, for materials with nanoscale subunits or heterogeneities, microwave wavelengths (approx. 30 cm at 1 GHz and 3 cm at 10 GHz in free-space) are large compared to the distances between two scatterers. So, theoretically one can assume that interference can be excluded from the analysis.

3.2 Measurement methods

The microwave methods and instrumentation include both resonant and non-resonant microwave spectroscopy techniques. In this chapter, the resonant cavity is applied to characterize samples made of multiwalled carbon nanotube yarns, and the non-resonant methods (Publications I and V) are used in the characterization of magnetic nanoparticles. The primary non-resonant method used in this work is a transmission/reflection technique reported in Publication I. The method allows for the determination of material parameters regardless of the sample position, so errors in the reference plane position are eliminated [67]. The experiments were done by measuring the complex electric permittivity and magnetic permeability of the samples in the frequency range between 0.5 and 18 GHz, allowing the observation of magnetic resonant phenomena under a fixed magnetizing field. Figures 3.1 and 3.2 demonstrate how the microwave measurements were conducted.

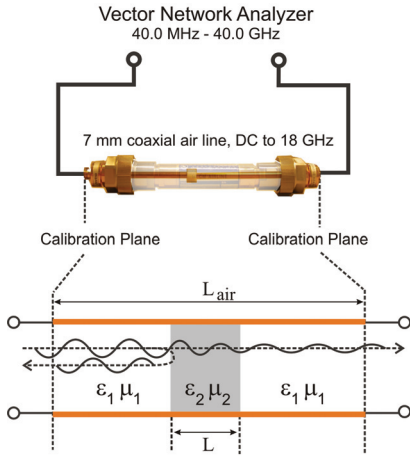

Figure 3.1. The transmission/reflection measurement setup used to measure the material's constitutive parameters.

3.2.1 Transmission/reflection technique

To derive the mathematical relation between transmission/reflection signals and the refractive index, we describe the scattering of electromagnetic waves based on the multiple reflection model shown graphically in Fig 3.3. Since a transverse electromagnetic (TEM) wave traveling a distance L exhibits a phase change of $2\pi L/\lambda$, where λ is the wavelength in that region, the propagation factor of the TEM wave traveling through a

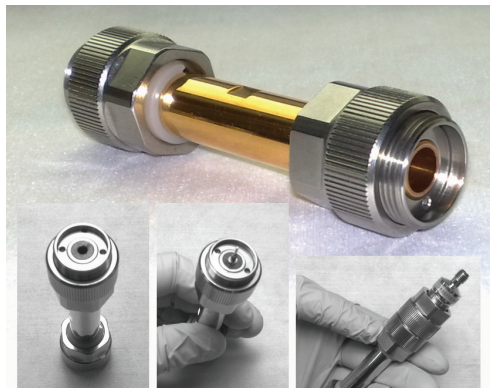

Figure 3.2. The insertion of a magnetic nanocomposite sample into the sample holder (precision coaxial airline) for the transmission/reflection measurement.

sample is given by

$$P = e^{-\gamma_2 L}, \tag{3.1}$$

where $\gamma_2 = i\omega\sqrt{\mu_r \epsilon_r}/c$, and L represents the length of the sample.

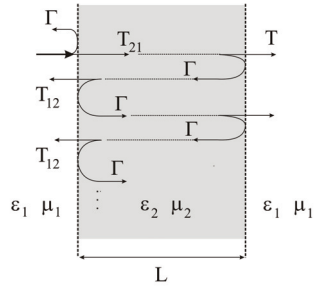

Figure 3.3. The model of multiple reflection between two interface

The total reflection coefficient is

$$\begin{aligned} \Gamma_{\text{tot}} &= \Gamma + T_{21}T_{12}\Gamma P^2 + T_{21}T_{12}\Gamma^3 P^4 + \ldots \\ &= \frac{\Gamma(1-P^2)}{1-\Gamma^2 P^2}, \end{aligned} \tag{3.2}$$

where

$$\Gamma = \frac{1-\sqrt{\frac{\epsilon_2\mu_1}{\epsilon_1\mu_2}}}{1+\sqrt{\frac{\epsilon_2\mu_1}{\epsilon_1\mu_2}}}, \tag{3.3}$$

and

$$T_{12} = \frac{2}{1+\sqrt{\frac{\epsilon_1\mu_2}{\epsilon_2\mu_1}}} = \sqrt{\frac{\epsilon_2\mu_1}{\epsilon_1\mu_2}}\, T_{21}. \tag{3.4}$$

Similarly, the total transmission coefficient in terms of Γ and P is

$$T_{\text{tot}} = \frac{P\,(1-\Gamma^2)}{1-\Gamma^2 P^2} \tag{3.5}$$

The transmission and reflection through a sample of length L inserted at any arbitary location in a perfect transmission line can be described by the cartoon shown in Fig. 3.4. The transmission line is divided into three regions. The regions of lengths L_1 and L_2 are assumed to be filled with air and the middle region of length L is filled with a material with the relative permittivity, $\epsilon_r = \epsilon/\epsilon_0$, and relative permeability, $\mu_r = \mu/\mu_0$. The complex refractive index of the material is $n = \sqrt{\mu_r \epsilon_r}$. The permittivity ϵ_1

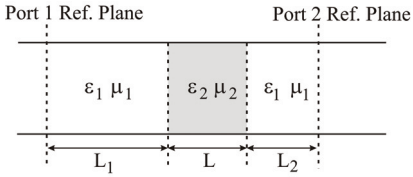

Figure 3.4. The model of a transmission line containing a material of length L. L_j represents the distance between the reference plane of the measurement to the first interface between air and material under test. (Figure from Publication I)

and permeability μ_1 of the space in front of the material can be assumed to be those of the air or free space, $i.e.$ ϵ_0 and μ_0. So,

$$\Gamma = \frac{1 - \sqrt{\frac{\epsilon_r}{\mu_r}}}{1 + \sqrt{\frac{\epsilon_r}{\mu_r}}}. \tag{3.6}$$

Based on the multiple reflection model, we can write the scattering parameters (see Appendix A) in terms of Γ and P as follows

$$S_{11} = e^{-2\gamma_1 L_1}\Gamma_{\text{tot}} = e^{-2\gamma_1 L_1}\frac{\Gamma(1-P^2)}{1-\Gamma^2 P^2}, \tag{3.7}$$

$$S_{22} = e^{-\gamma_1 L_2}\Gamma_{\text{tot}} = e^{-\gamma_1 L_2}\frac{\Gamma(1-P^2)}{1-\Gamma^2 P^2} \tag{3.8}$$

and

$$S_{21} = S_{12} = e^{-\gamma_1(L_1+L_2)}T_{\text{tot}} = e^{-\gamma_1(L_1+L_2)}\frac{P(1-\Gamma^2)}{1-\Gamma^2 P^2}. \tag{3.9}$$

If there is no sample inside the airline, S_{21} is reduced to

$$S_{21}^o = e^{-\gamma_1 L_{\text{air}}}, \tag{3.10}$$

where $L_{\text{air}} = L_1 + L_2 + L$ is the length of the sample holder (7-mm coaxial air line).

The full derivation of the reference-plane invariant (RPI) algorithm began with the definition of two RPI parameters:

$$A = \frac{S_{11}S_{22}}{S_{21}S_{12}} = \frac{\Gamma^2}{(1-\Gamma^2)^2}\frac{(1-P^2)^2}{P^2}, \tag{3.11}$$

$$B = S_{21}S_{12} - S_{11}S_{22} = e^{-2\gamma_1(L_{\text{air}}-L)}\frac{P^2-\Gamma^2}{1-\Gamma^2 P^2}, \tag{3.12}$$

which give (see Publication I)

$$\Gamma^2 = \frac{-A(1+B^2)+(1-B)^2}{2AB} \pm \frac{\sqrt{-4A^2B^2+[A(1+B^2)-(1-B)^2]^2}}{2AB}, \tag{3.13}$$

where the correct solution is the one that satisfies $|\Gamma| \leq 1$. The physical descriptions of S_{ij}, Γ, and P are given in Appendix B.

Besides Γ, it is also necessary to express P in a form that does not require the knowledge of L_1 and L_2. The derivation as presented in Publication I gives

$$P = R\frac{1+\Gamma^2}{1+B\Gamma^2}e^{-\gamma_1 L}, \tag{3.14}$$

where

$$R = \frac{S_{21}}{S_{21}^o} = \frac{e^{\gamma_1 L}P(1-\Gamma^2)}{1-P^2\Gamma^2}. \tag{3.15}$$

From Eqs (3.13), (3.14), and (3.15), the refractive index can be determined

$$n = \sqrt{\epsilon_r \mu_r} = \frac{1}{\gamma_1 L}\ln\left(\frac{1}{P}\right). \tag{3.16}$$

The logarithmic function in Eq. (3.16) is multi-valued, therefore the equation has an infinite number of solutions. The physically correct solution must be chosen. Principally, there are many ways to find the correct solution. In this thesis, the solution was chosen by checking whether a chosen root gives the correct value for the group delay. Group delay is a measure of the pulse signal transit time through a transmission line. Theoretically, the transit time of a wave packet is given by

$$\tau_{\mathrm{g}} = \frac{x}{v_g}, \tag{3.17}$$

where x is the transit length and v_g is the group velocity of the wave pulse. So, for a transit through free space, we have

$$\tau_{\mathrm{g}}^o = \frac{L_1+L+L_2}{c}, \tag{3.18}$$

while a transit through a material takes a time interval of

$$\tau_{\mathrm{g}} = \frac{L_1+L_2}{c} + L\frac{d}{df}\left(\frac{fn}{c}\right). \tag{3.19}$$

where τ_{g}^o is the group delay through an empty line, and τ_{g} is the group delay through the sample of length L. By subtracting Eq. (3.19) from Eq. (3.18), one obtains a function, τ, that does not depend on L_1 and L_2.

$$\tau = \frac{L}{c}\left[1-\frac{d}{df}(fn)\right]. \tag{3.20}$$

By comparing the calculated τ with the measured τ, one can then determine the correct root for the refractive index.

As discussed before, the determination of the complex permittivity ϵ_r and permeability μ_r is equivalent to the determination of the complex refractive index $n = \sqrt{\mu\epsilon}$ and wave impedance $Z = \sqrt{\mu/\epsilon}$. Since $Z = \frac{1+\Gamma}{1-\Gamma}$ and Γ is described by Eq. (3.13), we can express the wave impedance analytically regardless of the reference-plane position. The measurements of the S-parameters and group delays can be done by using a vector network analyzer.

Besides the observation at microwave frequencies, other experimental methods are used to characterize the materials under investigation. Experiments include SQUID (superconducting quantum interference device) magnetometry, direct-current (dc) measurements, X-ray diffraction (XRD), transmission electron microscopy (TEM), scanning electron microscopy (SEM), and magnetic force microscopy (MFM).

3.3 Ferromagnetic nanoparticles

Materials that are affected by magnetic fields are generally known as magnetic materials. In some metals, electrons are so strongly correlated that within a certain length their symmetries are spontaneously broken, resulting in different types of magnetic orderings, namely ferromagnetism, paramagnetism, superparamagnetism, anti-ferromagntism, and ferrimagnetism. The manifestation of these quantum collective phenomena, that lead to magnetic states, depends very much on environmental factors such as temperature, magnetic field, and pressure.

Ferromagnetism is an ordered state of matter characterized by the parallel magnetic moments of all electrons inside a certain domain called magnetic domain. At room temperature, some 3d transition metals (iron Fe, cobalt Co, and nickel Ni) are ferromagnetic. Above a temperature threshold, thermal energy can perturb and excite the energy states of electrons and destroy the parallel moments inside the ferromagnetic domain. However, the magnetic moments can be brought back into an ordered parallel state if a sufficiently large magnetic field is applied.

Paramagnetism is a state of magnetic materials where the magnetic moments of electrons are randomly oriented in the absence of a magnetizing field due to thermal excitation. But, under the presence of a magnetic field, the electrons will be forced into an ordered state with parallel magnetic moments. Anti-ferromagnetism is a special ordered state of matter when the next nearest magnetic moments point in the opposite direction,

in the way that the total magnetic moment is zero. Ferrimagnetism is a subset of anti-ferromagnetism, the difference is that one direction of the magnetic moments is stronger than the other leading to a non-zero magnetization.

Electrons in a magnet can be either localized (like in insulators) or delocalized (like in metals). Magnetic materials with localized electrons, for example molecular magnets, are called local-moment magnets, while magnetic materials with delocalized electrons are itinerant magnets. In a metallic ferromagnetic material, electrons can be both localized and delocalized. Fundamentally, all the magnetic states are the manifestation of quantum collective phenomena. The presence of a magnetic state depends strongly on the environment; factors such as temperature, magnetic field, and pressure can cause a transition from one magnetic state to another.

In nanostructured magnetic materials, the energy states of electrons can be strongly affected by the surface and interface energy. For example, below a certain size (usually of the order of a hundred nanometers), a ferromagnetic particle can change into a so-called superparamagnetic particle. In a superparamagnetic state, the electrons' magnetic moments are vibrating randomly (flipping) because of thermal energy. If the magnetization of the particle is measured in the absence of an external magnetic field at a frequency that is lower than the flipping frequency[1], the magnetization at the measurement frequency will be zero.

A uniaxial magnetic particle can be described by using a double-well anisotropy energy model: $E_a = K' \sin^2 \theta$, where K' is the anisotropy constant, θ is the angle between the magnetization direction and the principal axis of the crystal. Classically, the model predicts two stable magnetization states. However, in addition to the anisotropy energy, a magnetic moment m in the presence of an applied field H also possesses the energy $E_B = -\vec{m} \cdot \mu_0 \vec{H} = -m\mu_0 H \cos\theta$, where $\mu_0 = 4\pi \times 10^{-7}$ T.m/A is the magnetic constant (permeability of free space). Figure 3.5a shows how the total energy of a uniaxial particle changes when an external static field H is applied.

At a low temperature, the magnetization is blocked in one of the two states, $i.e.$ the ferromagnetic state. As the temperature increases, ther-

[1] In 1949, L. Néel proposed that the flipping period of a magnetic moment may be described by $\tau_N = \tau_0 e^{\frac{KV}{k_B T}}$, where τ_N is the Néel relaxation time, τ_0 is the attempt time, KV is the energy barrier which is a product of the magnetic anisotropy energy density K and the particle volume V, k_B is the Boltzmann constant, and T is the temperature.[68]

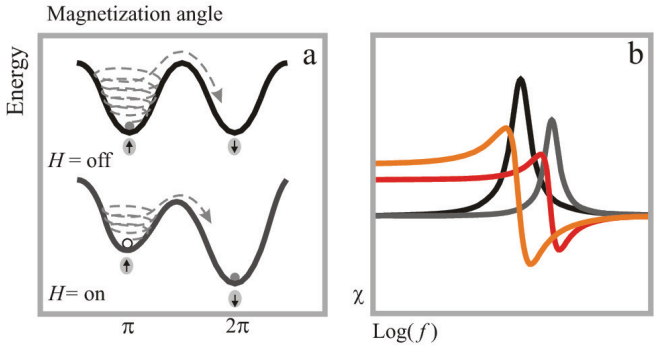

Figure 3.5. a) The cartoon presents the classical double-well potential of a uniaxial magnetic particle. An applied alternating field induces oscillations of magnetization in the wells. When the field frequency matches the precessional frequency of the magnetization, the system is excited and energy is pumped into the system, and eventually the magnetization direction is reversed. b) The complex magnetic susceptibility $\chi = \chi' - i\chi''$, predicted by the Landau-Lifshitz-Gilbert equation. When a static field H is applied, the resonance peak shifts towards a higher frequency. Here, the orange and red lines are χ' when H is off and on, respectively, while the black and grey lines are the corresponding χ''. (From Publication VI.)

mal energy can overcome the magnetic energy barrier. This thermal excitation leads to the switching of the magnetization direction, and a transition between the ferromagnetic and superparamagnetic phases. The temperature at which the magnetization starts to fluctuate is called the superparamagnetic blocking temperature T_B.

Small particles may become superparamagnetic even at room temperature. This observation implies that the anisotropy energy is proportional to the particle volume. Mathematically, this can be described as [69]

$$E_a = K' \sin^2\theta = KV \sin^2\theta, \tag{3.21}$$

where K is the anisotropy constant (energy per unit volume), and V is the particle volume. Based on this definition, K can be estimated from the blocking temperature, $i.e\ KV \approx k_B T_B$.

Similar to a rapidly spinning top that precesses around a gravitational field, the magnetization of a particle also precesses around an applied magnetic field. However, Kittel's FMR theory states that, in addition to the external applied field, we should also consider magnetic anisotropy and the associated 'demagnetizing' field H_a. (Demagnetizing field is defined as the field generated by the magnetization inside a magnet.)

The equation of motion, $\tau = \vec{m} \times \mu_0 \vec{H}_{tot}$, allows the derivation of the demagnetizing field H_a. Note that the total magnetic energy is the sum of the magnetic energy and the anisotropy energy, $E = E_B + E_a$. So,

if the torque τ acting on the magnetic moment is calculated by taking the derivative of the total energy with respect to the angle between the moment and the external field, we obtain $\tau = \partial E/\partial\theta = m\mu_0 H\sin\theta + 2KV\sin\theta\cos\theta$. Based on this expression, we can rewrite the equation of motion as follows

$$m\mu_0 H\sin\theta + 2KV\sin\theta\cos\theta = m\mu_0(H + H_a)\sin\theta., \tag{3.22}$$

which gives

$$\mu_0 H_a = \frac{2KV}{m}\cos\theta. \tag{3.23}$$

In the case of a uniaxial sphere, with an external field applied approximately along the magnetization direction, $i.e\ \cos\theta \approx 1$, Eq. (3.23) reduces to

$$\mu_0 H_a = \frac{2KV}{m}. \tag{3.24}$$

This implies that the angular resonance (precessional) frequency is

$$\omega_r = \gamma\mu_0(H + H_a) \approx \gamma(\mu_0 H + \frac{2K}{M}), \tag{3.25}$$

where $\gamma = ge/2m_e$ is the gyromagetic ratio with $\gamma/2\pi$ = 2.7992$\times 10^{10}$ Hz/T. Here g is the g-factor, H is the external magnetic field, H_a is the demagnetizing field due to the magnetic anisotropy, K is the anisotropy constant (energy per unit volume), $M = m/V \approx M_s$ is the magnetic moment per unit volume or the intensity of 'magnetization', and M_s is the saturation magnetization, which can be measured by using a SQUID magnetometer.

3.4 Ferromagnetic resonance (FMR)

Theoretically, the ferromagnetic resonance [70, 69] will cause dispersion and decrease of magnetic susceptibility in magnetic materials in the RF/Microwave frequency range. When the frequency of the microwave matches the natural frequency of the ferromagnetic resonance, energy absorption occurs and so the magnetic susceptibility (χ)[2] and the corresponding permeability ($\mu = 1 + \chi$) will become very dispersive when observed within a frequency range around the resonance.

3.4.1 Kittel and LLG models

The FMR theory and dispersion of the complex magnetic permeability (μ) was first discussed by L. Landau and E. Lifshitz in 1935 [70]. Later,

[2] $\vec{M} = \chi\vec{H}$, where $\vec{M}$ is the magnetization and $\vec{H}$ is the magnetizing field.

in 1946-1947, the FMR phenomenon was experimentally observed by J. H. E. Griffiths, W. A. Yager and R. M. Bozorth [71]-[72]. In attempting to measure the permeability of iron, cobalt and nickel at microwave frequency, Griffiths accidentally found that ferromagnetic metals exhibited an energy loss peak when a certain magnetic field is applied. He analyzed the relation between the microwave frequency and the magnetic field at the peak position, and found that the ferromagnetic resonance did not occur exactly at the electron spin resonance point, since it was known that the spin resonance emerges when $\hbar\omega = g\mu_B H$ or $\omega = \gamma H$, where $\hbar$ is the Planck constant, ω is the angular frequency, g is the electron g-factor, $\mu_B = e\hbar/2m_e$ is the Bohr magneton, H is the internal magnetizing field, and $\gamma = ge/2m_e$ is the electron gyromagnetic ratio.

One year after this experimental discovery, C. Kittel published a theoretical paper suggesting that the ferromagnetic resonance condition should be modified from the original Landau-Lifshitz theory, by taking into account the shape and crystalline anisotropy through the demagnetizing fields [69]-[73]. He proposed that electron spin FMR occurs according to the resonance condition $\omega_0 = \gamma H_{\text{eff}}$, where H_{eff} is an effective magnetizing field, equal to $(BH)^{\frac{1}{2}}$ for a plane surface, $H + M$ for a long circular cylinder, and H for a sphere. In addition, for the special case of uniaxial crystal with the axis parallel to the external static field, the value of H is increased by $2K/M_s$, where K is the anisotropy constant.

The fundamental assumption in Kittel's FMR theory is the validity of demagnetizing factors. Kittel stated in his original paper [69] that "We must accordingly discuss only objects which are uniformly magnetized at the frequency under consideration. It is therefore necessary that certain dimensions of the specimens are small in comparison to the eddy current skin depth." In cobalt, the skin depths in the frequency range between 1 GHz and 10 GHz are on the order of 100 nm, so only nanoparticles satisfy this requirement.

When the system is in the blocked state, magnetic reversal can still occur, for example by resonance excitation. Any physical system exhibits energy gain when the frequency of an energy source matches the natural frequency of the system. In case of cobalt particles, the exposure to a time-harmonic magnetic field $he^{i\omega t}$, particularly at a frequency close to the precessional frequency of the particles, leads to absorption of the field energy. The absorption may cause magnetization reversal or fluctuation between the magnetic states, see Fig. 3.5a.

Besides the gain, the dynamic process also possesses energy loss. Here, we describe the loss by applying the Landau, Lifshitz [70] and Gilbert [74] theory. The magnetization of a ferromagnetic domain is described by the Landau-Lifshitz-Gilbert (LLG) equation

$$\frac{d\vec{M}}{dt} = \gamma\mu_0\vec{M} \times \vec{H}_{tot} - \alpha\frac{\vec{M}}{M} \times \frac{d\vec{M}}{dt}. \tag{3.26}$$

The first term on the right hand side represents the precession of magnetization. The energy loss is taken into account by the second term via a single damping constant α. $\vec{M}$ is the magnetization of the system, and $\vec{H}_{tot}$ is the total magnetizing field which includes the applied static field ($\vec{H}$), the anisotropic field (H_a), and the relatively smaller alternating RF/microwave signal ($he^{j\omega t}$),

$$\vec{H}_{tot} = \vec{H} + \vec{H}_a + \vec{h}e^{j\omega t}. \tag{3.27}$$

Similarly, the magnetization at a given time includes the magnetization of the particle $\vec{M}_0$ and the time-varying term,

$$\vec{M} = \vec{M}_0 + \vec{m}e^{j\omega t} \approx \vec{M}_s + \vec{m}e^{j\omega t}, \tag{3.28}$$

where $\vec{M}_s$ is the saturation magnetization.

Recall that, within the particle, the magnetic field is $B = \mu_0(h + \chi h) = \mu_0\mu_r h$, where μ_r is the relative magnetic permeability, and $\chi = \frac{\partial M}{\partial h}$ is the magnetic susceptibility. So, an analytical expression for the complex permeability can be derived based on the LLG formalism. Note that, from what follows, the relative permeability will be defined as $\mu_r = \mu_r' - i\mu_r''$, to avoid that presence of a negative sign in front of μ_r'' when discussing the magnetic energy loss of the material being tested.

In the special case when a large external field is applied to a magnetic system, $i.e.$ $|H| \gg |H_a|$, it is possible to assume that $\vec{M}_0 \parallel \vec{H}$. Thus, by assuming that the external field $\vec{H}$ is in the z-direction and assuming that the magnitude of the oscillating field ($e.g.$ microwave) is much smaller than the static field, we can calculate the perpedicular magnetic susceptibility, $\chi_\perp = \partial m_x/\partial h_x = \partial m_y/\partial h_y$. This then gives an analytical expression for the complex permeability of the magnetic particle,

$$\mu_r' = 1 + \frac{\gamma M_s\omega_0[\omega_0^2 - \omega^2(1-\alpha^2)]}{[\omega_0^2 - \omega^2(1+\alpha^2)]^2 + 4\omega^2\omega_0^2\alpha^2}, \tag{3.29}$$

$$\mu_r'' = \frac{\alpha\gamma M_s\omega[\omega_0^2 + \omega^2(1+\alpha^2)]}{[\omega_0^2 - \omega^2(1+\alpha^2)]^2 + 4\omega^2\omega_0^2\alpha^2}, \tag{3.30}$$

where $\omega_0 = \gamma\mu_0(|H| + |H_a|\cos\theta)$. Note that when the external field H is small relative to the anisotropy field H_a, the assumption that $\vec{M}_0 \parallel \vec{H}$

is not valid and the FMR properties and the magnetic permeability of magnetic particles may not be described by Eqs. (3.29) - (3.30).

In general, the complex susceptibility $\chi(\omega) = \chi(\omega)' - j\chi(\omega)''$ and the permeability $\mu(\omega)$ are composed of both parallel, $\chi_{\parallel}$, and perpendicular $\chi_{\perp}$ components. The measured susceptibility is assumed to be an average of all components [75],

$$\chi(\omega) = \frac{1}{3}[\chi_{\parallel}(\omega) + 2\chi_{\perp}(\omega)]. \tag{3.31}$$

The perpendicular component can be described well by the LLG-Kittel theory, $i.e.$ Eqs. (3.29)-(3.30). The parallel component is purely relaxational and usually assumed to be described by Debye's model [76],

$$\chi_{\parallel}(\omega) = \frac{\chi_{\parallel}(0)}{1 + j\omega\tau_{\parallel}}, \tag{3.32}$$

where $\tau_{\parallel} = \tau_0\sigma$ with $\tau_0 = 1/\gamma\mu_0 H_a\alpha_{\parallel}$, $\mu_0 H_a = 2K/M_s$ and $\sigma = KV/k_B T_{\mathrm{room}}$.

Besides the size of the particles, crystal structure also affects the resonance conditions. At macroscopic scales, bulk cobalt has only two forms of lattice structure, namely hexagonal-closed-packed (hcp) and face-centered-cubic (fcc). For nanoparticles, a cubic ϵ-cobalt phase with a structure similar to β-manganese, has been observed in addition to the hcp and fcc phases [77, 78]. New chemical syntheses allow production of ϵ-cobalt particles at specific diameters (with a narrow size distribution) [17, 79]. It is therefore possible to experimentally study ideal spherical magnetic systems and their FMR effects at higher frequencies.

In a composite material, the interaction between the field and the magnetic particles is far more complex than in the case of a single particle. For example, millions of particles inside a tiny volume, each particle acts as a wave scatterer, can cause interference effects and collective phenomena especially when the interaction energy between the particles cannot be neglected. However, in the regime where the wavelength of the oscillating field (e.g. microwave signal), is much larger than the size of the nanoparticles inside a composite sample, the interference effects can be neglected and an effective medium model is commonly applied to determine the intrinsic properties of the composite sample. If the volume fraction of the inclusions is small, the mixing rules such as the Bruggeman equation [80] and Maxwell-Garnett model [81, 82] can be used.

3.4.2 Effective medium models

Effective medium theories (EMT) are mathematical models that describe the properties of a material based on the properties of its components. For a composite with metallic inclusions, one can assume that the microwave wavelength is large compared to the size of the particles. In addition, the distance between inclusions can also be assumed to be small compared to the wavelength of the microwave. Let us first consider a simple model where the space is filled only with low-concentration metallic particles. Each particle is excited by a local field [83],

$$E_{\text{local}} = E_{\text{ext}} + \sum_{j \neq i} E_{ij}, \tag{3.33}$$

where E_{ext} is the external applied field, and E_{ij} is the field at the position of the particle i due to another particle j. The local field E_{local} is different from the averaged field $\hat{E}$,

$$\hat{E} = \hat{E}_{\text{ext}} + \sum_{j \neq i} \hat{E_{ij}} + \hat{E_{ii}}, \tag{3.34}$$

where $\hat{E_{ii}}$ is the average electric field at the position of the particle i due to the charges within the i$^{\text{th}}$ particle. Eq. (3.33) and Eq. (3.34) gives

$$E_{\text{local}} - \hat{E} = E_{\text{ext}} - \hat{E}_{\text{ext}} + \sum_{j \neq i} (E_{ij} - \hat{E_{ij}}) - \hat{E_{ii}}. \tag{3.35}$$

If the souce of the external field is far from the material, one may assume that $E_{\text{ext}} - \hat{E}_{\text{ext}} \approx 0$. Also, in the regime where the microwave wavelength is large compared to the distance between inclusions, the field can be considered within the quasistatic limit. That is E_{ij} can be described by the field of an electric dipole which falls off as r_{ij}^{-3}. As a result, only a few nearest particles will contribute to creating the difference between E_{local} and $\hat{E}$. In the case of low-density randomly distributed inclusions, $i.e.$ $\sum_{j \neq i} (E_{ij} - \hat{E_{ij}}) \approx 0$, Eq. (3.35) reduces to

$$E_{\text{local}} = \hat{E} - \hat{E_{ii}}. \tag{3.36}$$

If a volume V is a collection of particles at position r_m with a charge q_m,

$$E_{ii}(r) = -\nabla \sum_m \frac{q_m}{4\pi\epsilon_0 |r - r_m|}, \tag{3.37}$$

which gives the averaged value

$$\hat{E_{ii}} = -\sum_m E_m, \tag{3.38}$$

where

$$E_m = -\nabla_m \int_V \frac{q_m/V}{4\pi\epsilon_0|r-r_m|}\mathrm{dV} = \frac{1}{3\epsilon_0}\frac{\mathrm{q_m}}{\mathrm{V}}. \tag{3.39}$$

Therefore,

$$\hat{E_{ii}} = -\frac{1}{3\epsilon_0 V}\sum_m q_m r_m = -\frac{1}{3\epsilon_0 V}p = -\frac{P}{3\epsilon_0}. \tag{3.40}$$

where $P = p/V$ is the average polarization, and $p = \sum_m q_m r_m$. From Eq. (3.36) and Eq. (3.40), we obtain the Lorenz-Lorentz relation between the local and the averaged field

$$E_{\mathrm{local}} = \hat{E} + \frac{P}{3\epsilon_0}. \tag{3.41}$$

The induced dipole moment p of a particle can be expressed in terms of the local field, $p = \alpha E_{\mathrm{local}}$, where α is the polarizability. Therefore,

$$P = \frac{p}{V} = \frac{\alpha E_{\mathrm{local}}}{V}. \tag{3.42}$$

From Eq. (3.41) and (3.42), we obtain

$$P = \frac{\alpha/V}{1-\frac{\alpha}{3\epsilon_0 V}}\hat{E}. \tag{3.43}$$

Substituting this in $D = \epsilon_0\hat{E} + P$ gives

$$\epsilon_{\mathrm{eff}} = \epsilon_0 + \frac{\alpha/V}{1-\frac{\alpha}{3\epsilon_0 V}}, \tag{3.44}$$

that is

$$\frac{\epsilon_{\mathrm{eff}}-\epsilon_0}{\epsilon_{\mathrm{eff}}+2\epsilon_0} = \frac{\alpha}{3\epsilon_0 V}. \tag{3.45}$$

Equation (3.45) is the so-called Clausius-Mossotti formula. For a spherical inclusion with dielectric constant ϵ_p and a volume V_p, the polarizability α is given by $\alpha = 3\epsilon_0 V_p(\epsilon_{\mathrm{p}}-\epsilon_0)/(\epsilon_{\mathrm{p}}+2\epsilon_0)$, so we obtain

$$\frac{\epsilon_{\mathrm{eff}}-\epsilon_0}{\epsilon_{\mathrm{eff}}+2\epsilon_0} = f\frac{\epsilon_p-\epsilon_0}{\epsilon_p+2\epsilon_0}, \tag{3.46}$$

where $f = V_p/V$ is the volume fraction of the particle inclusions. The complete version of the Maxwell-Garnett equation for a composite composed of a dielectric matrix and randomly-embedded spherical inclusions can be derived in a similar way. The derivation gives

$$\frac{\epsilon_{\mathrm{eff}}-\epsilon_{\mathrm{m}}}{\epsilon_{\mathrm{eff}}+2\epsilon_{\mathrm{m}}} = f\frac{\epsilon_{\mathrm{p}}-\epsilon_{\mathrm{m}}}{\epsilon_{\mathrm{p}}+2\epsilon_{\mathrm{m}}}, \tag{3.47}$$

where ϵ_{m} is the permittivity of the matrix. Equation (3.47) should be valid at low-volume fraction.

Both Maxwell-Garnett and Bruggeman rules can be derived from a more general mixing rule [84],

$$\frac{\epsilon_{\mathrm{eff}}-\epsilon_{\mathrm{m}}}{\epsilon_{\mathrm{eff}}+2\epsilon_{\mathrm{m}}+\nu(\epsilon_{\mathrm{eff}}-\epsilon_{\mathrm{m}})} = f\frac{\epsilon_{\mathrm{p}}-\epsilon_{\mathrm{m}}}{\epsilon_{\mathrm{p}}+2\epsilon_{\mathrm{m}}+\nu(\epsilon_{\mathrm{eff}}-\epsilon_{\mathrm{m}})}. \tag{3.48}$$

If the dimensionless parameter $\nu = 0$, the formula reduces to the Maxwell-Garnett model; if $\nu = 2$, the formula reduces to Bruggeman formula [85, 84]. Setting $\nu = 0$ and solving Eq. (3.48) for ϵ_{eff}, we obtain

$$\epsilon_{\text{eff}} = \epsilon_{\text{m}} + 3f\epsilon_{\text{m}} \frac{\epsilon_{\text{p}} - \epsilon_{\text{m}}}{\epsilon_{\text{p}} + 2\epsilon_{\text{m}} - f(\epsilon_{\text{p}} - \epsilon_0)} \tag{3.49}$$

In the case of spherical magnetic-particle inclusions, the Bruggeman model gives [86]

$$\mu_{\text{eff}} = \frac{1}{4}\left[(3f-1)\mu_{\text{p}} + (2-3f)\mu_{\text{M}} \pm \sqrt{8\mu_{\text{p}}\mu_{\text{M}} + ((3f-1)\mu_{\text{p}} + (2-3f)\mu_{\text{M}})^2}\right], \tag{3.50}$$

where f is the particle volume fraction, μ_{eff} is the permeability of the composite, μ_{p} is the permeability of the magnetic particle, and μ_{M} is the permeability of the insulating material. Equation (3.50) follows directly from the general mixing rule formula, Eq. (3.48), for the permittivity with $\nu = 2$. Note that, in general, Eq. (3.48) may not be directly applied to the magnetic permeability. In Ref. [87], the derivation of the Maxwell-Garnett formula for the magnetic permeability gives,

$$\mu_{\text{eff}} = \mu_{\text{M}} + 3f\mu_{\text{M}} \frac{\mu_{\text{p}} - \mu_{\text{M}}}{-2\mu_{\text{p}} + 5\mu_{\text{M}} + 2f(\mu_{\text{p}} - \mu_{\text{M}})}. \tag{3.51}$$

Nowadays, magnetic materials are designed to operate up to frequencies as high as 5 to 12 GHz, due to the development of computer and telecommunication capabilities. At these frequencies, most of conventional materials, such as ferrites, exhibit relatively low magnetic permeabilities, $i.e.$ $\mu_r \approx 1$. Recent studies show that composite materials with ferromagnetic nanoparticle inclusions may be used to replace conventional materials for high-frequency applications [88, 89]. The applications of nanomaterials are diverse. Some industrial applications involve magnetic materials with high permeabilities (for sensor or antenna applications); some requires large absorption in a narrow-bandwidth (for filters or absorbers). In case of antenna applications, the search for high-permeability materials with minimal losses has led to the idea of eliminating eddy-current effects by utilizing composite materials made of smaller magnetic fillers. Conventionally, these fillers (magnetic powders) are prepared by mechanical methods, and the resulting particles are usually at the micro- and nanoscale. But reducing the size also increases the volume fraction of the oxide layer, and also it is almost impossible to control the size distribution of nanoparticles by mechanical means. Recent developments in material research have been focusing extensively toward finding new chemical methods to synthesize magnetic particles at the nanoscale with

a narrow size distribution. The problem of oxidation can be solved, for example, by covering the particles with graphene shells [90, 91].

In contrast to the advanced development of technology, the microwave response of ferromagnetic nanoparticles is still far from being well understood. In the special case when the nanoparticles can be described by a uniaxial model (as presented in Fig. 3.5), the Kittel FMR theory and LLG equation can be combined with an effective medium model to describe how a single ferromagnetic nanoparticle would respond under a microwave irradiation. It is the aim of this chapter to test whether these simplified models are sufficient to describe composite materials made of ferromagnetic nanoparticles.

Based on the uniaxial magnetic particle model, Eq. (3.25) implies that the microwave dispersion and the reduction of magnetic permeability are governed by the anisotropy energy (K) of the particle. For a single particle system, the crystalline or shape anisotropy energy defines the height of the energy barrier (see Fig. 3.5). Increasing the energy barrier between the two magnetic states can change the transition probability of the system and also, as a result, the response of the system to the external world.

In most circumstances, the development of a new technology usually requires an extensive amount of experimental investigations of materials at the frequencies that the materials are expected to be used. In the design of microwave devices, an engineer needs to know with high precision the values of the complex magnetic permeability μ and the electric permittivity ϵ. (Sometimes, the refractive index $n = \sqrt{\epsilon\mu}$ and the wave impedance $z = \sqrt{\frac{\mu}{\epsilon}}$ are used instead of μ and ϵ.)

In basic science research, the measurement of magnetic permeability provides useful information for the study of magnetic resonant phenomena. For example, based on permeability measurements, Fe_2O_3 nanoparticles were found to exhibit a magnetic resonance around 1.5 GHz [88], while the iron nanocrystal (28 nm) of Fe_3O_4 was reported to have energy-loss resonance at 2 GHz [9]. Similar magnetic resonant response was also observed in nickel particles around 5.5 GHz [92].

3.5 Cobalt nanoparticles

This section presents an experimental study of the effect of microwave radiation on cobalt nanoparticles. The study was done by measuring the index of refraction, the electric permittivity, and the magnetic permeabil-

ity of composite materials made from various kinds of cobalt nanoparticle fillers. The applications of cobalt nanocomposites include microwave absorbing layers, antenna, inductors, and filters.

In ferromagnetic materials, the strongly-coupled electrons have a tendency to align their magnetic moments in the same direction within a small region called domain. For an ϵ-cobalt nanoparticle, the particle usually consists of a single crystal core. The spin-orbit interaction inside the crystal structure causes the electron moment to align along certain 'easy' directions. A magnetic particle with a single easy axis is called a 'uniaxial' particle.

3.5.1 Face-centered-cubic (fcc) cobalt nanoparticles

Experimental studies on fcc-cobalt nanoparticles (average diameter 40 nm) shows that composites made from these particles exhibit a broad magnetic absorption peak around 7 GHz [93, 94, 95]. This subsection discusses the observation of fcc-cobalt nanoparticles under microwave radiation within the frequency range between 2 and 18 GHz, in zero magnetizing field, at room temperature. The samples were prepared by mixing the nanoparticles with insulating materials. Due to the fabrication process, ferromagnetic nanoparticles inside the composites are usually randomly oriented. The fcc-cobalt nanoparticles were systhesized by first dissolving polystyrene in toluene and making a nanoparticle colloid with toluene using an ultrasonic homogenizer. Then the two solutions were mixed and left to evaporate at 80^oC. Table 3.1 shows the characteristics of nanocomposites analyzed by transmission electron microscope (TEM), SQUID magnetometer and powder X-ray diffractometer (XRD).

	TEM	SQUID	XRD
	d [nm]	M_s [emu/g]	Crystal, d [nm]
Cobalt	50-150	144	Co(FCC), 66 ± 20
Iron	20-30	127	Fe (BCC), 9 ± 1
			FeO, 3 ± 1

Table 3.1. The diameters and crystal structures of cobalt nanoparticles measured by TEM, SQUID and XRD, compared with the properties of iron nanoparticles presented in Publication VII.

Figure 3.6 shows the TEM images of cobalt particles. The average size

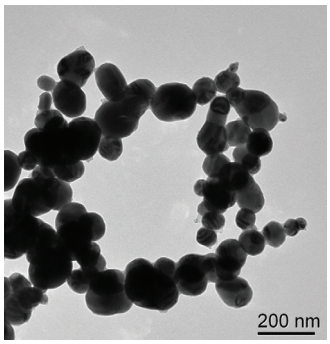

Figure 3.6. A TEM image of fcc-cobalt particles.

of the particles is 50-150 nm, which agrees well with the XRD analysis (60 nm). The XRD results shows that the cobalt has the fcc structure. The saturation magnetization M_s of the magnetic particles was measured by a SQUID magnetometer and found to be 144 emu/g.

The effects of the interaction between microwave radiation and fcc-cobalt nanoparticles were studied by measuring the permeability spectra of nanocomposite materials (made by randomly embedding the particles in an insulating matrix as discussed before). The measurements were done by a transmission/reflection technique using the reference-plane invariant algorithm [67], presented in Publication I. Prior to the measurements, the composite materials were pressed in a pellet mold, so that the samples can be inserted inside a 7-mm coaxial air-line, used as a sample holder to conduct the microwave signals. The group delay and S-parameters (transmission/reflection) were measured by using a Rohde and Schwarz ZVA40 vector network analyzer. The measurements of transverse electromagnetic waves were done after a SOLT calibration was performed.

Figures 3.7-3.9 present the microwave response of the fcc-cobalt nanocomposites. The imaginary spectra of refractive index (n'') in Fig. 3.7 show the total energy loss of the material. Microwave energy loss absorption peaks around 12 to 14 GHz. This peak has a magnetic origin because the imaginary spectra of magnetic permeability (μ'') also exhibit peaks in this frequency range. Comparing to the composites of bcc-Fe/FeO nanoparticles (Publication VII) with the same volume fraction , these fcc-Co nanocomposites exhibit microwave resonances at higher resonant frequencies and magnetic loss, $i.e.$ μ''. The dielectric loss is relatively low in both fcc-Co and bcc-Fe/FeO composites. The imaginary permittivity ϵ'' is nearly zero for all the fcc-Co samples, see Fig. 3.9.

The measured microwave spectra presented here exhibit also some sys-

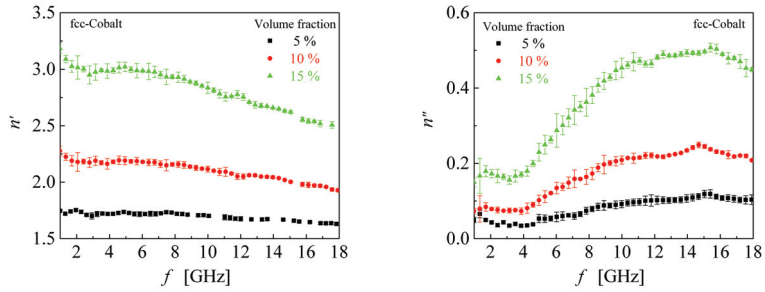

Figure 3.7. The complex refractive index of fcc-cobalt nanocomposites at different volume fractions. (Unpublished data)

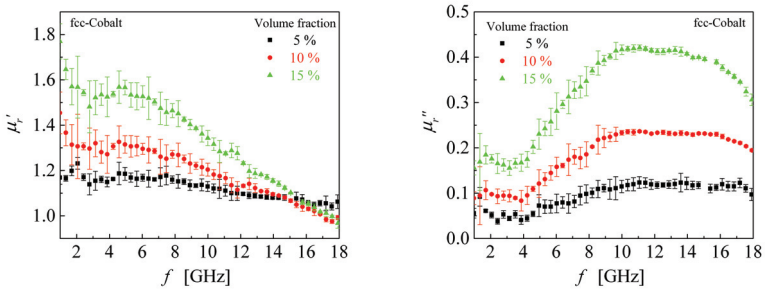

Figure 3.8. The relative permeability μ_r of fcc-cobalt nanocomposites at different volume fractions. (Unpublished data)

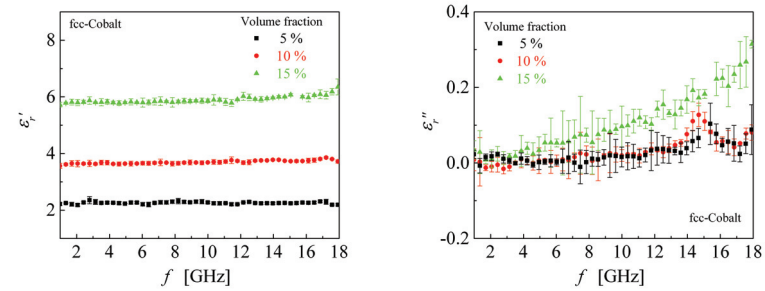

Figure 3.9. The relative permittivity ϵ_r of fcc-cobalt nanocomposites at different volume fractions. (Unpublished data)

tematic errors, as shown by the error bars in each graph. Some errors are known to be intrinsic for all transmission/reflection measurements, some are caused by small reflections and the associated phase errors at adapters. Further discussion on measurement techniques and errors can be found in Publications I and V.

The magnetic permeability and electric permeability spectra in Fig. 3.8 and Fig. 3.9 suggest that the fcc-cobalt nanoparticles exhibit a strong electric response (large ϵ_r') but a weak magnetic response (small μ_r') at this frequency range (2-18 GHz). However, compared with Fe/FeO nanoparticle composites [89], fcc-cobalt composites exhibit a larger magnetic loss. This actually agrees well with the analysis done by SQUID magnetometry: the fcc-cobalt nanoparticles have a saturation magnetization of 144 emu/g while the Fe/FeO particles have 127 emu/g.

Compared with the Fe_2O_3, Fe_3O_4 and carbon-coated nickel composites reported in [88], [92] and [9], the fcc-cobalt composites have relatively higher magnetic permeabilities in the frequency range between 2 to 6 GHz, even at lower particle concentration. This characteristic occurs in conjunction with a magnetic loss that peaks at higher frequencies between 10 and 12 GHz. This frequency is higher than the frequency at the magnetic loss peak of fcc-cobalt nanoparticles reported earlier [93].

However, recent research on fcc-Co particles has suggested that a peak of magnetic loss observed in a frequency domain around 7 GHz may not be associated with a ferromagnetic resonant phenomenon [93]. This speculation was based on a few assumptions. First, the permeability spectra of composite materials made from fcc-Co particles were assumed to follow Kittel's ferromagnetic resonance theory for a spherical particle. Second, the authors of Ref. [93] assumed that hcp-cobalt particles exhibit the ferromagnetic resonance at 6.5 GHz by referring to a study of Co_x/Ni_y particles [95]. Based on these two assumptions, an fcc-cobalt nanoparticle, that has a lower magnetocrystalline anisotropy compared to the hcp-cobalt, was expected to exhibit a ferromagnetic resonance at a frequency much lower than 6.5 GHz. In order to understand the origin of the peak in magnetic loss at 7 GHz, the authors calculated the eddy current loss of a magnetic particle. The eddy current loss can be expressed by

$$\frac{\mu''}{\mu'} \propto \frac{\mu_r'' f D}{\rho}, \tag{3.52}$$

where f is the microwave frequency, D is the particle diameter, and ρ is the electric resistivity of the particle. Eq. (3.52) implies that we can distinguish the eddy current loss from other losses by observing if the quantity

$\mu''/(\mu'^2 f)$ is constant when plotted in the frequency domain. They concluded that the magnetic loss over 1 and 18 GHz is mainly caused by the eddy current effect, but below 1 GHz the eddy current is not the dominant magnetic loss mechanism [93].

To compare the results of this study with Refs. [93] and [92], the parameter $\mu_r''/(\mu_r'^2 f)$ of each sample was plotted here in Fig. 3.10. The values of $\mu_r''/(\mu_r'^2 f)$ change abruptly at frequencies below 4 GHz. But, between 4 and 18 GHz, the changes are relatively weak. So, if the same reasoning as stated above can be used, the magnetic loss absorption as seen in Fig. 3.8 may be governed also by the eddy current phenomena. In addition to the eddy current loss, the magnetic ordering and the corresponding excitation, such as spin-waves, could also result in energy-relaxation processes in magnetic materials.

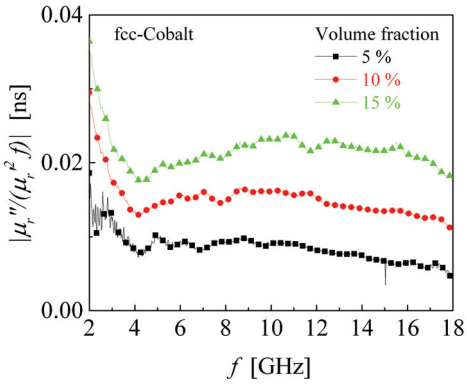

Figure 3.10. The values of $\mu_r''/(\mu_r'^2 f)$ for fcc-Co composites at different volume fractions. (Unpublished data)

So far, there is no evidence that magnetic losses at GHz frequencies are really caused by eddy currents. There is also no real evidence that the magnetic absorption peak would be associated with the natural ferromagnetic resonance. Note also that the theoretical analysis given by the authors of Ref [94], which is used as well for illustration in Fig. 3.10 , is based on certain assumptions that need to be justified more rigorously.

Based on Kittel's theory, natural ferromagnetic resonance is associated with the linear relation between the effective magnetizing field and the resonant frequency. Thus, in principle, the FMR theory can be tested, for example by measuring the permeability and observing FMR in varying magnetizing field. However, the broad size distribution and the plausible formation of a polycrystalline core demonstrated that fcc-cobalt nanopar-

ticles may not be a good material for studying the physics of ferromagnetic resonance.

3.5.2 ϵ-Cobalt nanoparticles

In this subsection, a more systematic study on spherical ϵ-cobalt particles is presented. Compared with fcc-cobalt, ϵ-cobalt nanoparticles are more suitable for FMR studies, since an ϵ-cobalt nanoparticle is more frequently found in the form of a single crystal. In this work, the ϵ-cobalt nanoparticles were synthesized by chemical methods described in Refs. [17, 18]. The sizes of the particles are between 3 and 30 nm. Some sets contain monodispersed spherical particles. The microwave characterization was done by measuring the permeability and other intrinsic parameters in varying magnetizing fields at room temperature over a broad range of frequency. The main results of the study are presented in Publications V and VI.

Samples are made of a mixture of polystyrene (PS) and randomly-oriented ϵ-cobalt nanoparticles. The experiments are done by measuring the complex magnetic permeability of the composite material in a frequency range between 0.5 and 12 GHz at zero and high magnetic field. The blocking temperature and the saturation magnetization measured by a SQUID magnetometer determines the anisotropy energy, thus allowing the prediction of ferromagnetic resonant frequencies according to the Kittel's theory for uniaxial spherical particles. The results show that the resonance condition of the cobalt nanocrystals can be estimated by combining Kittel's FMR formula with the Landau-Lifshitz-Gilbert equation and the effective medium model.

The effects of magnetic fields, particle morphology, and magnetic anisotropy were also investigated and analyzed. In summary, composite materials made from ϵ-cobalt nanoparticles and polystyrene were observed under microwave radiation. Experimental results demonstrated that the randomly-oriented spherical nanoparticles inside a composite induce the ferromagnetic resonant absorption at microwave frequencies (1 to 12 GHz). The permeability spectra can be predicted partly at a high-magnetizing field by using the phenomenological model (LLG/Kittel equation) and the effective medium model (Bruggeman or Maxwell-Garnett) presented above in section 3.4.2. We find that at a zero-magnetizing field, the LLG/Kittel equation and the effective medium model predicts magnetic resonance at relatively lower frequencies compared to the experimentally observed val-

ues. In case of polydispersed ϵ-cobalt particles with size of about 10 nm, the magnetic response began to follow Kittel's model for non-interacting particles when the magnetizing field is larger than 3 kOe. Based on experimental data, we also found that any cobalt composite that consists of ϵ-cobalt nanoparticles within the size range between 8 and 35 nm, either monodispersed or polydispersed, exhibit resonant absorption which peaks in the frequency range between 2 and 6 GHz. Particles of smaller sizes, especially the ones below 5 nm, do not have significant response to the microwave field in this frequency range.

Our experimental results (see Publication VI) also showed that, at high magnetizing field, some parts of the spectra can be described by Landau-Lifshitz-Gilbert equation and Maxwell-Garnett effective medium model. In the low field regime, the resonant absorption occurred at frequencies higher than the resonant frequencies of non-interacting-particle picture. Transmission electron microscopic images showed that the samples used in the microwave measurement contain both isolated particles and aggregated particles (clusters and chains). In case of monodispersed particles, the formation of superlattices (closed-pack array of particles) was also found.

In terms of technological applications, both monodispersed and polydispersed particles show wide-band absorbing spectra that can be controlled by an external magnetic field. Experimental results prove that the particles at the sizes of about 27 to 35 nm usually appear as facet (non-spherical) particles; they are better choices for high-μ low-loss applications at least for 1 GHz applications. Medium-size monodispersed spherical particles (10-20 nm) are good as microwave absorbers, particularly if superlattices are formed. Measurement results show that these superlattices may increase the absorption capability of the material. So less particles may be required to engineer a standard absorber/filter, if the superlattices are utilized. In the near future, if technology allows the control of particle arrangement inside a fluid-like absorbing matrix, the monodispersed ϵ-cobalt particles could be engineered in tunable microwave circuit and RF components without the use of magnetic field.

According to Kittel's theory [69], the zero-field ferromagnetic resonance of a uniaxial spherical particle is associated with the anisotropy field $\mu_0 H_a = 2K/M_s$, see Eqs. (3.21), (3.22), and (3.25). To determine the anisotropy constant K, we measure the ferromagnetic-superparamagnetic blocking temperature T_B from the zero-field cooled (ZFC) and field-cooled

(FC) magnetization curve. Here, we determine both K and the saturation magnetizaton M_s by using a superconducting quantum interference device (SQUID) Quantum Design MPMS XL7 magnetometer. The measurements were done for small sections from the actual sample. Each section has a volume of approximately 1 mm^3. The weights of all the samples were measured and used in conjunction with the measured saturation magnetization to calculate the magnetization per unit mass. Note that due to the anisotropic arrangement of particles and clusters, different sections taken from the same sample may have different M_s.

Polydispersed ϵ-cobalt nanoparticles

Polydispersed particles synthesized by the method described in [17] were characterized by a transmission electron microscope (TEM). The TEM images (see Fig. 3.11) show that polydispersed particles at the sizes between 2 to 20 nm tend to aggregate and form clusters in the solution. The average size of one sample is 8 ± 3 nm, while the average size of the other is 16 ± 5 nm (smaller particles at sizes below 10 nm are also observed). Both samples represent single-crystal ϵ-cobalt nanoparticles.

The microwave characterization of these cobalt nanoparticles was done by measuring the relative magnetic permeability ($\mu_r = \mu_r' - i\mu_r''$) , relative electric permittivity ($\epsilon_r = \epsilon' - i\epsilon''$), and refractive index ($n = n' - in''$) of composite materials made from the mixture of the polydispersed ϵ-cobalt particles and polystyrene (PS).

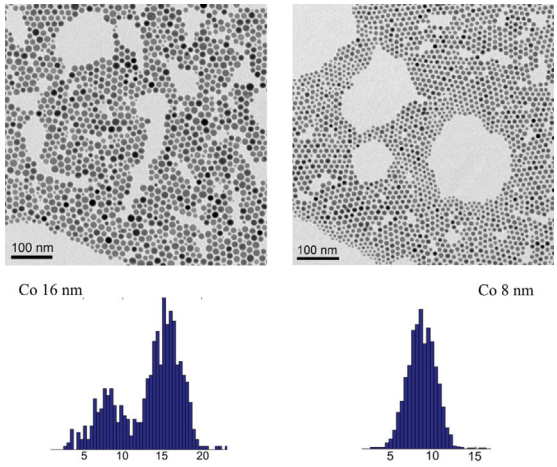

Figure 3.11. The transmission electron microscope image of two sets of polydispersed ϵ-cobalt nanoparticles. One set contains particles with an average diameter of 16 nm; smaller particles (5-10 nm) are also observed. The other set contains particles with an average diameter of 8 nm. (see also Publication VI)

The microwave properties of the composite samples measured by a transmission/reflection method (Publication I) show that the microwave dispersion is caused by magnetic resonance because the dielectric response (real electric permittivity ϵ') is almost constant over the measurement frequency range, see Fig. 3.12. The imaginary part of permittivity ϵ'' is nearly zero, so microwave absorption is of magnetic origin. Although the average sizes of the particles are not the same, the resonant absorption is maximum at almost at the same frequency. In the following, we shall study how these two composites respond to microwave excitation under an external magnetizing field.

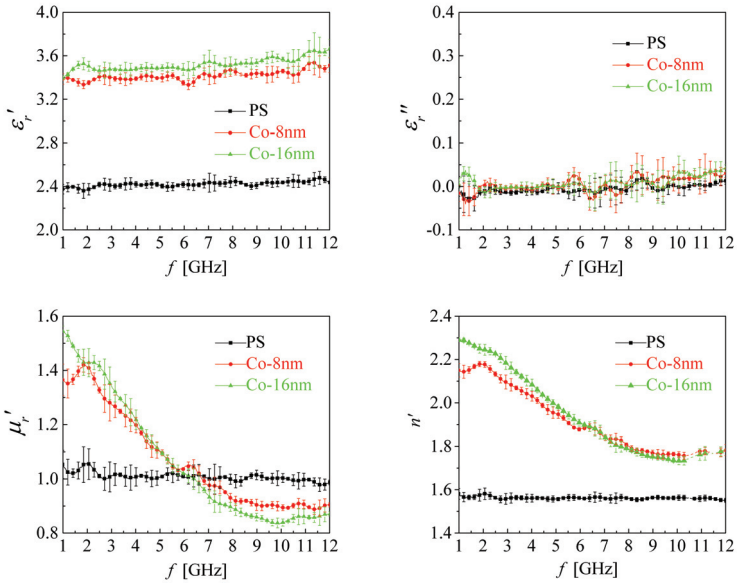

Figure 3.12. The microwave spectra of composites made from the mixture between polystyrene (PS) and polydispersed ϵ-cobalt particles, at a volume fraction of 10%. The microwave spectra of polystyrene (PS) are also presented.

The effect of the magnetizing field

In order to compare the FMR theory with experiments, we conduct the microscopic investigation and the observation of FMR phenomena under a varying magnetizing field. The complex magnetic permeability ($\mu_r = \mu_r' - i\mu_r''$) of the polydispersed ϵ-cobalt nanoparticles was measured over a wide range of frequency in non-zero external static fields H. We found that the material exhibited a broad resonance peak around 4 GHz in a zero external field, see Figs. 3.13 and 3.14.

An external magnetic field causes the resonance to shift towards higher frequency, a reduction of magnetic loss peak was also observed. Surpris-

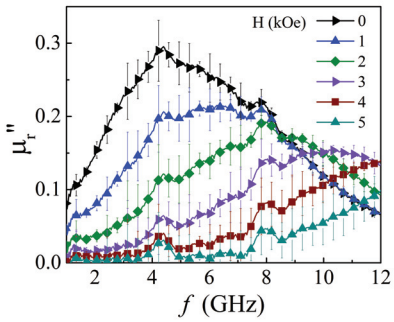

Figure 3.13. The magnetic permeability of a composite of polystyrene (PS) and the 8-nm ϵ-cobalt particles at a volume fraction of 10%.

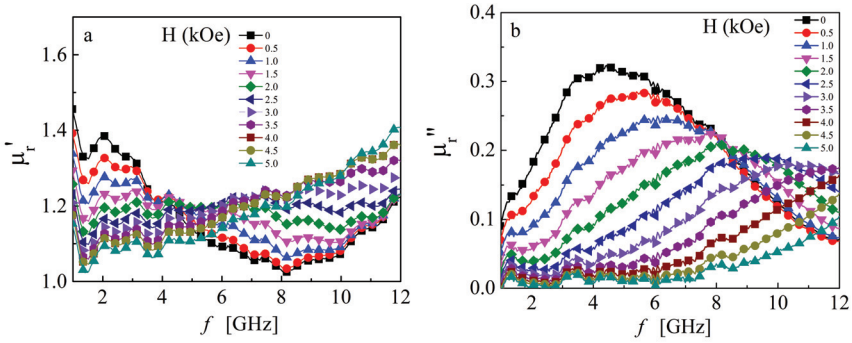

Figure 3.14. The magnetic permeability of a composite of polystyrene (PS) and the 16-nm ϵ-cobalt particles at a volume fraction of 10%. (The μ'' spectra is from Publication VI)

ingly, in the small field regime (below 1.5 kOe), the magnetic absorption remains almost constant at frequencies above 8 GHz. Figure 3.15 presents the comparison between the theoretical models and experimental results. The theoretical spectra (μ_r'') were calculated by combining the phenomenological models: LLG-Kittel and Debye/LLG-Kittel with the Bruggeman effective medium model. T_B and M_s can also be measured by a SQUID magnetometer. For this simulation, we have used T_B and M_s as fitting parameters, with values bounded by the average values obtained from the SQUID measurements.

The calculation was done by setting the particle volume ratio of 0.1, and the average particle diameter d of 16 nm. The magnetizing field is set equal to the experimental values: 2.5, 3.0, ..., 5.0 kOe. The dotted lines show the prediction of the LLG-Kittel model, Eqs. (3.25), (3.30) and (3.50), with the parameters: $M_s = 64$ emu/g, $T_B = 400$ K, and $\alpha = 0.37$. The solid and dashed lines show the prediction of the Debye/LLG-Kittel model, Eqs.

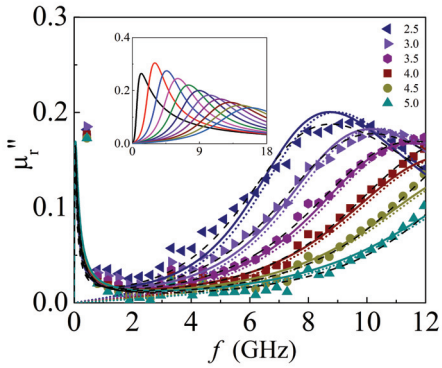

Figure 3.15. The theoretical predictions: LLG-Kittel (dotted lines) and Debye/LLG-Kittel (solid and dashed lines), shown in comparison with the experimental data (discrete symbols). Inset shows the theoretical prediction of LLG/Kittel for all the field values. (The figures are from Publication VI)

(3.25), (3.30), (3.32) and (3.50). The Debye model (parallel susceptibility) was calculated by setting $\alpha_{\text{Debye}} = 0.0005$ and $\chi_{\parallel}(0) = 10000$. The solid lines represent the theoretical prediction with $M_s = 74$ emu/g, and $\alpha = 0.37$, while the dashed lines represent the case when $M_s = 84$ emu/g and α is varied with the magnetizing field: 0.44 ($H = 2.5$ kOe), 0.40, 0.36, 0.32, and 0.28 ($H = 5$ kOe).

The analysis presented in Fig. 3.15 suggests that both the LLG-Kittel and the Debye/LLG-Kittel models can approximately predict the FMR spectra in the regime where the magnetizing field is larger than the anisotropy field. The LLG-Kittel (dotted lines) predicts that the imaginary part of magnetic permeability μ'' should go to zero at very low frequencies. In reality, the permeability μ'' does not keep decreasing at low frequencies, but extensively increases again when we reduce the microwave frequency below 2 GHz. This large absorption at the low-frequency range may be governed mainly by the (non-resonance) relaxation, that can be roughly estimated by the Debye/LLG-Kittel model. Here, the solid and dashed lines present the Debye/LLG-Kittel model in two different cases: constant (solid lines) and varying (dashed lines) damping constant α. The data fitting in Fig. 3.15 shows that the variation of α allows a better fitting, particularly in the high field regime. This finding supports a hypothesis that the damping constant depends on the magnitude of the magnetizing field; the larger the field is, the smaller the damping constant will be.

Figure 3.16 shows a cartoon revealing the difference between the observed ferromagnetic resonance of the ϵ-cobalt composite and the theo-

retical prediction with parameters given in Table 3.17. Based on Kittel's FMR theory, the resonance frequency f_r depends linearly on the effective field $H_{\text{eff}} = H_{\text{a}} + H$, H is the external magnetizing field. But our experiment shows that the linear dependence between f_r and H occurs only in the high field (III) regime. In the low field (I) regime, the resonance generally occurs at higher frequencies compared with the frequencies predicted by the single (non-interacting) particle theory.

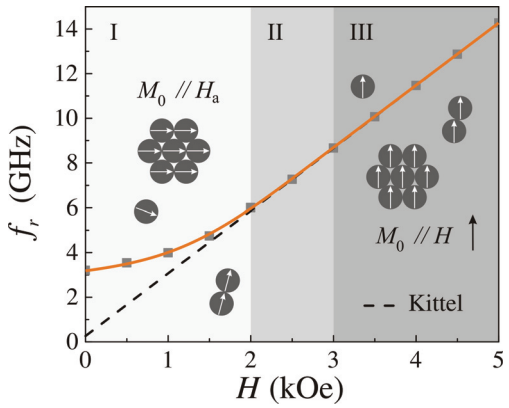

Figure 3.16. A diagram, with experimental data represented as squares, showing the relation between the resonance frequencies (ω_0) and the applied magnetizing field (H). In the low field regime (I), the magnetization of the particles is random and aligns along the anisotropy field. In the case that chains or clusters form inside the composite, the self-generating local magnetic field tends to cause the increase of FMR resonance frequencies. In the high field regime (III), where the magnetization of each particle is directed along the external magnetizing field, Kittel's FMR theory can be applied to predict the resonance absorption spectra. (The figure is from Publication VI)

H (kOe)	H' (T)	α	Volume fraction
0	0.105	0.37	0.112
0.5	0.117	0.38	0.106
1.0	0.133	0.39	0.100
1.5	0.160	0.42	0.100
2.0	0.205	0.40	0.100
2.5	0.250	0.37	0.100
3.0	0.300	0.37	0.100
3.5	0.350	0.37	0.100
4.0	0.400	0.37	0.100
4.5	0.450	0.37	0.100
5.0	0.500	0.37	0.100

Figure 3.17. The Kittel-LLG theory and Bruggemann effective medium model can roughly describe the experimental data shown in Fig. 3.14b using the parameters in this table with the resonance condition $f_r = \gamma(H_{\text{eff}} + H')$, where $H_{\text{eff}} = 2K/M_s$. The fitting was done by using $H' = H$ when H is above 2.5 kOe. At lower magnetizing field, H' is larger than H, implying that the observation does not agree well with the non-interacting particle FMR mode. Other parameters are set as follows: $M_s = 64$ emu/g, $T_B = 400$ K, and $d = 16$ nm.

Observing the cobalt composite with a transmission electron microscope (TEM), we found that ϵ-cobalt nanoparticles were not well separated, see Fig. 3.11. Large amount of clusters were formed. In each cluster, the magnetic dipole interactions between particles generates a distribution of local magnetic field. This local field is not explicitly written in Eq. (3.30). So, it is not surprising to see that the theory does not agree well with the experiment in the small field (I) regime.

In Fig. 3.15, we demonstrated that the LLG-Kittel theory and the effective medium model can be used to predict the high-field regime of the permeability spectra. The data fitting was done in frequency domain. Next, we present the analysis by plotting the permeability data in the magnetizing field domain. Only four sets of data that show nearly-symmetric curves are plotted here in Fig. 3.18 to show the FMR peaks. The figure shows that the 9.58-GHz curve which peaks around 2.25 kOe is less symmetric (non-lorentzian) compared to the spectra at 10.55, 11.56 and 12.53 GHz, that have resonant peaks at higher magnetizing fields. The asymmetry comes directly from the non-LLG/Kittel spectra in the frequency domain at fields smaller than 1.5 kOe as already discussed (see Fig. 3.15).

Although the field-dependence of absorption shown in Fig. 3.18 is not symmetric, $i.e.$ cannot be associated perfectly with the single-particle (LLG-Kittel) model, they are sufficient to provide a proof of the linear relation at resonances between the microwave frequency and the magnetizing field (see the inset graph of Fig. 3.18). Both the main graph and the inset in Fig. 3.18 present the spectra of the composite sample, but the diagram in Fig. 3.16 shows the spectra of cobalt particles. Within the validity of effective medium model, composites exhibit resonant peaks at higher frequencies compared to the constituent particles.

The relation between f and H also shows that the resonance frequency does not reduce to zero at zero magnetizing field. This finding suggests the validity of Kittel's formula for uniaxial spherical particles with an anisotropy field, $i.e.$ $\omega = \gamma(H + H_a) = \gamma(H + 2K/M_s)$. Ideally, if the resonance can be predicted by the Kittel's and LLG's equations, the slope of the $f_r - H$ graph for a cobalt particle should be equal to $\gamma/\sqrt{(1+\alpha^2)}$, that is approximately $2.8025/\sqrt{(1+0.37^2)} = 2.6283$ GHz/kOe. But the graph shows an average slope of 1.97 GHz/kOe, which is 23 $\%$ smaller than the theoretical value, suggesting that the permeability of the cobalt composite cannot be well described by the single-particle (non-interacting) FMR theory. This may be caused by the random orientation of the anisotropy

field, particle-size distribution, or particle-particle interaction. We shall investigate the effect of particle size in the next subsection.

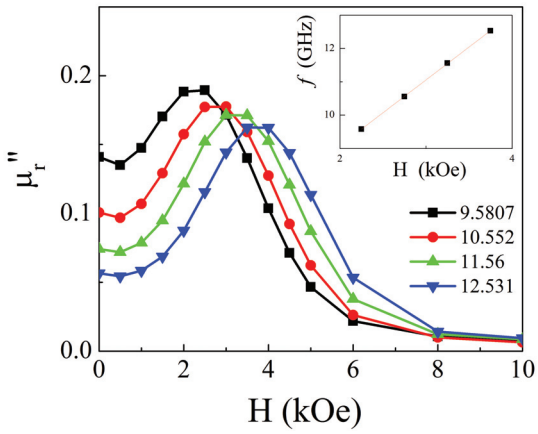

Figure 3.18. The imaginary part of magnetic permeability as a function of the applied magnetic field H. Each color represents the peak at one microwave frequency in the external field domain. The measurement shows that the resonance shifts towards a higher magnetic field when the microwave frequency is increased. The inset picture shows the linear dependence between the resonance frequency f_r of the composite and the external magnetic field H. (The figure is from Publication VI)

The effect of particle morphology

Next, the effect of particle size/shape on the microwave absorption properties is discussed. Composites are made from ϵ-cobalt nanoparticles. These particles were synthesized in the year 2010. The TEM images of the particles within these composites are shown in Figs. 3.19 and 3.20. The composites were fabricated by dissolving amounts of polystyrene in the solvent containing nanoparticles. The evaporation of the solvent then yields solid composite materials. The composite materials were then molded at elevated temperature (150 ^{o}C) to make circular pellets for microwave measurements. Each pellet has the outer diameter of 6.96 mm and the thickness of 4.00 mm. To create a center hole with the diameter of 3 mm, each pellet is drilled mechanically.

The permeability spectra of 2010-composites, see Fig. 3.21, show that the smallest nanoparticles of sample-A (5 nm) exhibit nearly vanishing magnetic response in this frequency range, while the nanoparticles of sample-B, that have relatively larger particle diameters, exhibit a weak magnetic loss absorption peak around 4 GHz. Sample-C is a representation of monodispersed particles. Comparing nearly-monodispersed parti-

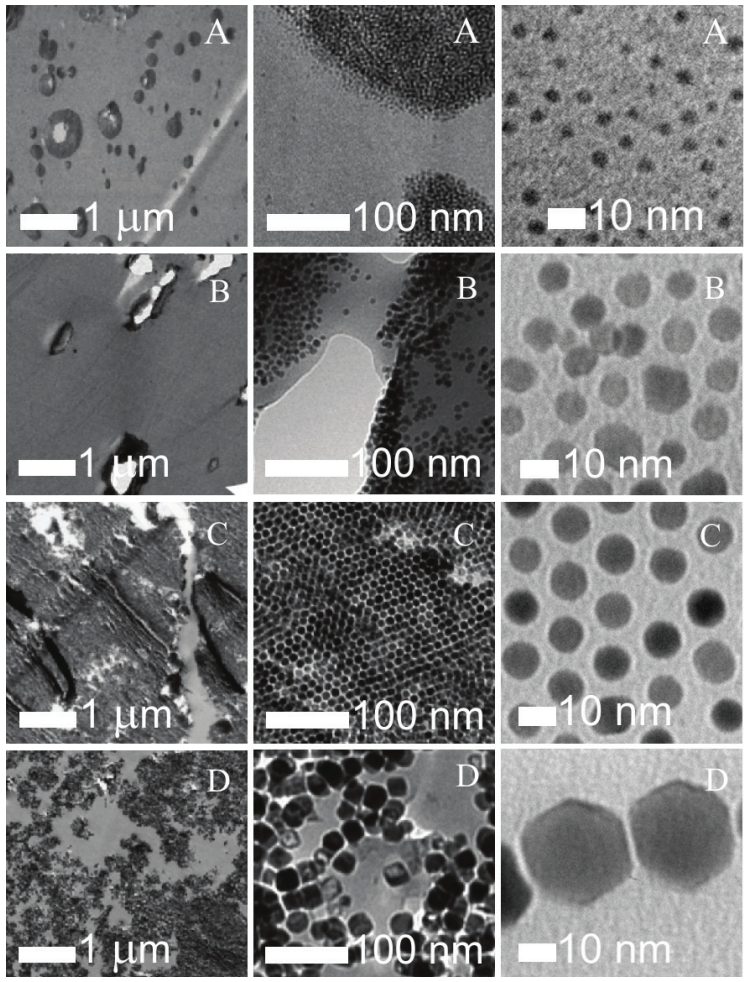

Figure 3.19. The TEM images of ϵ-cobalt nanoparticles composites (Set 2010). a) Sample-A contains nanoparticles with the average diameter of 5 nm, but chains of bigger particles ($\approx$10nm) are also observed. b) Sample-B contains nanoparticles with the average diamter of 8 nm, c) Sample-C contains nanoparticles with the average diameter of 11 nm, and d) Sample-D contains bigger facet-particles with the average size of 27 nm. Note that the TEM images on the right column with 10 nm scale bar are the images of particles in the original solution before the making of composite materials. (The figures are from Publication VI)

cles (sample-C) with bigger facet particles with an average diameter of 27 nm, we found that the facet particles (Sample-D) exhibit a smaller absorption at and around 1 GHz. The unusually high magnetic loss in sample-C can be caused by the formation of superlattices inside the composite.

Monodispersed ϵ-cobalt nanoparticles

Chemical synthesis allows the production of nearly monodispersed ϵ-cobalt nanoparticles. The composite materials made by mixing the monodis-

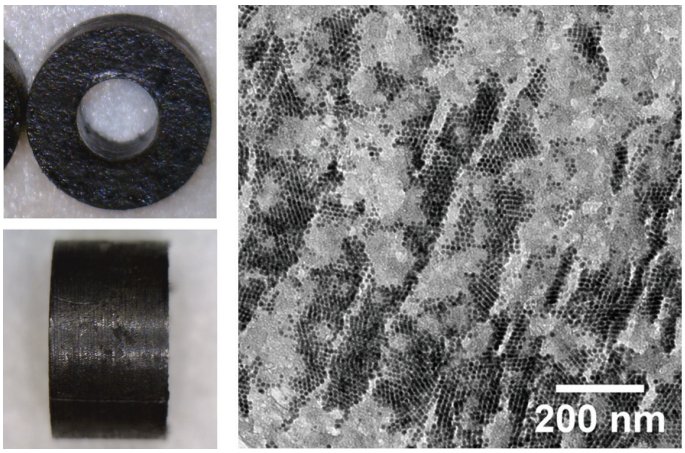

Figure 3.20. Left: a pellet of sample-C composite for microwave measurements. Right: the TEM image of particle clusters inside the sample-C composite.

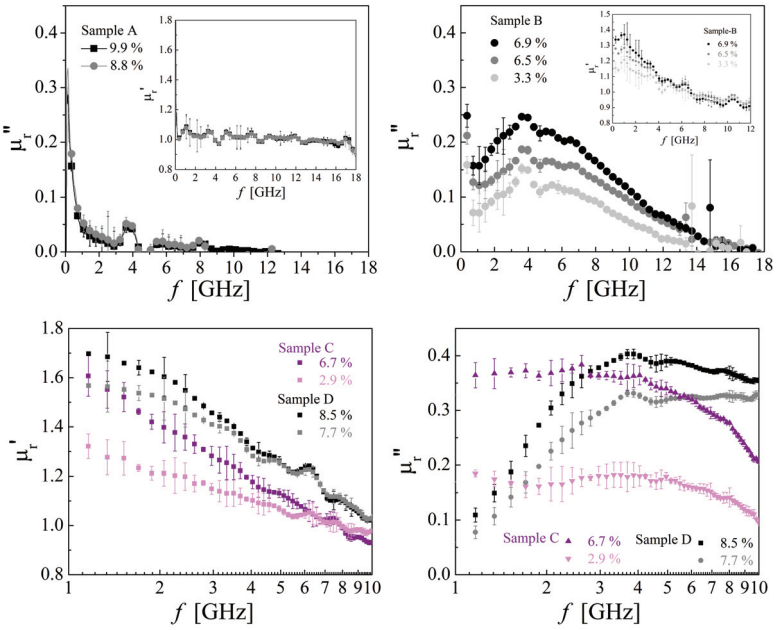

Figure 3.21. The relative magnetic permeability of ϵ-Co composites (Set 2010): A, B, C and D samples. (The figures are from Publication VI)

persed particles and insulating matrix have been studied. Some results are reported in Publication VI. In that paper, a composite of monodispersed ϵ-cobalt nanoparticles with an average diameter of 14 nm exhibits broad magnetic absorption within the frequency range between 1 and 10 GHz, with a peak around 3 GHz, see Fig. 3.22. It was also found that increasing the volume fraction not only increases the magnitude of μ_r'', but also shifts the resonant peak towards lower frequencies. This ob-

servation agrees with the prediction by the Bruggeman effective medium model (Fig. 3.23). However, the spectra, particularly the real part of permeability, were not well described by the model.

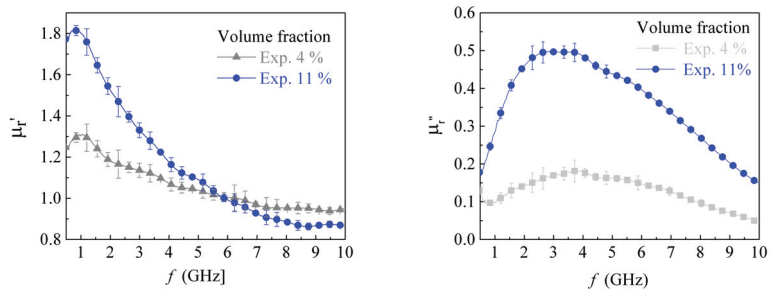

Figure 3.22. The magnetic permeability of two composites made from 14-nm monodispersed ϵ-cobalt particles with different volume fraction. (The figures are from Publication VI)

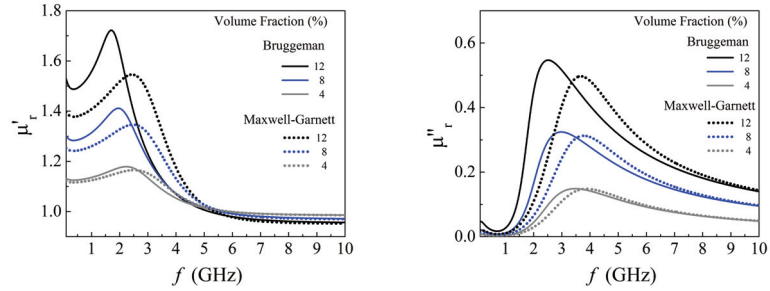

Figure 3.23. The predicted magnetic permeability of the composite made from 14-nm monodispersed ϵ-cobalt particles based on the Bruggeman and Maxwell-Garnett effective medium model. (The figures are from Publication VI)

Figure 3.24 shows the atomic force microscopic (AFM) and magnetic force microscopic (MFM) images of an area on this composite. In addition to the visible magnetic particles/clusters in the MFM image, we also observe that, within the area of 100 nm^2, the magnetization direction/magnitude is not homogeneous. Different magnetization regions may correspond to the formation of big clusters or pseudolattice inside the composites. The clustering can occur either during the synthesis process or during the hot-plate molding of the toroidal samples.

Next, we will present a study on another set of monodispersed ϵ-cobalt nanoparticles. The average size of the particles in this set is 11.7 nm. Figure 3.25 shows the transmission electron microscopy pictures of the nanoparticles.

Figure 3.26b shows the zero-field cooled/field cooled (ZFC/FC) curve of

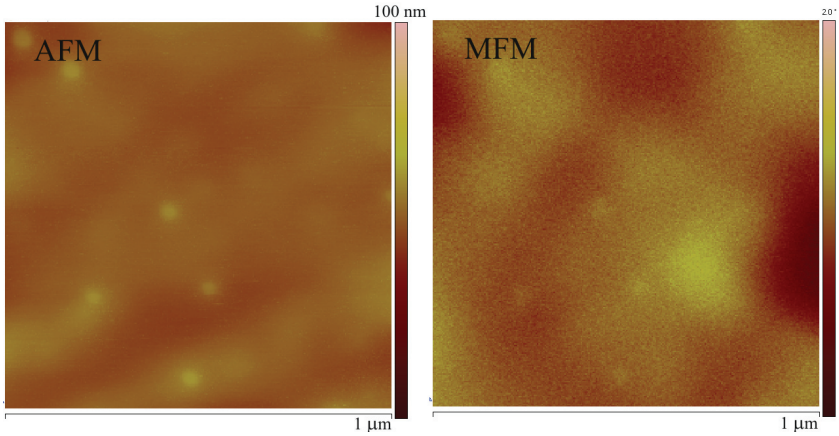

Figure 3.24. The AFM and MFM images of the composite made from the 14-nm monodispersed ϵ-cobalt particles. (Unpublished data)

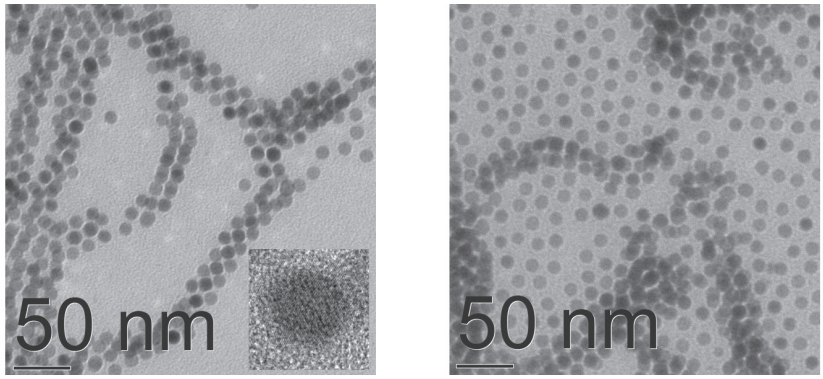

Figure 3.25. Transmission electron microscopic images of monodispersed ϵ-cobalt nanoparticles (Set 2012). The average particle diameter is 11.7 $\pm$ 0.7 nm. (Unpublished data)

the 11.7-nm monodispersed ϵ-cobalt nanoparticle composite. The measurement was done by firstly cooling a small piece of a sample to 2 K without an external magnetic field for a ZFC measurement. At the end, the sample was frozen with no net magnetization, due to the random magnetization at room temperature. Next, a small field (100 Oe) was applied, and the magnetization (M) of the sample was measured at different temperatures from 2 to 400 K. As the temperature increases, more particles undergo a transition from the ferromagnetic (blocked) to the paramagnetic phase, and align with the applied field. The magnetization reached a maximum when the blocking temperature was reached. The blocking temperature is the temperature for which thermal excitation occurs. In other words, the thermal energy causes fluctuation between the parallel and antiparallel magnetization states with respect to the anisotropy axis.

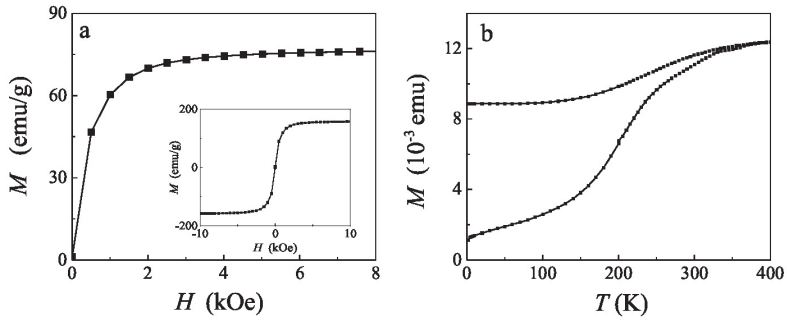

Figure 3.26. The magnetic response of a ϵ-cobalt nanoparticle composite (Set 2012) measured by a SQUID magnetometer. a) The magnetization versus the applied magnetic field at 300 K showing the saturation magnetization of about 77 emu/g. The inset picture is the result of another section from the same sample. b) The ZFC-FC curve of the same sample showing the blocking temperature above room temperature. (From publication VI)

As temperature was further increased, the fluctuations caused the magnetization to orient randomly, resulting in a decrease of the magnetization at a higher temperature.

At microwave frequencies between 0.1 and 10 GHz, the composites of the monodispersed particles exhibit magnetic resonant absorption which peaks between 2 and 3 GHz, see Fig. 3.27. Increasing the volume fraction causes the peak to shift towards lower frequencies. This effect was also observed in other samples, as reported in Publications V and VI. The permittivity spectra show that the dielectric response is less dispersive. The imaginary permittivity is nearly zero over the whole frequency range, such that the microwave absorption must be caused only by the strong magnetic coupling between the field and the magnetic particles at ferromagnetic resonance. Figure 3.28 shows the same data in logarithmic scale. Some samples from the "sample set 2012" have also been characterized by the short-circuit line method (Publication V). The results agree well with the measured results obtained by the transmission/reflection method presented in this section.

3.5.3 Conclusions

Compared with the polydispersed fcc-Co nanoparticle composite, a composite of polydispersed ϵ-Co nanoparticles (with the diameter in the order of 10 nm) exhibits ferromagnetic resonance at lower frequencies: 12 GHz for fcc-Co and 4 GHz for ϵ-Co. At a low volume fraction, the polydispersed fcc-Co composite and the polydispersed ϵ-Co composite have nearly the

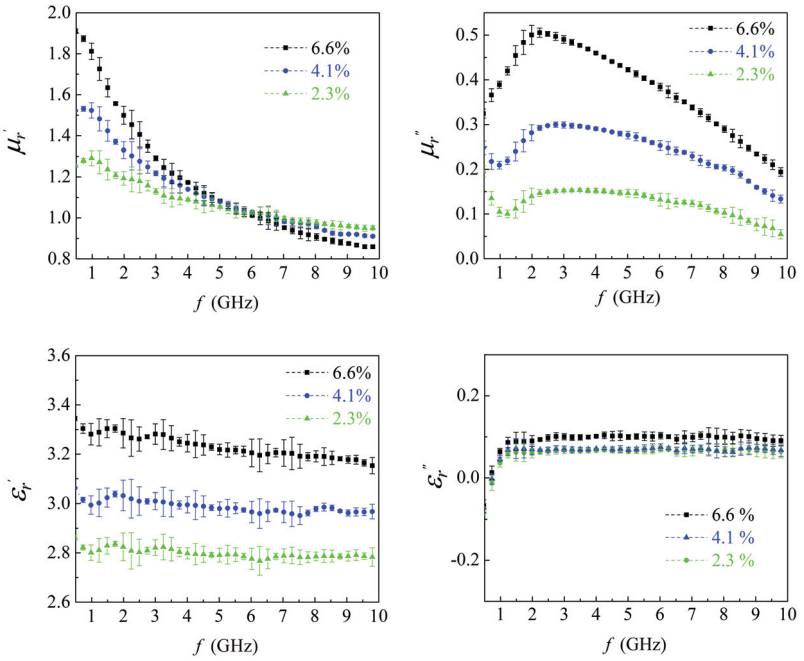

Figure 3.27. The relative permittivity $\epsilon_r = \epsilon_r' - i\epsilon_r''$ and relative permeability $\mu_r = \mu_r' - i\mu_r''$ of ϵ-cobalt nanoparticle composites (Set 2012) at different volume fractions. (Unpublished data)

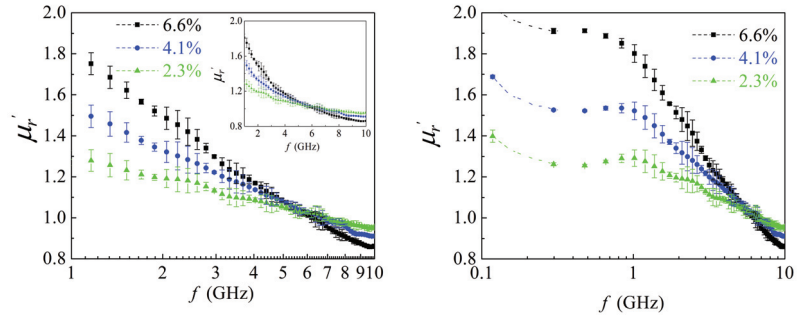

Figure 3.28. The relative permittivity $\epsilon_r = \epsilon_r' - i\epsilon_r''$ and relative permeability $\mu_r = \mu_r' - i\mu_r''$ of ϵ-cobalt nanoparticle composites (Set 2012) at different volume fractions in logarithmic scale. (Unpublished data)

same magnetic response ($\mu_r'' \approx 1.4$) at the frequencies between 1 and 2 GHz. Without external magnetizing field, both monodispersed and polydispersed ϵ-Co composites have broad ferromagnetic resonance peak in frequency domain.

With the currently available synthesis methods, magnetic nanoparticles usually aggregate in the form of clusters, chains and superlattices. The aggregation can be found in all of the composite materials. This

self-organization of magnetic nanoparticles generally reduces the free energy of the system. But, in terms of magnetic energy, the aggregation of nanoparticles can result in the increase of anisotropy, $i.e.$ an increase of the effective anisotropic field. So, when these nanoparticle clusters are observed under microwave radiation, they therefore respond as if they are subjected to an external (local) magnetizing field. This natural process may be a reason why some observations of cobalt nanoparticles under microwave radiation show a magnetic loss absorption peak at frequencies much higher than expected by the non-interacting uniaxial particle model.

3.6 Carbon nanotubes

Technologically, both magnetic and non-magnetic materials are useful for the design and development of microwave applications. As non-magnetic materials, carbon nanotubes are among the most versatile nanomaterials. Due to the remarkable electronic [96], thermal [97] and mechanical [98, 99, 100], electrical [96] properties, carbon nanotubes may be applied to fabricate lighter-weight devices with applications ranging from consumer electronics to space science.

For scientific purposes, arc discharge [101, 102], chemical vapor deposition [103] [3], laser ablation [104] and controlled flame environment [105] are widely-used techniques for the production of single-walled and multi-walled carbon nanotubes.

The observations of nanotubes with an electron microscope dates back to only half a century ago. However, a recent study shows that a 17th century sword made from Damascus steel contains carbon nanotubes [106]. This discovery provides evidence that human beings have been using carbon nanotubes since ancient times. A single-wall carbon nanotube is a flexible cylindrical tube formed from a single sheet of hexagonal network of carbon atoms, see Fig. 3.29. The electronic structure and the associated electrical properties of a single-wall carbon nanotube is determined by the chiral vector as shown diagramatically in Fig. 3.29.

Theoretical and experimental studies on the electronic structures of carbon nanotubes demonstrate that armchair ($n = m$) nanotubes have energy

[3] By using a catalytic vapor phase deposition of carbon, Radushkevich and Lukyanovich found in 1952 that carbon filaments could be hollow and have a nanometer-size diameter.

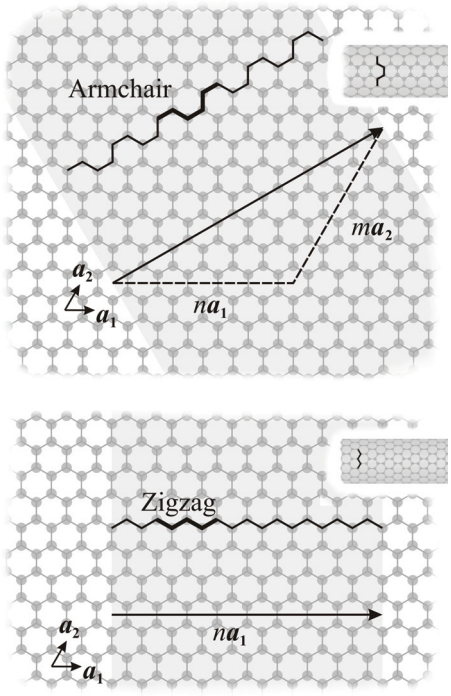

Figure 3.29. Diagram showing how different types of single-walled carbon nanotubes (SWCNT) can be constructed from a graphene sheet. The chirality and the tube diameter are uniquely specified by the chiral vector $C_h = n\vec{a_1} + m\vec{a_2}$, where n, m are integers and a_1, a_2 are the unit vectors of graphite, and C_h connects two edges of the rectangular graphitic sheet (dark color region). An armchair SWCNT is formed when $n = m$, while a zigzag SWCNT is formed when $m = 0$.

bands crossing the Fermi level and are therefore metallic, while chiral ($n \neq m$) and zigzag ($m = 0$) can be either metallic or semiconducting depending on the chiral angle [107, 108, 109]. It has been shown that when $n - m = 3l$, where l is an integer, the tubes are metallic; in other cases ($n - m \neq 3l$), the tubes are semiconducting with an energy gap (depending on the diameter) of the order of 0.5 eV. The chiral angle is defined as the angle between $\vec{C_h}$ and the zigzag θ (or armchair ϕ) direction. If the chiral angle is defined as the angle between $\vec{C_h}$ and the zigzag, then a zigzag tube will have the chiral angle $\theta = 0^o$, $\theta = \arctan -\sqrt{3}m/(2n + m)$. Similarly, if the chiral angle is defined as the angle between $\vec{C_h}$ and the armchair, then an armchair tube will have the chiral angle $\phi = 0^o$.

In this section, the experimental investigations of some carbon nanotube materials are presented. The objectives are a) to characterize the dielectric properties of carbon nanotube composites, and b) to test the scattering and absorption properties of carbon nanotube yarns.

3.6.1 Single-walled carbon nanotube composites

Composites made by mixing single-walled carbon nanotubes (mixed chirality) and dielectric matrix were studied at microwave frequencies. The dielectric permittivity spectra of the composites at frequencies between 7 and 11 GHz are shown graphically in Fig. 3.30. The measurements were done by using a transmission/reflection technique (see Appendix B). The permittivity spectra were retrieved by using a reference-plane invariant algorithm presented in Publication I.

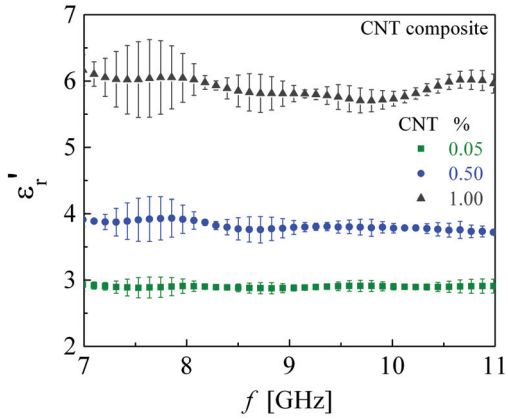

Figure 3.30. The microwave dielectric constant (relative permittivity $\epsilon_r = \epsilon_r' - i\epsilon_r''$) of composite materials made by mixing single-walled carbon nanotubes (mixed chirality) with dielectric matrix. (Unpublished data)

3.6.2 Carbon nanotube yarn

In this subsection, yarns of multiwall carbon nanotube are studied, and found to behave like metallic grids with large anisotropic properties.

Due to the electronic structure of multiwall carbon nanotubes (MCNT) [110], a sheet of aligned MCNT yarns [111] has very high electrical conductivity (DC) along the yarn axis (Fig. 3.31). The asymmetry of the MCNT sheet also causes anisotropy effects at microwave frequencies. Fig. 3.32 demonstrates how the anisotropic properties of the MCNT yarns are measured using a rectangular waveguide. The results of the transmission and reflection measurements show that the absorbance is higher when the MCNTs are perpendicular to the direction of the propagating electric field, see Fig. 3.33. At frequencies from 8.0 to 9.0 GHz, the incident electric field that aligned with the CNT yarn will be absorbed with the

absorbance ($1 - |S_{11}|^2 - |S_{21}|^2$) of about 0.1, while the absorbance of the perpendicular field is approximately 0.5. This finding is actually similar

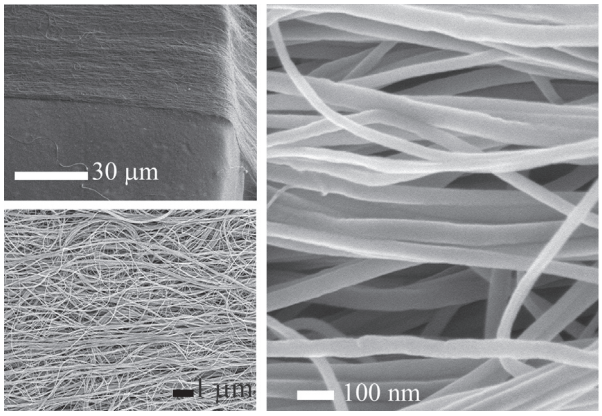

Figure 3.31. The scanning electron microscopy images of multiwall carbon nanotube yarn, made from multiwall carbon nanotubes aligned mainly in one direction (yarn axis); each tube has the length of about 1.5 mm.

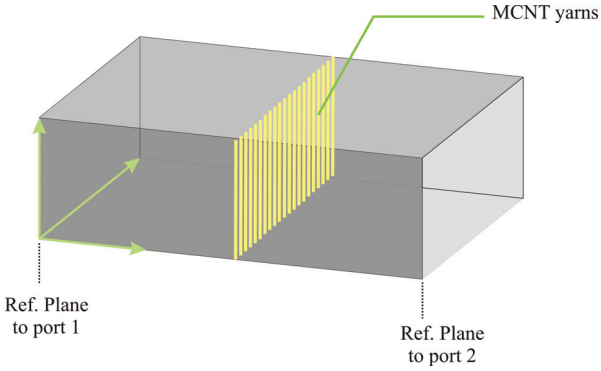

Figure 3.32. The rectangular waveguide used to measure the anisotropic properties of MCNT yarns.

to the case of metallic grid; the surface impedance of the grid depends strongly on the direction of the incident field. In order to have a higher absorption in a structure, we should design the structure to reflect less power. Ideally, a near unity absorbance can be achieved when the structure has zero reflection and zero transmission. This condition is difficult to obtain in practice, so in many cases a good absorber is designed first to match the impedance of the vacuum, in order to obtain the highest power from the incident field. A theoretical study of unity absorbance layers is presented and discussed in more details in Publication II.

With a resonant cavity, see Fig. 3.34, small samples can be accurately characterized. In the following, the cavity is designed and fabricated with a sample insertion hole in the middle of the top surface. The description

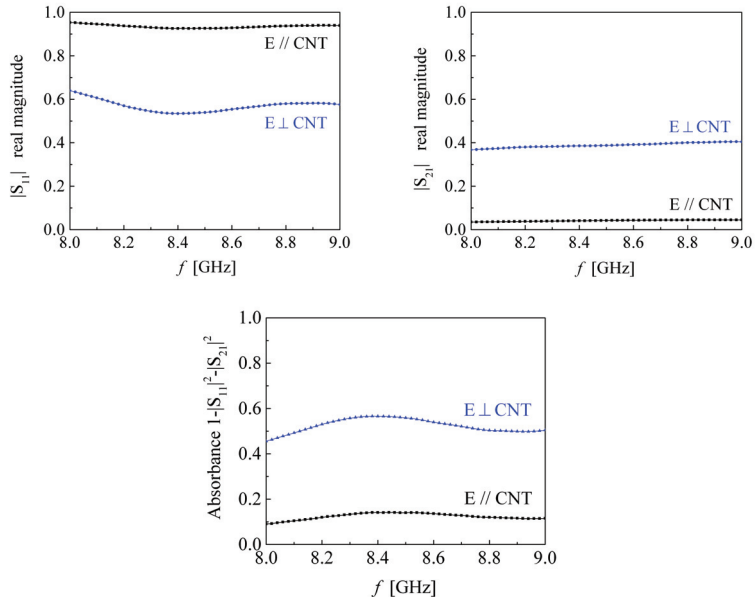

Figure 3.33. Microwave anisotropic properties of the MCNT yarn at frequencies between 8 and 9 GHz. (Unpublished data)

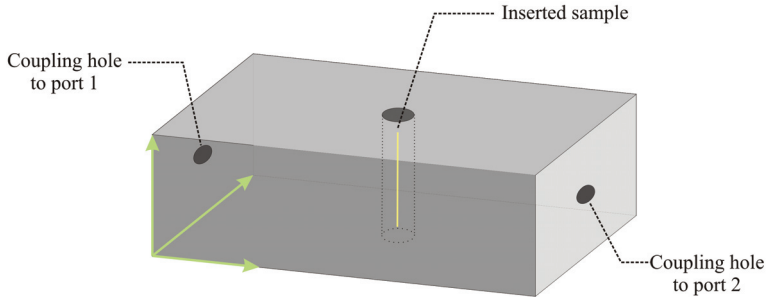

Figure 3.34. The resonant cavity used for testing small samples of MCNT yarns.

of the resonant modes can be found in Appendix A. Figure 3.35 shows the measured results when a small rectangular sheet of MCNT yarn is placed in the middle of the rectangular cavity in the way that the MCNT points in the same direction as the electric field. The absorbance of the parallel field can be as high as 0.7, at and around the resonance frequency of the cavity. It is also seen that the larger the sample, the higher the reflection. As a result, a larger sample does not absorb that much power.

Figure 3.36 shows the reflection S_{11} and absorbance spectra from the resonant cavity when filled with various types of materials. Comparing with a copper wire and a smaller piece of MCNT yarn leads to increased reflection, but the shift of resonant frequency is smaller due to the smaller perturbation of the resonant cavity mode. We have found experimentally

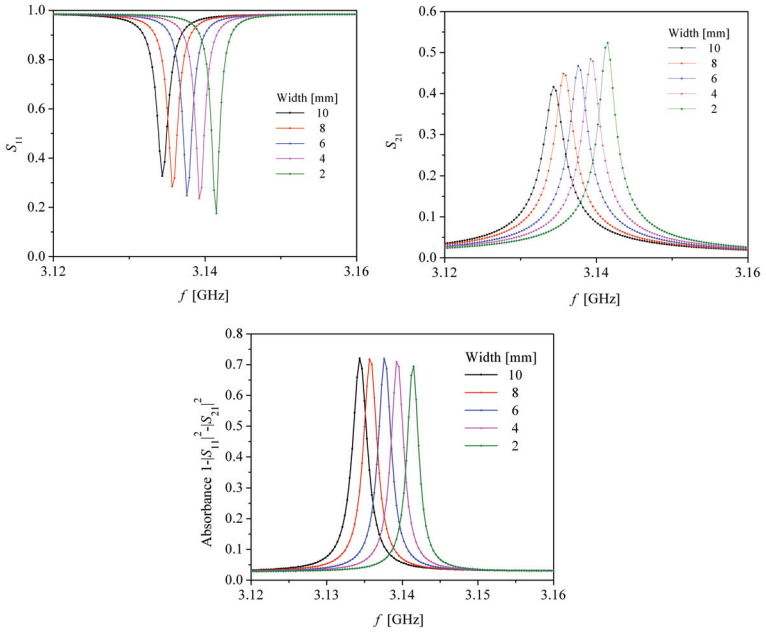

Figure 3.35. Microwave analysis for a rectangular sheet of MCNT yarn with the length of 10 mm and width of various lengths. The transmission (S21) and reflection (S11) through a resonant cavity when a small piece of MCNT yarn is inserted; the yarn axis points in the same direction with the electric field. The absorbance is calculated from the relation A = $1 - |S_{11}|^2 - |S_{21}|^2$. (Unpublished data)

that when the same MCNT yarn is attached to an end of a copper wire and the combined sample is inserted back into the cavity, unusually large reflection occurs.

3.6.3 Conclusions

Similar to macroscopic materials, anisotropy determines the coupling mechanisms between a nanostructured material and a microwave radiation under an observation. Classically, the interaction can be due to either magnetic or electric coupling between the field and the material. In nonmagnetic materials, such as carbon nanotubes, anisotropy allows the materials to interact strongly only with the electric field with the polarization parallel to the tube axis. Because of this nature, a piece of a multi-walled carbon nanotube yarn is less visible (low scattering and reflection) at microwave frequencies when the yarn axis is perpendicular to the field. But when the yarn axis is rotated so that it is parallel to the field, the nanotube yarn becomes clearly visible with large observable scattering. This anisotropic nature of the scattering process therefore highlights a similar-

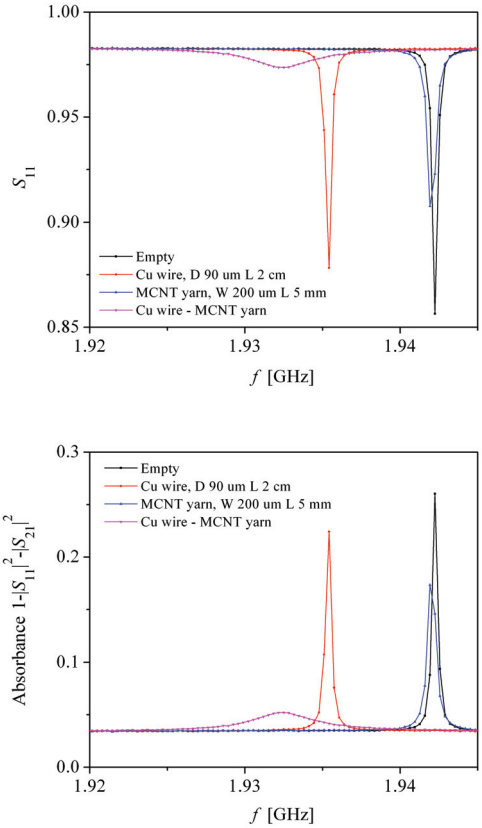

Figure 3.36. The reflection (S_{11}) and absorbance spectra for a resonant cavity with different inserted samples. The reflection from the cavity is larger when a small piece of MCNT yarn is inserted, as compared to the case of a bigger piece of copper wire. For the big copper wire, the electric field is highly perturbed, and there is a larger shift in the resonant frequency of the cavity. If we attach the same pieces of MCNT yarn at one end of the copper wire, the reflection becomes significantly larger. (Unpublished data)

ity between macroscopic and the nanoscopic materials. However, in the study of carbon nanotube yarn at microwave frequencies, an unexpected phenomenon was also observed. It was found that only a short ($L \ll \lambda$) carbon nanotube yarn (with the diameter in the order of 100 μm) can be used together with other metallic materials to create a composite material with remarkable microwave properties. As we have shown here, a copper wire with its axis parallel to the microwave electric field can couple and generate scattering many times stronger than usual when the end of the wire is connected with a tiny piece of carbon nanotube yarn.

4. Main Results and Conclusions

The development of future nanoscale devices requires not only precise knowledge of the material properties, but also innovative ways to fabricate structures at mesoscopic scales. In my thesis, I have demonstrated two novel fabrication concepts based on ion-induced inelastic strain engineering. The first concept involves the use of the well-established focused ion-beam technology. The concept has been demonstrated experimentally by fabricating various non-trivial 3D structures, including cubic structures, at nanometer scales. The second concept is a new hybrid nanofabrication technique. The main idea is to induce inelastic strain by using low-energy ions generated during a reactive plasma etching process. This technique was applied to assemble self-folding structures with various radii of curvature using a single ion etching process.

Regarding the microwave properties of nanomaterials, experimental investigations show that a composite material made of a mixture of dielectric material and ϵ-cobalt nanoparticles with sizes between 7 nm and 20 nm exhibits ferromagnetic resonant absorption which peaks at around 2 to 4 GHz. At high magnetizing fields (above 1.5 kOe), the ferromagnetic resonance approximately follows Kittel's FMR theory. The resonance peak at high field values can be described by combining the Landau-Lifshitz-Gilbert equation with the effective medium model. At lower field values, the resonance occurs at higher frequencies compared to the prediction by Kittel's single-particle FMR model. The shift of the resonance is hypothesized to be due to the local magnetizing field that arises from the interaction of particles inside particle clusters. Transmission electron microscope images show that the particles inside the composite aggregate in the form of chains and superlattices.

For carbon nanotube materials, experimental results show that the interaction between the CNT yarns and microwave radiation depends strongly

on the polarization (yarn axis). Inserting a thin piece of carbon nanotube yarn ($L \approx \lambda/2, w \ll 100$ μm) inside a microwave cavity and measuring the reflected and transmitted signals, we find that the combined system (the CNT yarn and the cavity) exhibits high reflection when the yarn is parallel to the field in the resonant cavity. A very high reflection signal occurs if one attaches a small ($L \ll \lambda/2, w \ll 100$ μm) piece of CNT yarn to a thin metal wire ($L_{\mathrm{metal}} \approx \lambda/2$) and inserts this combination into the cavity. The finding suggests that structures exhibiting ultra high reflection (shielding) may be fabricated by combining metallic wires with multi-walled carbon nanotube yarns.

Nanoscale materials have many promising and useful applications in science and technology, but there are also some environmental and ecological concerns about the use of these materials. Therefore, mass-production of nanostructured materials would require further research and development to make sure that the new materials are biologically and ecologically compatible.

A. Appendix: Microwave Theory and Techniques

This appendix discusses microwave theory and techniques in the context of classical electrodynamic theory. It is not aimed to cover the whole research area, but rather to present some basic concepts for the understanding of experimental methods used in Chapter 3. (The author's contributions to the knowledge of microwave techniques are summarized in Publication I and V.)

A.1 Microwaves

Electromagnetic waves in the range of microwave frequencies have wavelengths ranging from 1 m to 1 mm, corresponding to frequencies between 300 MHz and 300 GHz. At the quantum limit microwave energy is transferred to/from a materials in discrete amounts, called 'photons'. Microwave photons have an energy ranges between 1.24 μeV (at 300 MHz) and 1.24 meV (at 300 GHz). For a mobile phone operating at 1 GHz, a corresponding microwave photon would have an energy of about 1.26×10^{-24} J or 7.86 μeV.

A.1.1 Microwave power units

The decibel (dB) is a logarithmic unit that expresses the magnitude of a physical quantity relative to a reference level. Since the unit quantifies the ratio of two quantities having the same units, it is a dimensionless unit. In the microwave literatures, dBm (dBmW) is referenced to one milliwatt (mW), x dBm = $10 \log_{10} P/P_0$, where P is the measured power and $P_0 = 1$ mW is the reference power. For example, 1 mW = 0 dBm, 10 mW = 10 dBm, and 100 mW = 20 dBm.

A.2 Measurement Techniques

The interaction between the magnetic nanocomposites and the transmitted microwave can be described classically in terms of material constitutive parameters, $i.e.$ the complex permittivity ϵ_r, and the complex permeability μ_r. The imaginary parts of the constitutive parameters determine how large the radiation energy is absorbed.

This section discusses the measurement methods for the determination of constitutive parameters at microwave frequencies. Generally, microwave measurement techniques can be classified as resonant or non-resonant. The study of magnetic resonant phenomena was conventionally done with resonant methods. However, the advancement of microwave instrumentation has allowed also the study of resonant phenomena in frequency domain using non-resonant methods. Non-resonant methods can involve the measurement of transmission/reflection or reflection only.

A.2.1 Transmission/reflection methods

Non-resonant techniques such as the transmission/reflection method provides a way to observe magnetic resonance phenomena under zero magnetizing field. Material properties at microwave frequencies are widely characterized by the transmission and reflection measurement. The refractive index, n, and the permittivity, ϵ, are examples of the properties that have been measured with these techniques. A well-known technique which provide both permittivity and permeability, μ, in one measurement is the transmission/reflection (TR) method introduced by Nicholson-Ross [112] and Weir [113]. This technique has a technical problem involving the transformation of S-parameter measurements from the calibration reference planes to the surfaces of the material. To solve it, Baker-Jarvis and co-workers proposed a set of reference-plane independent equations for the determination of complex permittivity [114]. They derived five scattering equations that are invariant to the positions of reference planes. Since many measurement methods are designed for characterizing non-magnetic materials, the permeability of the material being tested is usually assumed to be 1 in the calculation algorithms [114]-[115].

In general, it would be useful to extract all of the electromagnetic parameters of a material being tested. Fig. A.1 shows the relation between four fundamental physical constants and the corresponding electromagnetic parameters, which can be measured by transmission/reflection tech-

nique. In case of a non-magnetic material, the refractive index relates to

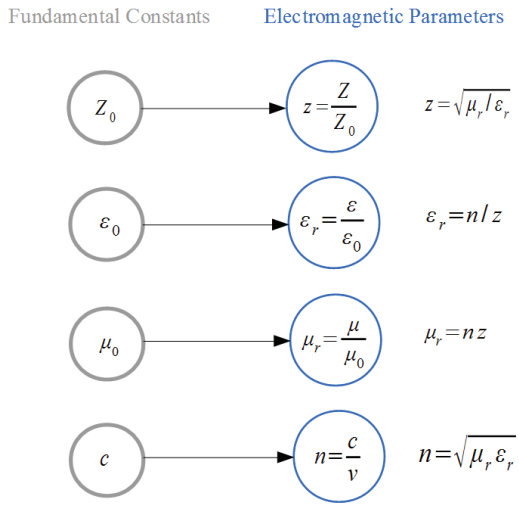

Figure A.1. Fundamental physical constants and electromagnetic parameters. It is sufficient to measure either n and z or ϵ and μ, because when a pair of parameters is known one can always calculate the other pair.

only the permittivity. But the refractive index of a magnetic material is also dependent on the permeability, $n = \sqrt{\mu\epsilon}$. In the following, the mathematical descriptions of the scattering parameters will be discussed. The aim is to find a reference-plane invariant algorithm for the determination of complex refractive index and wave impedance. When the index of refraction $n = n' + n'' = \sqrt{\epsilon\mu}$ and the wave impedance $z = \sqrt{\frac{\mu}{\epsilon}}$ are known, the permittivity and permeability can then be determined.

Transverse electromagnetic waves

The foundation of classical electromagnetic theory was firmly established when J. C. Maxwell modified the Ampere's law (an electric current produces a magnetic field) with an additional assumption that a changing electric field also produces a magnetic field in a similar way to how a changing magnetic field produces an electric field, and combined his modified law with the other electrostatic and magnetostatic laws to create the most-important equation of the 19th century - the equation that predicts the existence of electromagnetic waves that travel with the speed of light $c = 1/\mu\epsilon$ [116]. Maxwell's prediction was confirmed experimentally using a set of simple generator and reciever by H. Hertz in 1887.[1]

[1]Hertz's electromagnetic field generator was made from a battery and a simple LC circuit. He also separated the electrical line between the capacitor and the inductor with a small air gap. This air gap between two well-polished brass

According to Faraday and Ampere's laws (Maxwell's curl equations) [117, 118],

$$\nabla \times E = -\mu \frac{dH}{dt} \tag{A.1}$$

$$\nabla \times H = J + \epsilon \frac{dE}{dt}, \tag{A.2}$$

where $\mu = \mu_0 \mu_r$ is the magnetic permeability and $\epsilon = \epsilon_0 \epsilon_r$ is the permittivity. If we assume that 1) the transmission line is source-free ($J = 0$), isotropic and homogeneous, 2) EM waves propagate along z-axis with $e^{j\omega t}$ dependence, and 3) there are only transverse electromagnetic (TEM) waves propagating within the line ($E_z = H_z = 0$), we will find that the transverse field component E_ρ (or H_ϕ) is governed by

$$\frac{\partial^2 E_\rho}{\partial z^2} + \omega^2 \mu \epsilon E_\rho = 0. \tag{A.3}$$

This means that there is a sinusoidal electric field in the transverse direction. The mathematical expression of the field is given by Eq. (A.4).

Mathematically, a sinusoidal wave of electric field E travelling along the z-direction within a transmission line can be described in terms of the angular frequency ω and the proportional constant γ as follows:

$$E_\rho(z,t) = C^+ e^{j\omega t - \gamma z} + C^- e^{j\omega t + \gamma z}, \tag{A.4}$$

where $\gamma = j\omega\sqrt{\mu\epsilon}$ and t is time. Like other plane waves, the first term on the r.h.s. of (A.4) represents a wave propagating in the +z direction, while the second term is the one propagating in the opposite direction. For simplicity, we will, from now, describe all the fields using their phasor forms. This means the time-dependent factor $e^{j\omega t}$ will be suppressed. For example, the phasor form of (A.4) is

$$E_\rho(z) = C^+ e^{-\gamma z} + C^- e^{\gamma z}. \tag{A.5}$$

The propagation of TEM waves in homogeneous waveguides can be described in terms of plane waves. If the line is filled partly with a piece of material, a fraction of the incident wave will get reflected at the first and also at the second interface. In practice, unknown reflection can also occur, for examples, at a defect of a waveguide or at a joint between a waveguide and an adapter.

knobs was expected to generate sparks during the electrical generation. Hertz reasoned that, if Maxwell were correct, electromagnetic waves would be created during these sparks. To detect the transmitted waves, Hertz placed a simple receiver (a looped wire with both of its end separated by a tiny gap) a few meters away from the generator. He found that whenever there were sparks at the generator, there were also sparks generated at the gap of the metal-loop receiver.

In the case that the reflection and absorption of the waveguide can be eliminated, we can use the reflection and transmission signal to determine material constitutive parameters. Recall that the constitutive relations can be written:

$$D = \epsilon E, \tag{A.6}$$

and

$$H = B/\mu. \tag{A.7}$$

In general, the electric permittivity ϵ and the magnetic permeability μ are not constants, but rather functions of frequency. At a chosen frequency, a material is said to be non-magnetic, if its permeability is equal to μ_0, *i.e.* with $\mu_r = \mu/\mu_0 = 1$. When expressing the material properties in terms of the intrinsic electromagnetic parameters, like ϵ and μ, their magnetic properties can also be described in terms of electric permittivity $\epsilon =$ and magnetic permeability μ, The wave impedance z and the refractive index n of the material inserted inside the waveguide. Here, we will focus our analysis on the transmission and reflection at the interface between a material under test and the air within a transmission line. The schematic illustration of this model system is shown in Figure A.2. The wave impedance z and the refractive index n of the material inserted inside the waveguide.

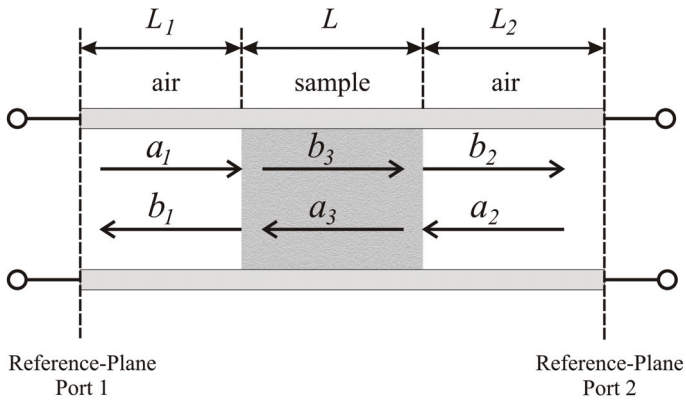

Figure A.2. Diagram of transmission line segment containing material under test. The arrows represent the transmitted and reflected signals through the transmission line.

Within region I and III, the electric fields propagate through air, so they are governed by

$$\gamma_0 = j\omega\sqrt{\mu_0\epsilon_0} = j\frac{\omega}{c}. \tag{A.8}$$

While, in region II, this characteristic parameter changes to

$$\gamma = j\omega\sqrt{\mu\epsilon} = j\omega\sqrt{\mu_0\mu_r\epsilon_0\epsilon_r} = \gamma_0\sqrt{\mu_r\epsilon_r}, \tag{A.9}$$

where μ_r and ϵ_r are the relative permeability and permittivity of the material under test.

By using notations as in figure A.2, we can write the mathematical expressions for the incident and reflected waves within each region as

$$E_I = a_1 e^{-\gamma_0 z} + b_1 e^{\gamma_0 z}, \tag{A.10}$$

$$E_{II} = b_3 e^{-\gamma_0\sqrt{\mu_r\epsilon_r}z} + a_3 e^{\gamma_0\sqrt{\mu_r\epsilon_r}z}, \tag{A.11}$$

$$E_{III} = b_2 e^{-\gamma_0 z} + a_2 e^{\gamma_0 z}. \tag{A.12}$$

The amplitudes (a_i, b_i) of each wave components can be determined by solving (A.10-A.12) with the following boundary conditions:

$$E_I|_{z=L_1} = E_{II}|_{z=L_1}, \tag{A.13}$$

$$E_{II}|_{z=L_1+L} = E_{III}|_{z=L_1+L}. \tag{A.14}$$

and

$$\frac{1}{\mu_0}\frac{\partial E_I}{\partial z}|_{z=L_1} = \frac{1}{\mu_0\mu_r}\frac{\partial E_{II}}{\partial z}|_{z=L_1}, \tag{A.15}$$

$$\frac{1}{\mu_0\mu_r}\frac{\partial E_{II}}{\partial z}|_{z=L_1+L} = \frac{1}{\mu_0}\frac{\partial E_{III}}{\partial z}|_{z=L_1+L}. \tag{A.16}$$

Solving (A.10) - (A.12) with (A.13) - (A.16), we obtain

$$\begin{pmatrix} b_1 \\ \\ b_3 \end{pmatrix} = \begin{pmatrix} \frac{1-\sqrt{\frac{\epsilon_r}{\mu_r}}}{1+\sqrt{\frac{\epsilon_r}{\mu_r}}} e^{-2\gamma_0 L_1} & \frac{2\sqrt{\frac{\epsilon_r}{\mu_r}}}{1+\sqrt{\frac{\epsilon_r}{\mu_r}}} e^{-\gamma_0(1-\sqrt{\epsilon_r\mu_r})L_1} \\ \\ \frac{2}{1+\sqrt{\frac{\epsilon_r}{\mu_r}}} e^{-\gamma_0(1-\sqrt{\epsilon_r\mu_r})L_1} & -\frac{1-\sqrt{\frac{\epsilon_r}{\mu_r}}}{1+\sqrt{\frac{\epsilon_r}{\mu_r}}} e^{2\gamma_0\sqrt{\epsilon_r\mu_r}L_1} \end{pmatrix} \begin{pmatrix} a_1 \\ \\ a_3 \end{pmatrix} \tag{A.17}$$

and

$$\begin{pmatrix} a_3 \\ \\ b_2 \end{pmatrix} = \begin{pmatrix} -\frac{1-\sqrt{\frac{\epsilon_r}{\mu_r}}}{1+\sqrt{\frac{\epsilon_r}{\mu_r}}} e^{-2\gamma_0\sqrt{\epsilon_r\mu_r}(L_1+L)} & \frac{2}{1+\sqrt{\frac{\epsilon_r}{\mu_r}}} e^{\gamma_0(1-\sqrt{\epsilon_r\mu_r})(L_1+L)} \\ \\ \frac{2\sqrt{\frac{\epsilon_r}{\mu_r}}}{1+\sqrt{\frac{\epsilon_r}{\mu_r}}} e^{\gamma_0(1-\sqrt{\epsilon_r\mu_r})(L_1+L)} & \frac{1-\sqrt{\frac{\epsilon_r}{\mu_r}}}{1+\sqrt{\frac{\epsilon_r}{\mu_r}}} e^{2\gamma_0(L_1+L)} \end{pmatrix} \begin{pmatrix} b_3 \\ \\ a_2 \end{pmatrix} \tag{A.18}$$

Combining (A.17) and (A.18), we obtain the relation between the magnitudes of the incident, reflected, and transmitted signals:

$$\begin{pmatrix} b1 \\ \\ b2 \end{pmatrix} = \begin{pmatrix} S'_{11} & S'_{12} \\ \\ S'_{21} & S'_{22} \end{pmatrix} \begin{pmatrix} a_1 \\ \\ a_2 \end{pmatrix}, \tag{A.19}$$

which shows that the scattering (S') matrix relates the incoming waves toward the sample to the corresponding outgoing waves.

The elements of a scattering matrix are conventionally called S-parameters. Recall that S-parameters can be written, see Eq. (3.7) - (3.9), in terms of the propagation factor

$$P = e^{-\gamma_0 \sqrt{\epsilon_r \mu_r} L}, \tag{A.20}$$

and the reflection coefficient

$$\Gamma = \frac{1 - \sqrt{\frac{\epsilon_r}{\mu_r}}}{1 + \sqrt{\frac{\epsilon_r}{\mu_r}}}. \tag{A.21}$$

In principle, if S-parameters are known, the electromagnetic parameters can be determined. Fig. A.3 shows the calculation algorithms, as a comparison, between the Nicolson-Ross-Weir (NRW) method and the reference-plane invariant algorithm (Publication I). In the RPI algorithm, neither Γ nor P are given in terms of L_1 and L_2.

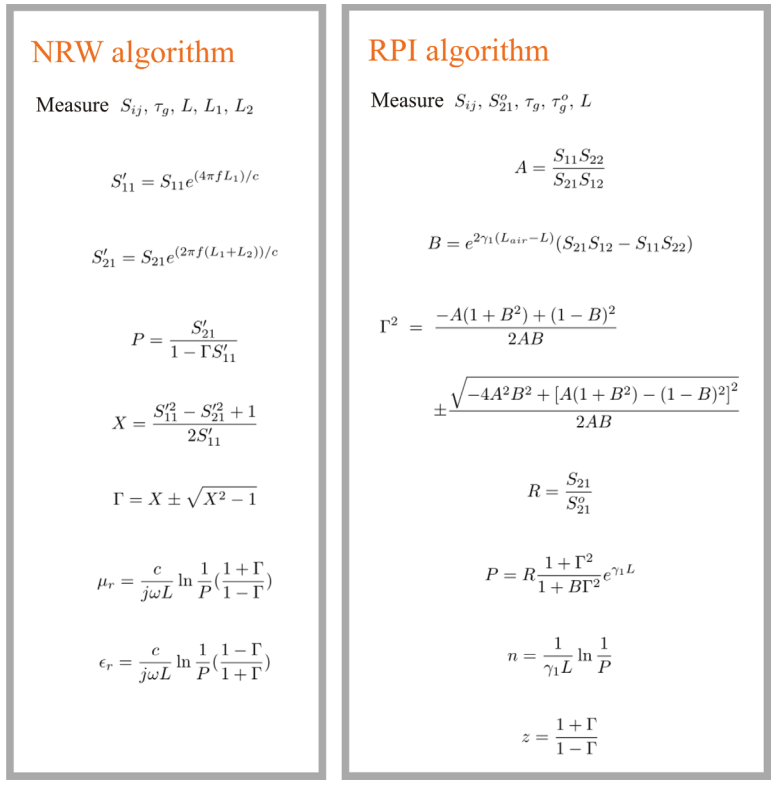

Figure A.3. The Nicholson-Ross-Weir (NRW) algorithm and the reference-plane invariant (RPI) algorithm for the determination of electromagnetic parameters.

The complex permittivity ϵ_r and the complex permeability μ_r can be analytically calculated when both the complex refractive index $n = \sqrt{\mu\epsilon}$ and

the wave impedance $z = \sqrt{\mu/\epsilon}$ are known. Since $z = (1+\Gamma)/(1-\Gamma)$, we can describe Γ using Eq. (3.13). This means the wave impedance can also be determined without specifying the reference-plane position. The measurements of S-parameters and group delays can be done by using a vector network analyzer.

The measurements of S-parameters and group delays are conducted, for example, by using a vector network analyzer. After a calibration, the empty transmission line was measured to obtain S_{21}^o and τ_{g}^o. Then a sample is inserted into the transmission line, and the measurement is repeated again. The source of errors can be eliminated by calibration. In the case when a perfect calibration is not possible due to technical problems, the phase errors can be reduced by averaging over different sample positions. Generally, the measurement uncertainties for the transmission/reflection are lower at higher frequencies.

A.2.2 The reflection method

A reflection measurement can be realized with either a short-circuit or a loaded transmission line. A systematic study of a short-circuit method is presented in Publication V. The idea is to express the electromagnetic parameters of the material in terms of the reflected signal, *i.e.* S_{11}, and determine the parameters by either a numerical technique (using an optimization or root-searching algorithm) or by an analytical calculation similar to the NRW method. Fig. A.4 shows a diagram describing how a toroidal sample is inserted inside a short-circuit coaxial transmission line. The numerical method used for this type of measurement setup is presented in Publication V.

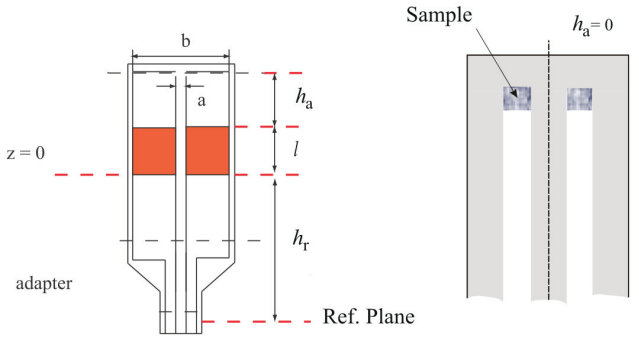

Figure A.4. Diagram showing the experimental setup for a short-circuit method: a sample is inserted inside a coaxial line near the short end. In case that the sample can be placed next to the short-circuit, h_a can be set to zero in the calculation algorithm.

A.2.3 Resonant cavity

A rectangular resonant cavity as shown in Fig. A.5 can be used to test anisotropic materials. With cavity parameters as given, the cavity is operated with the transverse electric field (TE_{mnl}) modes, with $m = 1$ and $n = 0$. The resonant frequencies f_r can be determined by

$$f_r = \frac{c}{2}\sqrt{\left(\frac{m}{a}\right)^2 + \left(\frac{n}{b}\right)^2 + \left(\frac{l}{d}\right)^2}, \tag{A.22}$$

where c is the microwave velocity, a is the width of the cavity, b is the height of the cavity. Table A.6 shows the prediction of the first six resonant peaks of the rectangular cavity by Eq. (A.22). In the case that

Waveguide cavity: WR_{340}
Frequency range: 2.17-3.30 GHz
Mode: TE_{10l}
Resonant frequency: 1.95, 2.48, 3.17 GHz
Width (x): 86 mm = a
Height (y): 43 mm
Length (z): 170 mm = d

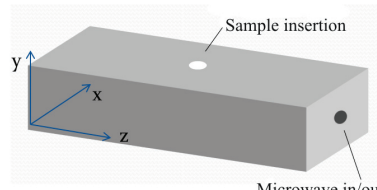

$$\vec{E} = E_0 \sin\left(\frac{\pi x}{a}\right) \sin\left(\frac{l\pi z}{d}\right) \hat{y}$$

Figure A.5. Using a rectangular cavity WR340 with the length of 170 mm, the cavity exhibits resonances at1.95, 2.48 and 3.17 GHz.

Cavity Dimensions							
Width (m)	a	0.08600	0.08600	0.08600	0.08600	0.08600	0.08600
Height (m)	b	0.04300	0.04300	0.04300	0.04300	0.04300	0.04300
Waveguide Length (m)	d	0.17000	0.17000	0.17000	0.17000	0.17000	0.17000
Resonant Modes	m	1	1	1	1	1	1
	n	0	0	0	0	0	0
	l	1	2	3	4	5	6
Resonant frequency (GHz)	f_r	1.95332	2.47949	3.16784	3.93414	4.74075	5.57018

Figure A.6. The resonant frequencies of a rectangular cavity WR340 operated with the transverse electric field modes TE_{mnl}.

the cavity is used to characterize a dielectric material, the experiment must be done with the 101, 103, and 105 TEM modes, where the electric field is maximum at the center (sample insertion) position. For magnetic materials, the 102, 104, and 106 modes are used instead.

With circular coupling aperture at the end of the cavity, the measurement with a vector network analyzer shows that the cavity exhibits resonances at frequencies close to the predicted values, see Fig. A.7.

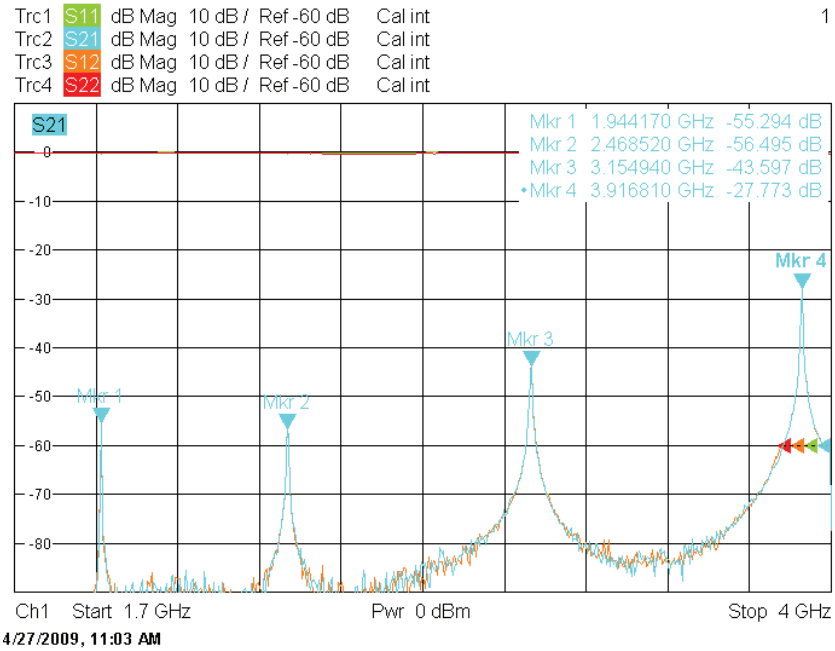

Figure A.7. The measured resonant frequencies of the rectangular cavity WR340.

B. Appendix: Instrumentation in Nanoscience

This chapter describes the basic physical principles of some instruments used for the fabrication and the characterization of materials at nanoscales.

B.1 SEM

The scanning electron microscope (SEM) is an imaging tool used for magnifying structures with dimensions below the diffraction limit of standard optical microscopes. The operation of an SEM begins with the scanning of a focused electron beam over the sample surface. Due to the interaction of these electrons with the atoms in the material, some particles (electrons, photons) are emitted from the surface. They are then received by a detector, and processed into an image. The brightness of each pixel in the image represents the intensity of the signal received from the corresponding point of the sample surface.

Typically, the scanning electron beam can interact with the sample via various mechanisms. Different mechanisms induce the emission of different particles, see Table B.1.

Positions	Emitted Particles	Remarks
Surface	Auger electrons	Low energy
Close to surface	Secondary electrons	Low energy
Deeper in sample	Backscattered electrons	Low energy
Deepest in sample	X-ray photons	

Table B.1. Particles generated by electron beams interacting with materials.

Although various kinds of signals can be detected and converted into images, a standard scanning electron microscope may have only one secondary electron detector. Normally, secondary electrons have low ener-

gies. They are mostly emitted from points near the surface (approximately 10 nm). The contrast of secondary electron images depends mainly on the tilt angle and topography of the specimen surface.

In an optical microscope, radiation from a source is focused through lenses onto the sample. In the case of an SEM, the electrons are 'focused' by electromagnetic lenses instead. An electromagnetic lens is comprised of a coil and a conducting cover, see Fig. B.1. By applying a current to the coils, a magnetic field is created. The electrons which come out in a spray pattern will then follow helical trajectories through the lens, and finally converge at the focal point. The advantage of the electromagnetic lens is that by varying the current through the coil, the focal length of the lens can be varied.

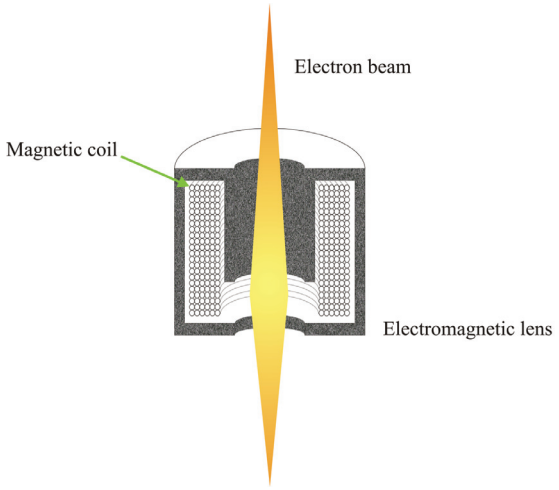

Figure B.1. The diagram of an electromagnetic lens in a scanning electron microscope

In an SEM, a number of electromagnetic lens are used to control the beam. If the magnetic field produced by a lens is not axially symmetrical, the refractive power will be different in the two mutually orthogonal planes. As a result, the electron beam will appear as an ellipse. This phenomenon is called astigmatism. If there is astigmatism in the objective lens, the SEM image will blur in one direction even at the in-focus condition.

The resolution of the SEM is high compared to an optical microscope because electrons have much shorter wavelengths compared to the wavelength of the visible light. From quantum mechanics, we know that particle wavelength is given by

$$\lambda = h/p = h/\sqrt{2meV_b} \approx 1.2/\sqrt{V_b} \qquad \text{nm.} \tag{B.1}$$

So, for EBL which operates at 30 kV, the wavelength of electron is approximately 0.007 nm. Although the wavelength of the electron is so short, it is still impossible to go beyond a critical resolution limit. This limit is caused by the signal to noise ratio. If we use a too small spot size, the current may be too low to induce enough secondary electron signals. This lowers the signal to noise ratio and also lowers the image quality. So, in order to produce a good quality image, one needs to compensate between the high resolution and the sharpness of the image.

Besides its high resolution, the SEM has a large depth of field (focus). This is because the SEM has a smaller aperture and a larger distance between the objective lens and the sample. The large depth of field makes the SEM a very useful tool in various fields. Biologists use SEM to observe tiny objects ranging from invisible viruses to tiny insects. Microelectronic industries use it for quality control process and failure analysis.

Nowadays, commercial SEMs have been developed so that they are much easier to use. However, the ease of use does not imply that a good-quality photo can be easily obtained. Many factors can affect the image quality. One factor comes from the users themselves. The users will not get a good result if they do not prepare the sample properly for the imaging. To obtain a satisfactory SEM image, the sample preparation should be done to guarantee that 1) the surface of the sample is clean enough, 2) the shape of the sample will not change during the exposure and 3) there will be no charge accumulated on the sample during the exposure. If the sample is non-conductive, we need to coat it with a thin layer of conductive material. This is an important step because charging on the sample surface can lead to many errors in the observation.

B.2 FIB

The focused ion beam (FIB) processing presented in this thesis was done with Ga^+ ions at 30 keV using an SEM/FIB dual beam microscope Helios Nanolab 600, see Fig. B.2. The ion source is gallium liquid metal. The resolution of the FIB is 5 nm when the microscope is set at the coincident working distance at 30 kV.

The FIB microscope is commonly used for imaging and sputtering. For imaging, the operation of the FIB is similar to that of an SEM. Usually, a FIB column consists of two lenses (a condenser and objective lens), apertures (to select the beam diameter and current), deflection plates (to

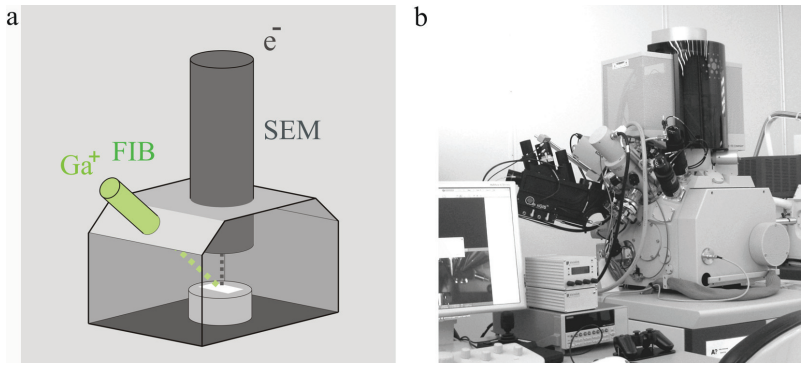

Figure B.2. a) Schematic illustration of the dual beam microscope b) SEM/FIB dual beam microscope.

sweep the beam), stigmation poles (to restore spherical beam profile), and a beam blanker [119]. The focusing and deflection of ions within an FIB system are done with electrostatic components. (Note that the FIB has a much lower charge/mass ratio, so if the focusing or deflection of ions were done with electromagnetic components, the size of the lens must be very large relative to the electromagnetic lens of an SEM.)

The results of an FIB processing depends on the ion-solid interaction. In general, when an ion collides with a solid sample, its kinetic energy is transferred to the solid via a series of collisions. The energy relaxation (energy and momentum transfer) involves various types of scattering (interaction) events resulting in both the electronic energy loss (excitation of electrons within the solid) and the nuclear energy loss (atoms are knocked out of their original positions). Both the electronic and the nuclear relaxations result in the emission of secondary electrons and the electromagnetic radiation. At 30 keV, a Ga^+ ion causes a series of binary linear collisions. These collisions result in the creations of vacancy pairs in the crystalline solid.

In practice, the results of FIB processing depends not only on the the incidence angle of the ion beam, but also on the type and geometry of the solid sample: crystal orientation, atomic mass, surface geometry, etc. For example, similar to the operation of an SEM, an FIB user is supposed to take into account the higher emission of the secondary electrons near an edge of the imaging structure.

The damage of a crystalline solid due to an ion beam process can be estimated if the stopping and range of ions are known. The calculation of the stopping and range of ions can be done, for example, by assuming that the ion and an atom inside the solid interact through the screen Coulomb

collision and the electronic exchange-correlation. The interaction between the ion and the solid induces various physical phenomena: electronic excitation, displacement of lattice atoms, and production of phonons.

Using the SRIM software [66], we can simulate the stopping and range of energetic ions into matter. Figure B.3 shows simulated collision cascades in an Al thin film due to 30 keV Ga^+ ion implantation. The simulations are done for a fixed-boundary Al film with the thickness of 50 nm. The simulation also shows that the Ga^+ ions can generate the ionization and phonon near the front surface of the film, see Fig. B.4

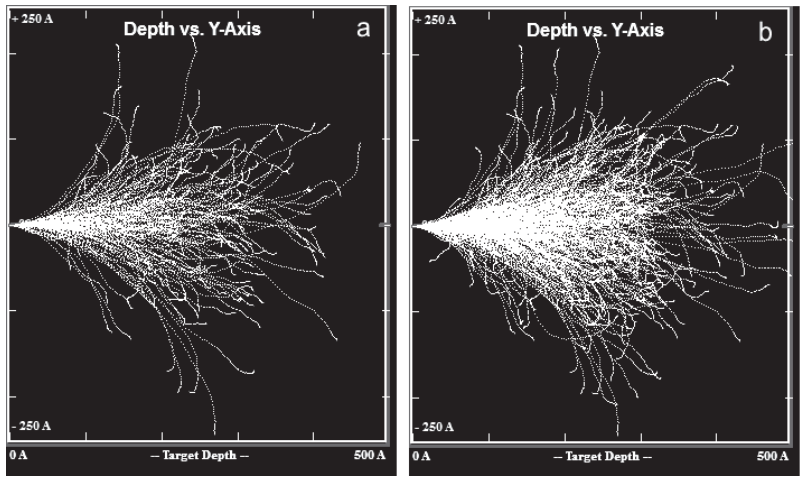

Figure B.3. SRIM simulation of collision cascades within a fixed Al film, generated by a) two hundreds Ga^+ ions and b) five hundreds Ga^+ ions at 30 keV.

B.3 AFM/MFM

An atomic force microscope (AFM) generally consists of a cantilever (probe tip), a laser, a photodetector, feedback electronics, and a positioning system (piezoelectric unit), see Fig. B.5. An AFM cantilever is usually made from silicon or silicon nitride. In the case of magnetic force microscopy, the tip of the probe is made by (or coated with) magnetic elements.

In this thesis, the AFM/MFM measurements were done by using a Veeco Dimension 5000 scanning probe microscope. Fig. B.6 shows a scanning electron microscopic image of an MFM probe (Bruker MESP-LC) made from 0.01 - 0.025 Ω cm Antimony (n) doped Si, coated with Co/Cr on the front side and Co/Cr on the back side. The average radius of the tip 35 nm.

The operation of an AFM starts by controlling the tip, and bringing it

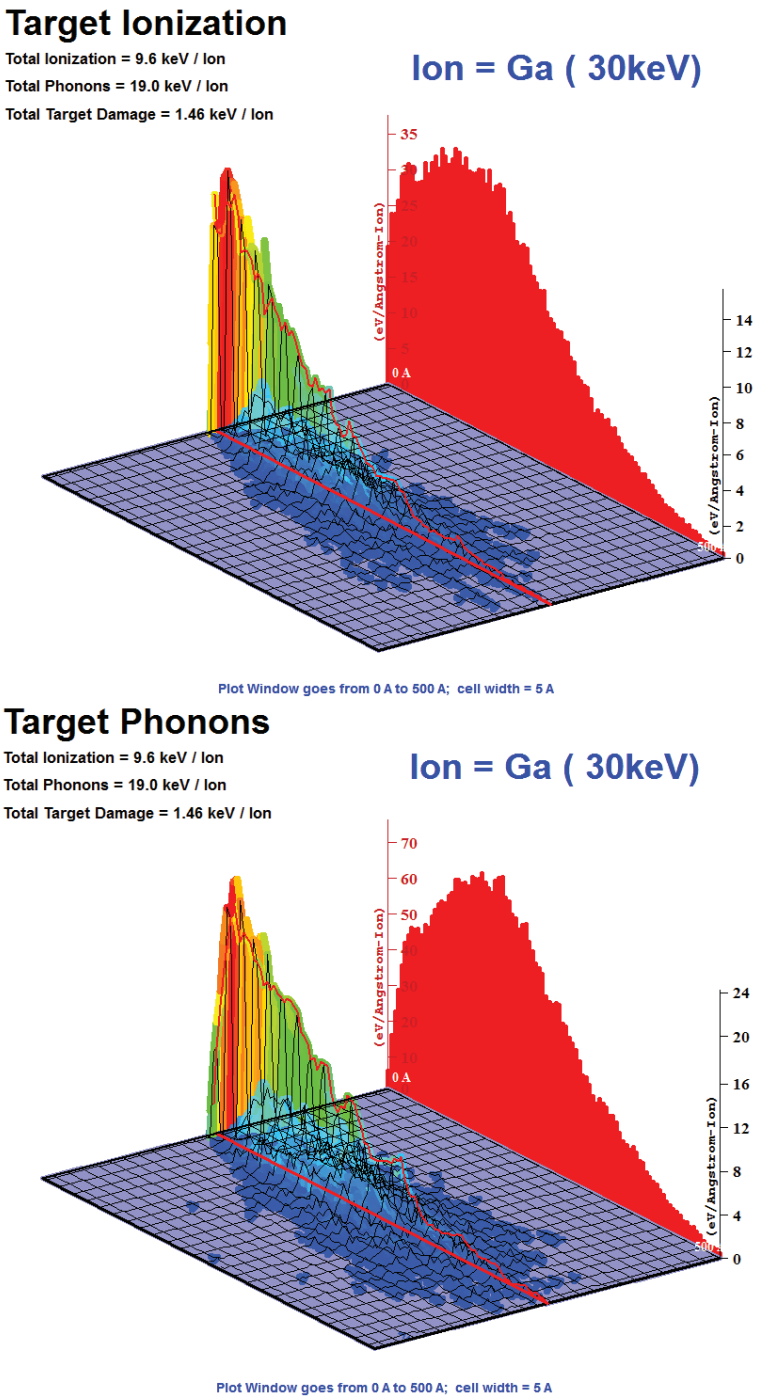

Figure B.4. SRIM simulation of the ionization and phonon generated after a fixed Al film is impinged by two hundreds Ga^+ ions at 30 keV.

down to a working distance (depending on the operation mode), which is usually in the proximity of a sample surface. The laser light used for

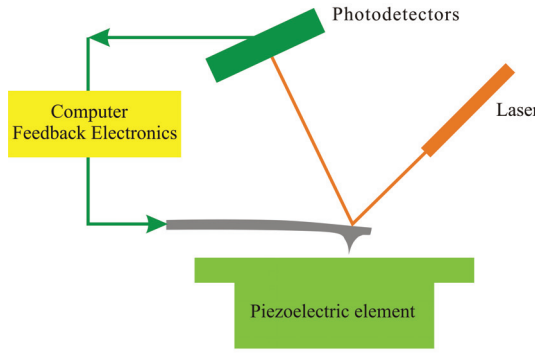

Figure B.5. A schematic illustration of an AFM/MFM microscope.

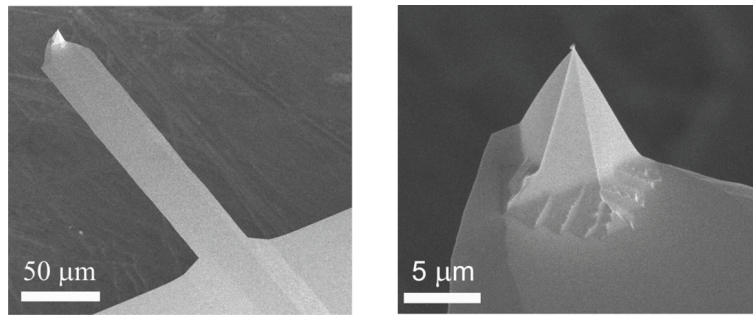

Figure B.6. The scanning electron microscope images of an MFM tip.

the detection is then focused and aligned on the upper surface (top) of the probe tip. The alignment is usually done so that the reflected light is absorbed at the center of the light detector.

In the non-contact mode, the probe tip is lower to a position above the sample surface. The deflection of the cantilever is then driven and detected. This processing provides the information about the oscillating frequency of the cantilever. The information also includes the force which can be modelled based on Hooke's law. Scanning the probe tip over the sample surface causes a shift of the frequency. Both the distance between the tip and the surface and the surface chemical composition can affect the results. The resolution of an AFM depends strongly on the diameter of the probe tip.

In the case of MFM, the cantilever scans the same area (line scanning) twice. The first scan is done in a regular mode (AFM mode) to collect the topological (height) image of the surface. The second scan is done at a lifted distance to detect the magnetic force. The magnetic image is processed by using the information from both scans.

Fig. B.7 shows the AFM/MFM images of a reference sample (a mag-

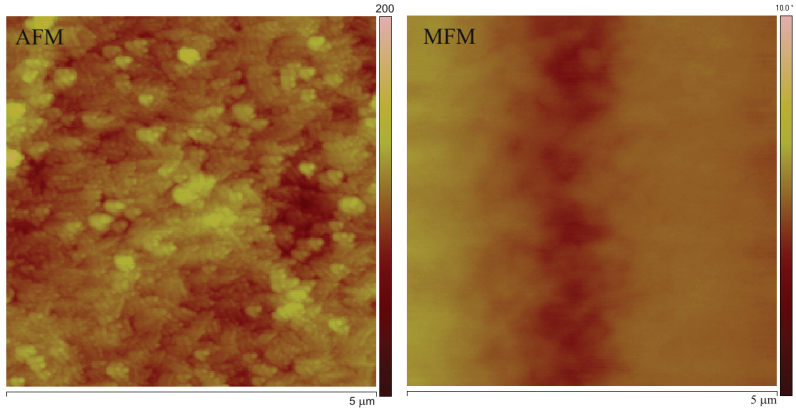

Figure B.7. The AFM/MFM images of a magnetic memory.

netic storage medium). The AFM image demonstrates that the reference sample is made of magnetic particles, while the MFM image provides an evidence that the sample has been magnetized equally along the vertical axis and periodically along the horizontal axis.

Bibliography

[1] E. S. Andersen, M. Dong, M. M. Nielsen, K. Jahn, R. Subramani, W. Mamdouh, M. M. Golas, B. Sander, H. Stark, C. L. P. Oliveira, J. S. Pedersen, V. Birkedal, F. Besenbacher, K. V. Gothelf, and J. Kjems. Self-assembly of a nanoscale dna box with a controllable lid. *Nature*, 459:73–76, 2009.

[2] S. Jeon, J.-U. Park, R. Cirelli, Shu Yang, C. E. Heitzman, P. V. Braun, P. J. A. Kenis, and J. A. Rogers. Fabricating complex three-dimensional nanostructures with high-resolution conformable phase masks. *PNAS*, 101(34):12428–12433, 2004.

[3] C. M. Soukoulis and M. Wegener. Past achievements and future challenges in the development of three-dimensional photonic metamaterials. *Nature Photonics*, 5:523–530, 2011.

[4] D. Chanda, K. Shigeta, S. Gupta, T. Cain, A. Carlson, A. Mihi, A. J. Baca, G. R. Bogart, P. Braun, and J. A. Rogers. Large-area flexible 3d optical negative index metamaterial formed by nanotransfer printing. *Nature Nanotechnology*, 6:402–407, 2011.

[5] T. Buckmann, N. Stenger, M. Kadic, J. Kaschke, A. Frolich, T. Kennerknecht, C. Eberl, M. Thiel, and M. Wegener. Tailored 3d mechanical metamaterials made by dip-in direct-laser-writing optical lithography. *Adv. Mater.*, 24(20):2710–1714, 2012.

[6] V. Ya. Prinz, V. A. Seleznev, A. K. Gutakovsky, A. V. Chehovskiy, V. V. Preobrazhenskii, M. A. Putyato, and T. A. Gavrilova. Free-standing and overgrown ingaas/gaas nanotubes, nanohelices and their arrays. *Physica E*, 6:828–831, 2000.

[7] V. Ya. Prinz. A new concept in fabricating building blocks for nanoelectronic and nanomechanic devices. *Microelectron. Eng.*, 69:466–475, 2003.

[8] L. Z. Wu, J. Ding, H. B. Jiang, C. P. Neo, L. F. Chen, and C. K. Ong. High frequency complex permeability of iron particles in a nonmagnetic matrix. *J. Appl. Phys.*, 99:083905, 2006.

[9] Zheng Hong, Yang Yong, Wen Fu-Sheng, Yi Hai-Bo, Zhou Dong, and Li Fa-Shen. Microwave magnetic permeability of fe3o4 nanoparticles. *Chin. Phys. Lett.*, 26(017501), 2009.

[10] Yang Yong, Xu Cai-Ling, Qiao Liang, Li Xing-Hua, and Li Fa-Shen. Microwave magnetic properties and natural resonance of ϵ-co nanoparticles. *Chin. Phys. Lett.*, 27(5):057501, 2010.

[11] C. P. Neo, Y. Yang, and J. Ding. Calculation of complex permeability of magnetic composite materials using ferromagnetic resonance model. *J. Appl. Phys.*, 107:083906, 2010.

[12] Longgang Yan, Jianbo Wang, Xianghua Han, Yong Ren, Qingfang Liu, and Fashen Li. Enhanced microwave absorption of fe nanoflakes after coating with sio_2 nanoshell. *Nanotechnology*, 21:095708, 2010.

[13] R. B. Yang W. L. Liang and C. K. Lin. Electromagnetic characteristics of manganese oxide-coated fe_3o_4 nanoparticles at 2-18 ghz. *J. Appl. Phys.*, 109:07D722, 2011.

[14] P. C. Fannin, S. W. Charles, and T. Relihan. A study of the effect of an external magnetic field on the resonant frequency of magnetic fluids. *J. Magn. Magn. Mater.*, 162:319–326, 1996.

[15] P. C. Fannin and S. W. Charles. Ac and dc magnetic measurements on colloidal suspensions of co particles. *J. Magn. Magn. Mater.*, 196(1-3):586–588, 1999.

[16] V. F. Puntes, K. M. Krishnan, and A. P. Alivisatos. *Science*, 291:2115–2117, 2001.

[17] V. F. Puntes, K. M. Krishnan, , and P. Alivisatos. Synthesis, self-assembly, and magnetic behavior of a two-dimensional superlattice of single-crystal ϵ-co nanoparticles. *Appl. Phys. Lett.*, 78:2187, 2001.

[18] J. V. I. Timonen, E. T. Seppala, O. Ikkala, and R. H. A. Ras. From hot-injection synthesis to heating-up synthesis of cobalt nanoparticles: observation of kinetically controllable nucleation. *Angew. Chem. Int. Ed.*, 50:2080–2084, 2011.

[19] I. A. Blech and C. Herring. Stress generation by electromigration. *Appl. Phys. Lett.*, 29(3):131–133, 1976.

[20] M. A. Korhonen, P. Borgesen, K. N. Tu, and Che-Yu Li. Stress evolution due to electromigration in confined metal lines. *J. Appl. Phys.*, 73(8):3790–3799, 1993.

[21] T. Ragab and C. Basaran. Joule heating in single-walled carbon nanotubes. *J. Appl. Phys.*, 106:063705, 2009.

[22] H. Xu, S. M. Anlage, L. Hu, and G. Gruner. Microwave shielding of transparent and conducting single-walled carbon nanotube films. *Appl. Phys. Lett.*, 90:183119, 2007.

[23] L. Lu, M. L. Sui, and K. Lu. Superplastic extensibility of nanocrystalline copper at room temperature. *Science*, 287(5457):1463–1466, 2000.

[24] M. D. Thouless, J. Gupta, and J. M. E. Harper. Stress development and relaxation in copper thin films during thermal cycling. *J. Mater. Res.*, 8:1845–1852, 1993.

[25] J. Schiotz, F. D. Di Tolla, and K. W. Jacobsen. *Nature*, 391:561, 1998.

[26] H. V. Swygenhoven. Grain boundaries and dislocations. *Science*, 296(5565):66–67, 2002.

[27] T. J. Rupert, Y. Gan D. S. Gianola, and K. J. Hemker. Experimental observations of stress-driven grain boundary migration. *Science*, 326(5960):1686–1690, 2009.

[28] J. Schiotz and K. W. Jacobsen. A maximum in the strength of nanocrystalline copper. *Science*, 301(5638):1357–1359, 2003.

[29] T. Zhu, J. Li, A. Samanta, A. Leach, and K. Gall. Temperature and strain-rate dependence of surface dislocation nucleation. *Phys. Rev. Lett.*, 100:025502, 2008.

[30] S. X. McFadden, R. S. Mishra, R. Z. Valiev, A. P. Zhilyaev, and A. K. Mukherjee. Low-temperature superplasticity in nanostructured nickel and metal alloys. *Nature*, 398:684–686, 1999.

[31] C. Wu. Superplastic metals stretch to a new low. *Science News*, 155(17):263, 1999.

[32] K. G. Libbrecht. Morphogenesis on ice: The physics of snow crystals. *Engineering & Science*, (1):10–19, 2001.

[33] J. T. Perron, J. W. Kirchner, and W. E. Dietrich. Formation of evenly spaced ridges and valleys. *Nature*, 460:502–505, 2009.

[34] Yang Lu, Jian Yu Huang, Chao Wang, Shouheng Sun, and Jun Lou. Cold welding of ultrathin gold nanowires. *Nature Nanotechnology*, 5:218–224, 2010.

[35] E. C. Garnett, W. Cai, J. J. Cha, F. Mahmood, S. T. Connor, M. G. Christoforo, Yi Cui, M. D. McGehee, and M. L. Brongersma. Self-limited plasmonic welding of silver nanowire junctions. *Nature Materials*, 11:241–249, 2012.

[36] S. Y. Chou, P. R. Krauss, and P. J. Renstrom. Imprint lithography with 25-nanometer resolution. *Science*, 272(5258):85–87, 1996.

[37] W. J. Arora, H. I. Smith, and G. Barbastathis. Membrane folding by ion implantation induced stress to fabricate three-dimensional nanostructures. *Microelectron. Eng.*, 84:1454–1458, 2007.

[38] L. Xia, W. Wu, J. Xu, Y. Hao, and Y. Wang. *MEMS, Istanbul, Turkey*, pages 118–121, 2006.

[39] K. Chalapat, N. Chekurov, J. Li, and G.S. Paraoanu. Ion beam assisted self-assembly of metallic nanostructures. *Nucl. Instrum. Meth. B*, 272:202–205, 2012.

[40] G. Matsuoka and T. Tawa. *Hitachi Review*, 52(3):158, 2003.

[41] http://www.vistec-semi.com.

[42] H. W. Deckman and J. H. Dunsmuir. Pmma electron resists with narrow molecular weight distribution. *J. Vac. Sci. Technol. B*, 1:1166, 1983.

[43] J. Taniguchi Y. Matsubara and I. Miyamoto. *International Microprocesses and Nanotechnology Conference Proceeding*, page 140.

[44] K. Yamazaki and H. Namatsu. *Microelectron. Eng.*, 73-74:85–89, 2004.

[45] Y. Sun, B. Mayers, and Y. Xia. Metal nanostructures with hollow interiors. *Adv. Mater.*, 15(7-8), 2003.

[46] S. Talapatra, S. Kar, S. K. Pal, R. Vajtai, L. Ci, P. Victor, M. M. Shaijumon, S. Kaur, O. Nalamasu, and P. M. Ajayan. Direct growth of aligned carbon nanotubes on bulk metals. *Nature Nanotechnology*, 1:112–116, 2006.

[47] Yihai Wang, Penglei Chen, and Minghua Liu. Synthesis of hollow silver nanostructures by a simple strategy. *Nanotechnology*, 19:045607, 2008.

[48] Lijia Pan, Hao Qiu, Chunmeng Dou, Yun Li, Lin Pu, Jianbin Xu, and Yi Shi. Conducting polymer nanostructures: template synthesis and applications in energy storage. *Int J Mol Sci.*, 11(7):2636–2657, 2010.

[49] D. H. Gracias, J. Tien, T. L. Breen, C. Hsu, and G. M. Whitesides. Forming electrical networks in three dimensions by self-assembly. *Science*, 289(5482):1170–1172, 2000.

[50] O. G. Schmidt and K. Eberl. Nanotechnology: Thin solid films roll up into nanotubes. *Nature*, 410:168, 2001.

[51] P. W. K. Rothemund. Folding dna to create nanoscale shapes and patterns. *Nature*, 440:297–302, 2006.

[52] C. Py, P. Reverdy, L. Doppler, J. Bico, B. Roman, and C. N. Baroud. Capillary origami: spontaneous wrapping of a droplet with an elastic sheet. *Phys. Rev. Lett.*, 98:156103, 2007.

[53] J.-H. Cho, M. D. Keung, N. Verellen, L. Lagae, V. V. Moshchalkov, P. V. Dorpe, and D. H. Gracias. Nanoscale origami for 3d optics. *Small*, 7:1943–1948, 2011.

[54] M. J. Harrington, K. Razghandi, F. Ditsch, L. Guiducci, M. Rueggeberg, J. W. C. Dunlop, P. Fratzl, C. Neinhuis, and I. Burgert. Origami-like unfolding of hydro-actuated ice plant seed capsules. *Nature Communications*, 2:337, 2011.

[55] G. Gore. *The art of electro-metallurgy*. London: Longmans, Green, and Co., 1877.

[56] G. G. Stoney. The tension of metallic films deposited by electrolysis. *Proc. R. Soc. Lond. A*, 82:172–175, 1909.

[57] O. G. Schmidt and N. Y. Jin-Phillipp. Free-standing sige-based nanopipelines on si (001) substrates. *Appl. Phy. Lett.*, 78:3310, 2001.

[58] F. Cavallo, R. Songmuang, C. Ulrich, and O. G. Schmidt. Rolling up sige on insulator. *Applied Physics Letters*, 90:193120, 2007.

[59] A. Malachias, Ch. Deneke, B. Krause, C. Mocuta, S. Kiravittaya, T. H. Metzger, and O. G. Schmidt. Direct strain and elastic energy evaluation in rolled-up semiconductor tubes by x-ray microdiffraction. *Phys. Rev. B*, 79:035301, 2009.

[60] J. A. Rogers, M. G. Lagally, and R. G. Nuzzo. Synthesis, assembly and applications of semiconductor nanomembranes. *Nature*, 477:45–53, 2011.

[61] Feng Li and Zetian Mi. Optically pumped rolled-up ingaas/gaas quantum dot microtube lasers. *Optics Express*, 17:19933–19939, 2009.

[62] G. Huang, Y. Mei, D. J. Thurmer, E. Coric, and O. G. Schmidt. Rolled-up transparent microtubes as two-dimensionally confined culture scaffolds of individual yeast cells.

[63] T.W. Clyne and S. C. Gill. Residual stresses in thermal spray coatings and their effect on interfacial adhesion: A review of recent work. *J. Therm. Spray Technol.*, 5:401–418, 1996.

[64] G. P. Nikishkov. Curvature estimation for multilayer hinged structures with initial strains. *J. Appl. Phys.*, 94:5333–5336, 2003.

[65] E. Chason, B. W. Sheldon, L. B. Freund, J. A. Floro, and S. J. Hearne. Origin of compressive residual stress in polycrystalline thin films. *Phys. Rev. Lett*, 88:156103, 2002.

[66] J. F. Ziegler and J. P. Biersack. Srim code. *http://www.srim.org*, 2003.

[67] K. Chalapat, K. Sarvala, J. Li, and G.S. Paraoanu. Wideband reference-plane invariant method for measuring electromagnetic parameters of materials. *IEEE Trans. Microw. Theory Tech.*, 57(9):2257–2267, 2009.

[68] L. Neel. Théorie du trainage magnétique des ferromagnétiques en grains fins avec applications aux terres cuites. *Ann. Géophys*, 5:99–136, 1949.

[69] C. Kittel. On the theory of ferromagnetic resonance absorption. *Phys. Rev.*, 73(2):155–161, 1948.

[70] L. D. Landau and E. M. Lifshitz. Theory of the dispersion of magnetic permeability in ferromagnetic bodies. *Phys. Zeitsch. der Sow.*, 8:153–169, 1935.

[71] J. H. E. Griffiths. Anomalous high-frequency resistance of ferromagnetic metals. *Nature*, 158:670, 1946.

[72] W. A. Yager and R. M. Bozorth. Ferromagnetic resonance at microwave frequencies. *Phys. Rev.*, 72:80, 1947.

[73] C. Kittel. Interpretation of anomalous larmor frequencies in ferromagnetic resonance experiment. *Phys. Rev.*, 71:270, 1947.

[74] T. L. Gilbert. A phenomenological theory of damping in ferromagnetic materials. *IEEE Trans. Magn.*, 40(6):3443–3449, 2004.

[75] P. C. Fannin, T. Relihan, and S. W. Charles. Experimental and theoretical profiles of the frequency-dependent complex susceptibility of systems containing nanometer-sized magnetic particles. *Phys. Rev. B*, 55(21):14423, 1997.

[76] P. Debye. *Polar Molecules*. The Chemical Catalog Company, New York, 1929.

[77] D. P. Dinega and M. G. Bawendi. A solution-phase chemical approach to a new crystal structure of cobalt. *Angew. Chem. Int. Ed.*, 38(12):1788–1791, 1999.

[78] S. Sun and C. B. Murray. Synthesis of monodisperse cobalt nanocrystals and their assembly into magnetic superlattices (invited). *J. Appl. Phys.*, 85(8), 1999.

[79] Y. Xia, Y. Xiong, B. Lim, and S. E. Skrabalak. Shape-controlled synthesis of metal nanocrystals: simple chemistry meets complex physics? *Angew. Chem. Int. Ed.*, 48(1):60–103, 2009.

[80] D. A. G. Bruggeman. Berechnung verschiedener physikalischer konstanten von heterogenen substanzen. *Ann. Phys.*, 416:636–679, 1935.

[81] J. C. M. Garnett. Colours in metal glasses and in metallic films. *Phil. Trans. R. Soc. Lond.*, 203:385–420, 1904.

[82] P. Mallet, C. A. Guerin, and A. Sentenac. Maxwell-garnett mixing rule in the presence of multiple scattering: Derivation and accuracy. *Phys. Rev. B.*, 72:014205, 2005.

[83] S. Tretyakov. *Analytical modeling in applied electromagnetics*. Artech House, Inc., 2003.

[84] K. Karkkainen, A. Sihvola, and K. Nikoskinen. Analysis of a three-dimensional dielectric mixture with finite difference method. *IEEE Trans. Geosci. Remote Sens.*, 39(5):1013, 2001.

[85] W. E. Kohler and G. C. Papanicolaou. *Some applications of the coherent potential approximation*. 1981.

[86] D. Mercier, J.-C. S. Lévy, G. Viau, F. Fiévet-Vincent, F. Fiévet, P. Toneguzzo, and O. Acher. Magnetic resonance in spherical co-ni and fe-co-ni particles. *Phys. Rev. B*, 62(1):532–544, 2000.

[87] H.-M. Chang and C. Liao. A parallel derivation to the maxwell-garnett formula for the magnetic permeability of mixed materials. *World Journal of Condensed Matter Physics*, 1:55–58, 2011.

[88] C. Brosseau, J. B. Youssef, P. Talbot, and A.-M. Konn. Electromagnetic and magnetic properties of multicomponent metal oxides heterostructures: Nanometer versus micrometer-sized particles. *J. Appl. Phys.*, 93(11):9243, 2003.

[89] J. V. I. Timonen, R. H. A. Ras, O. Ikkala, M. Oksanen, E. Seppala, K. Chalapat, J. Li, and G. S. Poraoanu. *Trends in Nanophysics*. Springer Berlin Heidelberg, 2010.

[90] D. Matsuura and T. Kizuka. Structures of graphene/cobalt interfaces in cobalt-encapsulated carbon nanocapsules. *Journal of Nanomaterials*, 2012:843516, 2012.

[91] M. Topsakal, H. Sahin, and S. Ciraci. Graphene coatings: An efficient protection from oxidation. *Phys. Rev. B*, 85:155445, Apr 2012.

[92] X. F. Zhang, X. L. Dong, H. Huang, Y. Y. Liu, W. N. Wang, X. G. Zhu, B. Lv, J. P. Lei, and C. G. Lee. Microwave absorption properties of the carbon-coated nickel nanocapsules. *Appl. Phys. Lett.*, 89:053115, 2011.

[93] M. Wu, Y. D. Zhang, S. Hui, T. D. Xiao, W. A. Hines S. Ge, J. I Budnick, and G. W. Taylor. Microwave magnetic properties of $co_{50}/(sio_2)_{50}$ nanoparticles. *Appl. Phys. Lett.*, 80:4404, 2002.

[94] G. Viau, F. Ravel, O. Acher, F. Fievet-Vincent, and F. Fievet. *J. Appl. Phys.*, 76:6570, 1994.

[95] G. Viau, F. Ravel, O. Acher, F. Fievet-Vincent, and F. Fievet. *J. Magn. Magn. Mater.*, 140-144:377–378, 1995.

[96] J.-C. Charlier, X. Blase, and S. Roche. Electronic and transport properties of nanotubes. *Rev. Mod. Phys.*, 79:677–732, 2007.

[97] S. Berber, Y.-K. Kwon, and D. Tomanek. *Phys. Rev. Lett.*, 84(20):4613–4616, 2000.

[98] M.-F. Yu, O. Lourie, M. J. Dyer, K. Moloni, T. F. Kelly, and R. S. Ruoff. *Science*, 287(5453):637–640, 2000.

[99] K. Jensen, W. Mickelson, A. Kis, and A. Zettl. Buckling and kinking force measurements on individual multiwalled carbon nanotubes. *Phys. Rev. B.*, 76(19):195436, 2007.

[100] B. Peng, M. Locascio, P. Zapol, S. Li, S. L. Mielke, G. C. Schatz, and H. D. Espinosa. Measurements of near-ultimate strength for multiwalled carbon nanotubes and irradiation-induced crosslinking improvements. *Nature Nanotechnology*, 3(10):626–631, 2004.

[101] S. Iijima. Helical microtubules of graphitic carbon. *Nature*, 354(6348):56–58, 1991.

[102] T. W. Ebbesen and P. M. Ajayan. Large-scale synthesis of carbon nanotubes. *Nature*, 358(6383):220–222, 1992.

[103] M. Jose-Yacaman, M. Miki-Yoshida, L. Rendon, and J. G. Santiesteban. Catalytic growth of carbon microtubules with fullerene structure. *Appl. Phys. Lett.*, 62:657, 1993.

[104] Ting Guo, P. Nikolaev, A. Thess, D. Colbert, and R. Smalley. Catalytic growth of single-walled nanotubes by laser vaporization. *Chem. Phys. Lett.*, 243:49–54, 1995.

[105] A. Oberlin, M. Endo, and T. Koyama. Filamentousgrowth of carbon through benzenedecomposition. *Journal of Crystal Growth*, 32(3):335–349, 1976.

[106] M. Reibold, P. Paufler, A. A. Levin, W. Kochmann, N. Patzke, and D. C. Meyer. Carbon nanotubes in an ancient damascus sabre. *Nature*, 444:286, 2006.

[107] N. Hamada, S.-I. Sawada, and A. Oshiyama. New one-dimensional conductors: Graphitic microtubules. *Phys. Rev. Lett.*, 68(10):1579, 1992.

[108] R. Saito, M. Fujita, G. Dresselhaus, and M. S Dresselhaus. Electronic structure of chiral graphene tubules. *Appl. Phys. Lett.*, 60(2204), 1999.

[109] J. W. G. Wildoer, L. C. Venema, A. G. Rinzler, R. E. Smalley, and Cees Dekker. Electronic structure of atomically resolved carbon nanotubes. *Nature*, 391:59–62, 1998.

[110] Y.-K. Kwon and D. Tomanek. Electronic and structural properties of multiwall carbon nanotubes. *Phys. Rev. B*, 58(24):R16001, 1998.

[111] Y. Inoue, K. Kakihata, Y. Hirono, T. Horie, A. Ishida, and H. Mimura. One-step grown aligned bulk carbon nanotubes by chloride mediated chemical vapor deposition. *Appl. Phys. Lett.*, 92:213113, 2008.

[112] A. M. Nicolson and G. F. Ross. Measurement of the intrinsic properties of materials by time-domain techniques. *IEEE Trans. Instrum. Meas.*, IM-19:377–382, 1970.

[113] W. B. Weir. Automatic measurement of complex dielectric constant and permeability at microwave frequencies. *Proc. IEEE*, 62:33–36, 1974.

[114] J. Baker Jarvis, E. J. Vanzura, and W. A. Kissick. Improved technique for determining complex permittivity with the transmission/reflection method. *IEEE Tran. Microw. Theory Tech.*, 38(8):1096–1103, 1990.

[115] C. Wan, B. Nauwelaers, W. De Raedt, and M. V. Rossum. Two new measurement methods for explicit determination of complex permittivity. *IEEE Tran. Microw. Theory Tech.*, 46:1614–1619, 1998.

[116] J. C. Maxwell. A dynamical theory of the electromagnetic field. *Phil. Trans. R. Soc. Lond.*, 155:459–512, 1865.

[117] J. D. Jackson. *Classical Electrodynamics*. John Wiley and Sons Ltd, 1962.

[118] L. D. Landau and E. M. Lifshitz. *The classical theory of fields*. Pergamon Press, 1971.

[119] C. A. Volkert and A. M. Minor. Focused ion beam microscopy and micromachining. *MRS Bulletin*, 32:389, 2007.

Errata

Publication I

Typo error: Eq. (27), $z = \frac{1+\Gamma}{1-\Gamma}$

When subatomic ingredients, such as electrons, protons and neutrons, join together to form condensed matter systems, collective phenomena emerge. These phenomena occur in all forms of matter ranging from chemistry in living organisms to the emergence of magnetic states and superconductivity. The interaction between the subatomic ingredients with the external world defines the existence and the manifestation of the world as we perceived it.

ISBN 978-952-60-5188-8
ISBN 978-952-60-5189-5 (pdf)
ISSN-L 1799-4934
ISSN 1799-4934
ISSN 1799-4942 (pdf)

Aalto University
School of Science
O.V. Lounasmaa Laboratory
www.aalto.fi

BUSINESS + ECONOMY

ART + DESIGN + ARCHITECTURE

SCIENCE + TECHNOLOGY

CROSSOVER

DOCTORAL DISSERTATIONS

Aalto-DD 91/2013